MICRU: a sophisticated effective cloud fraction algorithm designed for UV/vis satellite instruments with large viewing angles

Holger Sihler[1], Steffen Beirle[1], Steffen Dörner[1], Marloes Gutenstein-Penning de Vries[1,2], Christoph Hörmann[1,3], Christian Borger[1], Simon Warnach[1], and Thomas Wagner[1]

[1]Max Planck Institute for Chemistry, Hahn-Meitner-Weg 1, 55128 Mainz, Germany
[2]now at: Deutscher Wetterdienst, Offenbach, Germany
[3]now at: Volume Graphics GmbH, Heidelberg, Germany

Correspondence: holger.sihler@mpic.de

Abstract. Clouds impact the radiative transfer of the Earth's atmosphere and strongly influence satellite measurements in the UV visible and IR spectral ranges. For satellite measurements of trace gases absorbing in the UV/vis spectral range, particularly clouds ultimately determine the vertical sensitivity profile, mainly by reducing the sensitivity for trace gas columns below the cloud.

The Mainz Iterative Cloud Retrieval Utilities (MICRU) algorithm is specifically designed to reduce the error budget of trace gas retrievals, such as those for nitrogen dioxide (NO_2), which strongly depends on the accuracy of small cloud fractions (CF) in particular. The accuracy of MICRU is governed by an empirical parametrisation of the viewing geometry dependent background surface reflectivity taking instrumental and physical effects into account. Instrumental effects are mainly degradation and polarisation effects, physical effects are due to the anisotropy of the surface reflectivity, e. g. shadowing of plants and sun glitter.

MICRU is applied to main science channel (MSC) and polarisation measuring device (PMD) data collected between April 2007 and June 2013 by the GOME-2A instrument onboard the MetOp-A satellite. CF are retrieved at different spectral bands between 374 and 758 nm. The MICRU results for MSC and PMD at different wavelengths are inter-compared to study CF precision and accuracy, which depend on wavelength and spatial correlation. Furthermore, MICRU results are compared to FRESCO (Fast Retrieval Scheme for Clouds from the Oxygen A band) and OCRA (Optical Cloud Recognition Algorithm) operational cloud products.

We show that MICRU retrieves small CF with an accuracy of 0.04 or better for the entire 1920 km wide swath with a potential bias between -0.01 and -0.03. CF retrieved at shorter wavelengths are less affected by adverse surface heterogeneities. The comparison to the operational CF algorithms shows that MICRU significantly reduces the dependence on viewing angle, time, and sun glitter. Systematic effects along coasts are particularly small for MICRU due to its dedicated treatment of land and ocean surfaces.

The MICRU algorithm is designed for spectroscopic instruments ranging from the GOME to TROPOMI/Sentinel-5P, but is also applicable to UV/vis imagers like, for example, AVHRR, MODIS, VIIRS, and Sentinel-2.

1 Introduction

Clouds are the most clearly visible component of the atmosphere, both from the ground and from space. Their presence increases the shortwave albedo of the Earth and, hence, reduces the amount of solar radiation absorbed by the Earth. Clouds furthermore alter the radiative transfer (RT) within the atmosphere by effectively shielding the underlying atmosphere and
5   surface from observation. This paper focuses on the influence of clouds on the measurement sensitivity for atmospheric trace-gases retrieved from satellite observations in the UV and visible (UV/vis) spectral ranges. The largest portion of the Earth's surface is darker than overlying clouds. In this scenario, the measurement sensitivity – that is the air mass factor (AMF) (Noxon et al., 1979; Solomon et al., 1987; McKenzie et al., 1991; Perliski and Solomon, 1993; Sarkissian et al., 1995; Rozanov and Rozanov, 2010; Deutschmann et al., 2011) – is decreased for trace gas abundances below clouds and increased above
10 (see e. g. Wagner et al., 2003). For trace gases located within clouds, however, the influence of clouds depends on the cloud characteristics and trace-gas profiles. In any case, cloud properties need to be carefully constrained in order to achieve high accuracy in tropospheric trace-gas measurements from satellites (De Smedt et al., 2008; Liu et al., 2011; Barkley et al., 2012; Lorente et al., 2017). Boersma et al. (2004), for example, estimated the uncertainty in the tropospheric air mass factor for GOME measurements of nitrogen dioxide (NO_2) due to uncertainties in the cloud fraction between 25 and 30% over large
15 parts of North America, Europe and South East Asia, where most anthropogenic NO_2 emission occur.

Satellite retrievals of trace gases with high abundances in the boundary layer depend on the amount and properties of clouds within one satellite pixel. The effective cloud fraction (CF, c) is one measure to quantify cloud contamination. CF is defined by

$$c = \frac{R - R_{\min}}{R_{\max} - R_{\min}} \tag{1}$$

20 based on the top of atmosphere (TOA) reflectance

$$R = \frac{\pi I}{E_0 \cos \vartheta_0} \tag{2}$$

with TOA radiance I, solar irradiance E_0, and solar zenith angle ϑ_0. This definition of c applies the independent pixel-approximation (IPA) neglecting the influence of horizontal RT (Martin et al., 2002). $R_{\min}$ and $R_{\max}$ in Eq. (1) denote lower and upper thresholds corresponding to reflectances from cloud free and completely cloudy pixel, respectively. $R_{\min}$ depends
25 on the reflecting properties of the surface and viewing geometry. Hence, an $R_{\min}$ approximating the time dependency of the actual bidirectional reflectance distribution function (BRDF) is required for any geolocation in order to retrieve small CF at high accuracy. In contrary, $R_{\max}$ depends on cloud albedo. The cloud albedo depends on optical density and scattering properties, which can be described by an a priori cloud model, in addition to the observation geometry. $R_{\max}$ may be empirically determined (e. g Grzegorski et al., 2006; Lutz et al., 2016) or calculated using a radiative transfer model (RTM) (e. g. Wang
30 et al., 2008). MICRU applies a Lambertian cloud model with a fixed albedo of 0.8 (e. g. McPeters et al., 1996; Stammes et al., 2008; Vasilkov et al., 2017), rendering $R_{\max}$ depending on observation geometry alone.

Within tropospheric trace gas retrievals, cloudy pixels are usually flagged applying a threshold for c between 10 and 30%, and a high accuracy of c is required for the correction of cloud effects of remaining pixels. Specifically, the accurate determination

of R_{min} is crucial to determine small CF accurately. R_{min} depends on the geolocation and time and, therefore, maps of the lower threshold are needed. The Heidelberg iterative cloud retrieval utilities (HICRU), for example, derive background maps based on TOA reflectances using imaging processing techniques (Grzegorski et al., 2006; Grzegorski, 2009). In contrary, Koelemeijer et al. (2003) take Rayleigh scattering into account providing Lambert-equivalent reflectivity (LER) maps. More sophisticated

5 methods apply complex BRDF accounting for the anisotropy of the surface reflectivity (Vasilkov et al., 2017; Lorente et al., 2018), or apply a geometry-dependent LER model (Vasilkov et al., 2018; Loyola et al., 2020).

Algorithms for the retrieval of background maps usually rely on completely cloud-free observations over a certain location. Here, we are interested in CF of spectroscopic measurements. Compared to imager instruments, spectrometers are characterised by lower spatial but much higher spectral resolution. For example, the imager Visible Infrared Imaging Radiometer Suite

10 (VIIRS) features 22 spectral channels at a resolution of approximately 400 m whereas the spectrometer Ozone Monitoring Instrument (OMI) offers 1176 spectral channels at a nadir resolution of 13 km × 24 km (Schueler et al., 2002; Levelt et al., 2006; KNMI, 2019; de Graaf et al., 2016; Sihler et al., 2017). Based on this difference of spatial resolution, it becomes evident that the probability to obtain a completely cloud-free observation over a certain location is much higher for imagers than for spectrometers (Krijger et al., 2007). Therefore, background-reflectance retrieving algorithms applicable to spectrometer data

15 have to deal with much sparser statistics than those tailored for imagers.

Algorithms deriving cloud fractions from spectroscopic measurements feature different approaches for background maps. One of the first algorithms published for the Global Ozone Monitoring Instrument (GOME, Burrows et al., 1999) is Initial Cloud Fitting Algorithm (ICFA) applying the global digital elevation model ETOPO5 (Kuze and Chance, 1994; Tuinder et al., 2004). Seven years later, Koelemeijer et al. (2001) published the fast method for retrieval of cloud parameters using oxygen A-

20 band measurements (FRESCO), whose development continued as FRESCO+ (Fournier et al., 2006; Wang et al., 2008; TEMIS, 2019). Operational algorithms, like FRESCO+, apply background maps from auxiliary instruments in order to provide data directly after launch. The algorithms are then usually updated implementing different background maps as the mission evolves. The background maps may be either supplied from spectrometers or images. FRESCO version 6, for example, applies imager data from the Medium Resolution Imaging Spectrometer (MERIS) resolving albedo gradients, e. g. over coastlines, much better

25 than the spectrometer data (Popp et al., 2011). Kokhanovsky et al. (2009), on the other hand, interprets MERIS data using threshold techniques to derive cloud fractions for Scanning Imaging Absorption Spectrometer for Atmospheric Cartography (SCIAMACHY, Bovensmann et al., 1999). FRESCO version 7 features another approach for the Global Ozone Monitoring Experiment 2 (GOME-2, Callies et al., 2000; Munro et al., 2006, 2016) applying Lambertian Equivalent Reflectance (LER) maps derived from GOME-2 itself (TEMIS, 2019; Tilstra et al., 2017b). Version 8 of FRESCO then applies a LER climatology

30 derived from GOME-2 data taking the viewing geometry into account. In contrast to FRESCO, Optical Cloud Recognition Algorithm (OCRA) applies background maps derived in the RGB color space (Loyola, 1998; Loyola et al., 2007; Lutz et al., 2016). In its third version developed for GOME-2 and the Tropospheric Monitoring Instrument (TROPOMI, Veefkind et al., 2012), OCRA also accounts for degradation, viewing geometry dependence, and sun glint (Lutz et al., 2016). The fourth version of OCRA applied to TROPOMI is described by Loyola et al. (2018). For OMI, the first version of OMCLDO2 (Stammes et al.,

35 2008) uses albedo data from GOME (Koelemeijer et al., 2003) and TOMS (Herman and Celarier, 1997) for calculating effective

cloud fractions, whereas OMCLDO2 version 2 (Veefkind et al., 2016) applies a LER database derived from OMI measurements themselves as published by (Kleipool et al., 2008). It is preferred to apply background maps from the same sensor for cloud retrievals – like in (Grzegorski et al., 2006), (Veefkind et al., 2016), and (Tilstra et al., 2017b) – in order to achieve higher CF accuracy especially at small CF because radiometric properties and their dependence on viewing angles vary between sensors

5 (e. g. Tilstra et al., 2012). This approach is especially suitable for scientific studies using data processed offline. However, operational CF processors require background obtained from auxiliary sensors because data from the same sensor is then not yet available.

Recent developments also focus on applying geometry dependent background maps in CF algorithms. HICRU empirically derives lower thresholds for each of the three subpixels of GOME separately (Grzegorski et al., 2006). For instruments featuring

10 wider swaths like OMI and GOME-2, the limitations of the LER surface model become more important (Vasilkov et al., 2017; Lorente et al., 2017, 2018; Fasnacht et al., 2019). Lorente et al. (2018) find biases in cloud fractions of up to 50% between backward-scattering and forward-scattering geometries in the GOME-2 FRESCO and 26% in the OMI OMCLDO2 cloud algorithms. Vasilkov et al. (2017) show that applying a geometry dependent LER instead of a regular LER can lead up to a 50% increase of the trace-gas column density over polluted areas. Furthermore, Vasilkov et al. (2018) compared CF derived

15 using geometry dependent LER with those based on regular LER and found CF differences of up to 0.07, especially for small CF. These absolute differences correspond to relative errors that have a significant impact on trace gas retrievals. Aerosols, however, reduce the effect of the BRDF (Noguchi et al., 2015). These recent studies rely on BRDF information derived from Moderate Resolution Imaging Spectroradiometer (MODIS, Justice et al., 1998) measurements because similar information from spectrometers is yet too sparse to derive all coefficients of, for example, the Ross-Li BRDF model (Wanner et al., 1995).

20 This paper presents a new method to derive a geometry dependent lower threshold map from spectroscopic measurements. The Mainz iterative cloud retrieval utilities (MICRU) apply an empirical parametrisation of the geometry dependence in order to overcome the limitation of having sparse data per geolocation. MICRU derives the lower threshold as LER in contrast to its heritage algorithm HICRU, which applies TOA reflectances directly. Hence, first order atmospheric effects are accounted for. Remaining dependencies on the viewing angle, which may be either instrumental artefacts or physical, are modelled by a

25 combination of a second order polynomial and a reduced model for surface effects of land and sun glitter over ocean (Cox and Munk, 1954a; Harmel and Chami, 2013; Martin et al., 2016). It is noted that the idea of modelling the viewing angle dependence using a second order polynomial is not new. For example, Várnai and Marshak (2007) used a second order polynomial to model the mean optical thickness of inhomogeneous clouds in MODIS measurements.

In this study, we apply MICRU to GOME-2 data exemplarily. Unlike its heritage algorithm, HICRU, MICRU is applicable

30 to almost arbitrary wavelength intervals in the UV/vis wavelength region. MICRU furthermore uses an RT model to reduce the influence of atmospheric scattering for the retrieval of R_{min}. MICRU CF are evaluated between 382 and 757.5 nm in order to investigate the spectral stability of the algorithm, the influence of the surface on CF accuracy, and the influence of spatial aliasing specific to GOME/GOME-2 instruments (EUMETSAT, 2015).

The MICRU algorithm has been developed as part of the cloud fraction verification activities for the TROPOMI/S5P

35 (Veefkind et al., 2012) and Sentinel 5 satellite missions. The operational cloud fraction algorithms for TROPOMI/S5P is

4

OCRA (Loyola et al., 2018) and FRESCO is an auxiliary cloud product used for selected level 2 products (Wang et al., 2008), respectively. A comparison between all three algorithms is performed in Sect. 3, after introducing MICRU in Sect. 2.

2 Method

MICRU is designed to be applicable to UV/vis satellite sensors operating on sun-synchronous orbits. In this study, we examine its applicability using GOME-2 data. This section first describes the required input data (sec. 2.1) and the conversion between TOA reflectances R to the LER (Sect. 2.2). Section 2.3 then details the retrieval of T_{min} maps. The calculation of R_{max} is

5 described in Sect. 2.4. Section 2.5 specifies the implementation of the MICRU algorithm, followed by a description of data sets MICRU results are compared to (Sect. 2.6).

2.1 Input data

2.1.1 GOME-2 data

The primary data used in this work are radiances measured by the GOME-2 instrument onboard MetOp satellites. There are

10 three essentially identical MetOp satellites in total: MetOp-A was launched in 2006 followed by MetOp-B and MetOp-C in 2012 and 2018, respectively. The MetOp satellites fly in a sun-synchronous orbit with an equator crossing-time around 9:30 solar local time (Munro et al., 2016). This study applies data from GOME-2A only as it features the longest uninterrupted time-series at the time of the MICRU algorithm development.

GOME-2 has four spectral main science channels (MSCs) with a spectral resolution between 0.26 and 0.51 nm ranging

15 between 240 and 790 nm. Each MSC band features 1024 spectral channels. This study uses GOME-2A MSC data collected between February 2007 and June 2013. Data before and after this period are discarded in order to avoid interferences from instrument startup and a change of the operational swath width, respectively (EUMETSAT, 2015). Furthermore, GOME-2 has two polarization measurement devices (PMDs) covering a similar spectral range but at a much coarser spectral resolution: PMD-PP and PMD-SP measure the polarised intensity parallel and perpendicular to the slit of the spectrometer, respectively.

20 Lang (2010) defines 15 discrete wavelength intervals for each PMD instrument. On 11 March 2008, the PMD band definitions of GOME-2A were updated to version 3.1 (EUMETSAT, 2015; Munro et al., 2016). Therefore, PMD data obtained before April 2008 are disregarded here in order to achieve a consistent PMD data set. All spectral data is contained in the level 1b (L1b) data (processor version 5.3) provided by EUMETSAT.

GOME-2 is a scanning spectrometer featuring a nominally 1920 km wide swath, which was reduced to 960 km in July 2013

25 (Munro et al., 2016). One swath consists of 32 MSC or 256 PMD pixels, respectively. One swath is divided into a forward and a backward scan. The scanner turns three times faster during the backward scan resulting in three times larger pixels, which are discarded altogether in the following. Hence remaining are 24 MSC or 192 PMD pixels, respectively. At nadir, the nominal, that is forward scan, MSC pixel size is 40 km × 80 km in along- and across-track direction, respectively. The PMDs feature an eight times higher acquisition frequency leading to a smaller pixel size of 40 km × 10 km. The illumination-observation geometry

30 is defined by the solar zenith angle (SZA) θ_0, the viewing zenith angle (VZA) θ and the relative azimuth angle (RAA) ϕ as sketched in Fig. 1. The angles are defined at the pixel center at the surface. It is noted that the along-track pixel size increases with increasing VZA due to the Earth's curvature. Hence, the pixel shape becomes trapezoidal (de Graaf et al., 2016; Sihler et al., 2017).
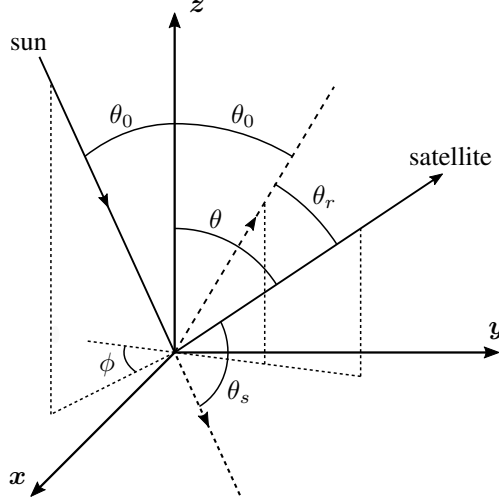
Figure 1. Angle definition at the surface: solar zenith angle θ_0, viewing zenith angle θ and relative azimuth angle ϕ, scattering angle θ_s, and reflected sun angle θ_r. Zenith is towards z.

In the spectral domain, the MICRU algorithm is applied to 14 MSC and 16 PMD channels in order to assess the influence of systematic differences on the accuracy of c. In principle, the radiometric input required by MICRU may be integrated along any spectral interval, but it is beneficial to avoid significant absorption structures in order to minimise the influence of atmospheric absorptions. A dependence on the accuracy of the spectral calibration, which may not be optimal, is reduced by avoiding narrowband absorption features and Fraunhofer lines. Furthermore, broadband absorption by molecules and aerosols interferes with the inversion of the LER from measured R. Interferences may not be avoided completely in the UV/vis, but MICRU MSC channels are defined minimising interferences from broad- and narrowband spectral features caused by Fraunhofer lines, inelastic Raman scattering (Grainger and Ring, 1962; Solomon et al., 1987, Ring effect), and molecular absorption by H_2O, O_2, and O_4. The TOA reflectance R_k of MSC channel k is derived from the measured spectrum $R(\lambda)$ by applying

$$R_k = R(\lambda) * K_k(\lambda) \tag{3}$$

where K_k is the convolution kernel of channel k. K_k are either Gaussian or boxcar convolution kernels with different widths as listed in Table 1 and depicted in Fig. 2. The MICRU PMD channels as listed in Table 2 are selected from predefined PMD bands (Lang, 2010).

The convolution kernels for 14 MICRU MSC channels are manually defined in the range between 374 and 758 nm. Hence, CF results are available for a variety of spectral ranges with different atmospheric trace gas absorptions. This is particularly important to improve collocation between CF and trace gas measurement featuring different spatial sensitivities caused by spatial aliasing (EUMETSAT, 2015; Munro et al., 2016). Spatial aliasing is caused by the sequential detector readout in connection with the movement of the GOME-2 scanning mirror (Sihler et al., 2017). The comparison of MICRU results from MSC channels 2, 5, 10, and 11 allows the investigation of spatial aliasing. These channels furthermore allow to compare the

7

Table 1. Definition of MICRU MSC channels k with spectral convolution kernels K centred at $\overline{\lambda}$ and width w. The kernels are either Gaussian (denoted G) or boxcar (denoted b) shaped. According to the spatial aliasing of GOME-2 (Fig. 3), channels 1, 4, 5, and 10 apply the same readout time as corresponding MSC/PMD channels in different bands.

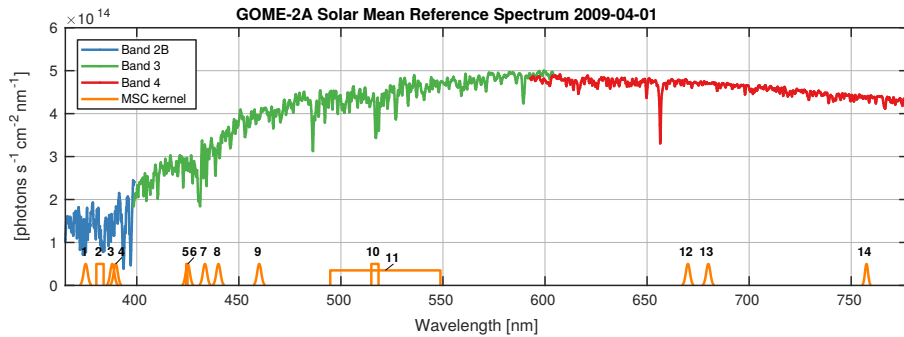| Channel k	Spectral convolution kernel centre	width	shape	MSC band	RT wavelength	Comment
1	374.96 nm	1.00 nm	G	2B	375.0 nm	same timing as channel 9
2	381.97 nm	3.57 nm	b	2B	382.0 nm	range of PMD-PP band 6
3	388.00 nm	1.00 nm	G	2B	388.0 nm	KNMI GOME-2 LER @ 388 nm
4	389.68 nm	1.00 nm	G	2B	389.7 nm	same timing as channel 14
5	424.52 nm	0.64 nm	b	3	424.5 nm	timing of PMD-PP band 6
6	425.00 nm	1.00 nm	G	3	425.0 nm	KNMI GOME-2 LER @ 425 nm
7	433.40 nm	1.00 nm	G	3	433.4 nm	same timing as channel 14
8	440.00 nm	1.00 nm	G	3	440.0 nm	KNMI GOME-2 LER @ 440 nm
9	460.00 nm	1.00 nm	G	3	460.0 nm	range of NO2 retrieval
10	516.67 nm	3.52 nm	b	3	519.0 nm	timing of PMD-PP band 9
11	521.77 nm	53.98 nm	b	3	521.8 nm	range of PMD-PP band 9
12	670.00 nm	1.00 nm	G	4	670.0 nm	KNMI GOME-2 LER @ 670 nm
13	680.00 nm	1.00 nm	G	4	680.0 nm	short of red edge and O_2-B band
14	757.50 nm	0.75 nm	G	4	757.5 nm	short of O_2-A band (FRESCO)

Figure 2. Mean solar spectrum of GOME-2A MSC channels 2B, 3, and 4 recorded on 1 April 2009. Spectral convolution kernels K_k from Table 1 are plotted in orange. Note small biases between overlapping bands due to different calibrations.

effect of spatial with spectral aliasing, which is due to differences in the spectral response of different channels. The horizontal arrows in Fig. 3 indicate MSC channels 2 and 5 matching the spectral sensitivity of the two PMD-PP/SP channel pairs 1/9 and 4/12, respectively. The vertical arrows indicate MICRU channels featuring the same acquisition time, and, hence, minimizing

Table 2. Definition of MICRU PMD channels for PP and SP polarisation, respectively. PMD band definitions are compiled in Sect. 5.1.5 of (EUMETSAT, 2015) or Table 5 by Munro et al. (2016).

Channel		PMD	approximate	RT
PP	SP	band	w/l range	wavelength
1	9	6	380 … 384 nm	382 nm
2	10	7	400 … 429 nm	413 nm
3	11	8	434 … 492 nm	460 nm
4	12	9	495 … 549 nm	519 nm
5	13	10	553 … 556 nm	554 nm
6	14	11	568 … 613 nm	589 nm
7	15	12	618 … 662 nm	639 nm
8	16	14	794 … 804 nm	799 nm
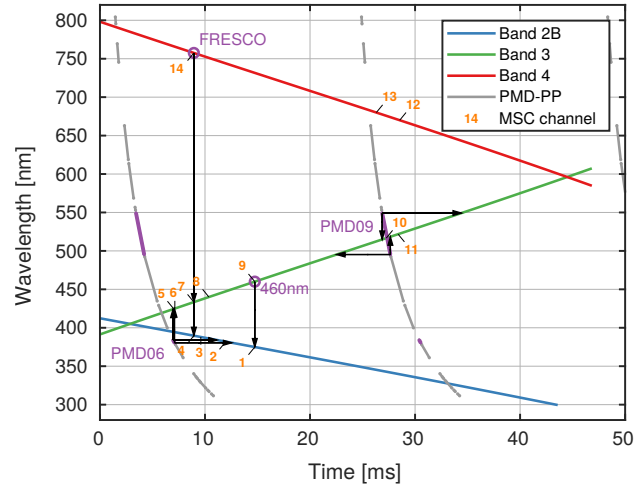
Figure 3. Spatial aliasing of GOME-2 for MSC and PMD bands in time-wavelength space. Radiometric and spatial correlation is expected maximal at the respective intersections. Note that the PMD read-out is faster (steep slope of gray lines) and at higher frequency compared to the MSCs. The second PMD readout (m=1) begins after 23.4375 ms (EUMETSAT, 2015). Horizontal and vertical black arrows indicate the spectral and temporal mapping between GOME-2 bands respectively.

the spatial aliasing between them: MSC channels 2 and 10 correspond to PMD channels 1/9 and 4/12; MSC data acquired at the same time but in different bands are sampled by MSC channels 1 and 9 in bands 2B and 3, respectively, and MSC channels 4, 7, and 14 in bands 2B, 3, and 4, respectively. The correlation of MICRU CF depending on spatial alignment is investigated in Sect. 3.3.3.

9

Table 3. List of external data sets applied in MICRU (see text for details).

Name	Symbol	Reference(s)	Native data resolution		Comment
			temporal	spatial	
Land sea mask	LSM	Wessel and Smith (1996), NOAA (2018)	—	≈ 178 m	GSHHG coast line database, rev. 679
Surface elevation	h	USGS (2018)	—	30 arcsec	GTOPO30, U.S. Geological Survey
Snow concentration	—	Hall and Riggs (2016)	8 d	0.05°	MODIS Terra level 3 (MOD10C2)
Sea ice	—	Cavalieri et al. (1996)	1 d	25 km	compiled passive microwave data
Surface wind speed	W	Dee et al. (2011)	6 h	1°	ERA Interim (ECMWF)
Absorbing aerosol index	AAI	Tuinder et al. (2020)	GOME-2 pixels		GOME-2A level 2, version 1.01
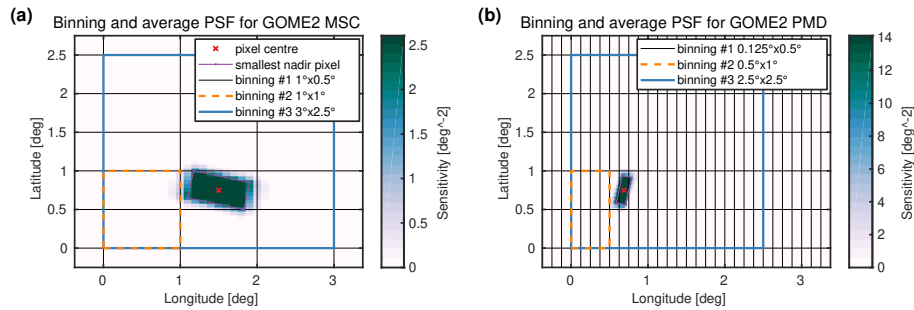
Figure 4. Illustration of average MSC (a) and PMD (b) point spread functions (PSF) used as convolution kernels for LSM, elevation, sea-ice and snow-concentration maps. The PSF correspond to a nominal GOME-2 swath width of 1920 km. The highest resolutions for MSC and PMD lower threshold maps are 0.1° × 0.05° and 0.0125° × 0.05°, respectively, and denoted binning #1 as in Table 6.

2.1.2 Auxiliary data for MICRU

The MICRU algorithm requires several external data sets listed in Table 3. Two different strategies of co-locating these data to the GOME-2 observations are applied depending on the spatial resolution. Data provided at spatial resolutions significantly higher than the generic GOME-2 resolution are convolved with the respective average MSC and PMD point spread function (PSF) as depicted in Fig. 4. The average PSFs are derived from all forward scan pixel edges from one orbit of GOME-2A data at latitudes lower than 55°. This approach simplifies the interpolation of auxiliary data on GOME-2 observations because a linear interpolation can be performed based on the GOME-2 pixel center alone while providing still sufficient spatial accuracy. Data provided at coarser resolutions than GOME-2 are linearly interpolated based on the GOME-2 pixel center without prior convolution.

MICRU features a separate T_{min} parametrisation for measurements over land and ocean, respectively. An accurate description of the land and water transition is therefore crucial for the accurate interpolation of T_{min} at coasts. An algorithm specifically

developed for MICRU derives the fraction of water and land in each satellite pixel at high resolution. As input, the land sea mask (LSM) compiled from revision 679 of the GSHHG coast line database (Wessel and Smith, 1996; NOAA, 2018) is applied. The polygon data from *intermediate* GSHHG resolution neglecting polygons smaller in area than one GOME-2 pixel is first sampled at $0.1° \times 0.05°$ and $0.0125° \times 0.05°$ for MSC and PMD, respectively, and then convolved with the corresponding PSF (cf. Figure 4). The convolution yields a global map of fractional land cover ranging between 0 and 1 representing complete water and land coverage, respectively. Hence, $T_{\min}$ values for land and ocean may be interpolated for each satellite pixel based on the convolved land cover map. The interpolated fractional land cover values are later also used for flagging (Sect. 2.5.3).

The second important input is the surface elevation h required for the inversion of the LER (Sect. 2.2). Elevations maps are inferred based on GTOPO30 raw data (USGS, 2018), which are averaged on a $0.05° \times 0.05°$ grid, and convolved with a mean PSF sampled on the same grid resolution. Interpolation to GOME-2 resolution is again performed applying nearest neighbour interpolation.

Snow and sea ice data are queried to flag possible interferences from highly reflecting surfaces during post-processing (Sect. 2.5.3). Snow data is imported from MODIS Terra measurements with a similar equator-crossing time of 10:30 in descending node similar to GOME-2. Hence, possible effects of different orbital parameters are supposed to be reduced. We used the 8-day composite MOD10C2 product (Hall and Riggs, 2016). Spatio-temporal interpolation uses the nearest neighbour method based on spatially convolved 8-day maps as described above.

Sea ice data is provided by the National Snow & Ice Data Center (NSIDC) and integrates micro-wave measurements from different sensors (Cavalieri et al., 1996). It has a native resolution of 25 km×25 km, which is convolved using average PSFs on 0.1° resolution before merging to GOME-2. Data voids at the poles are filled with values from the nearest valid latitude. Unfortunately, there is no information on the sea ice concentration close to shores in the applied data set. This limitation leads to interferences at shores at high latitudes because GOME-2 pixels possibly affected by sea ice may not be filtered a priori.

Information on wind speed for the calculation of contributions from sun glitter is extracted from ERA-Interim data provided by the European Centre for Medium-Range Weather Forecasts (ECMWF) (Dee et al., 2011). ECMWF 10 m-wind fields are used to parametrise sun glitter. As proposed by Ebuchi and Kizu (2002), the ECMWF wind fields are divided by a factor of 0.918 to approximate the wind speed at 41 ft (≈ 12.5 m) above the surface, which is required as input for the sun glitter model by Cox and Munk (1954a). This factor corresponds to a drag coefficient of 0.0015 assuming neutral stratification (Ebuchi and Kizu, 2002). ECMWF data is imported at 1° and 6 h spatial and temporal resolution, respectively. Spatially, nearest neighbour interpolation is applied based on GOME-2 pixel centers.

Absorbing aerosol indices (AAI) are also used to mask measurements potentially biased by aerosol effects (AAI > 2). For this purpose, AAI data inferred from GOME-2 measurements at both MSC and PMD resolutions is used (Tuinder et al., 2020). The reflectances used for the determination of the AAI at MSC resolution are centred at 340 and 380 nm. For the AAI at PMD resolution, PMD-PP bands 4 and 6 at 338 and 382 nm are applied, respectively. Hence, no interpolation is required to merge MICRU and AAI data.

Table 4. Definition of LUT nodes: reduced SZA μ_0, reduced VZA μ, RAA ϕ, surface height h, and surface LER. The 5-D LUTs are calculated for 19 wavelengths λ.

Parameter	Nodes
$\mu_0 = \cos\theta_0$	1.00, 0.975, 0.95, 0.90, 0.85, 0.80, 0.75, 0.70, 0.65, 0.60, 0.55, 0.50, 0.45, 0.40, 0.35, 0.30, 0.25, 0.20, 0.15, 0.10, 0.05 (21 total)
$\mu = \cos\theta$	1.000, 0.9875, 0.975, 0.950, 0.925, 0.900, 0.875, 0.850, 0.825, 0.800, 0.775, 0.750, 0.725, 0.700, 0.675, 0.650, 0.625, 0.600, 0.575, 0.550, 0.525, 0.500, 0.475, 0.450, 0.425, 0.400, 0.375, 0.350, 0.325 (29 total)
ϕ [°]	0 ... 180, in steps of 15 (13 total)
h [km]	0, 1.4, 3, 4.8, 7 (5 total)
LER	0 ... 1, in steps of 0.1 (11 total)
λ [nm]	375, 382, 388, 389.7, 413, 424.5, 425, 433.4, 440, 460, 519, 521.8, 554, 589, 639, 670, 681, 757.5, 799 (19 total)

2.2 RT calculations and inversion of LER

The conversion between surface LER and measured TOA reflectance R applies a look-up table (LUT) based on reduced reflectances $\hat{R} = I/E_0 = R\cos\theta_0/\pi$. The LUT entries are pre-computed using the SCIATRAN software version 3.7.1 (Rozanov et al., 2014; IFE-Bremen, 2018). The LUT has 5 dimensions: SZA, VZA , RAA, surface height h and surface LER. Table 4 compiles the LUT nodes as well as the wavelengths applied as described in Sect. 2.1.1. It needs to be noted that the resolution of the LUTs in LER direction may appear rather coarse. However, the difference of the obtained results to preliminary RT computations featuring a 10 times higher resolution were found to be < 0.001 in the UV and even one order of magnitude less in the red spectral region. The LUT nodes in SZA and VZA direction are defined in reduced angles $\mu_0 = \cos\theta_0$ and $\mu = \cos\theta$, respectively, in order to provide more nodes at angles featuring larger gradients. The linear interpolation between the nodes is performed in θ_0 and θ space, respectively, in order to increase numerical stability at nadir.

The vector RT calculations are performed in spherical geometry based on a US standard atmosphere with 1013 hPa surface pressure at $h = 0$ m and accounting for atmospheric refraction. The surface is treated as a Lambertian reflector. The model accounts for molecular absorption by O_3 and O_4. The O_3 column is fixed to 250 Dobson Units (DU) in order to reduce the number of required input parameters. This simplification may affect MICRU retrievals within the Ozone Chappuis band, most notably PMD channels 6 and 14, and, to a lesser extent, MSC channels 11 and 12. Preliminary results, however, showed that errors are on average negligible as the empirical approach of MICRU reduces the influence of systematic errors. Aerosols and Raman scattering are not included in the simulations.

From the LUT, the $\hat{R}(\text{LER})$ relation is interpolated for all observation geometries except for $h < 0$ km, which are tweaked to $h=0$ km. $\hat{R}(\text{LER})$ is monotonic and, therefore, $\text{LER}(\hat{R})$ can be readily inverted. We apply linear interpolation to infer $\text{LER}(\hat{R})$.
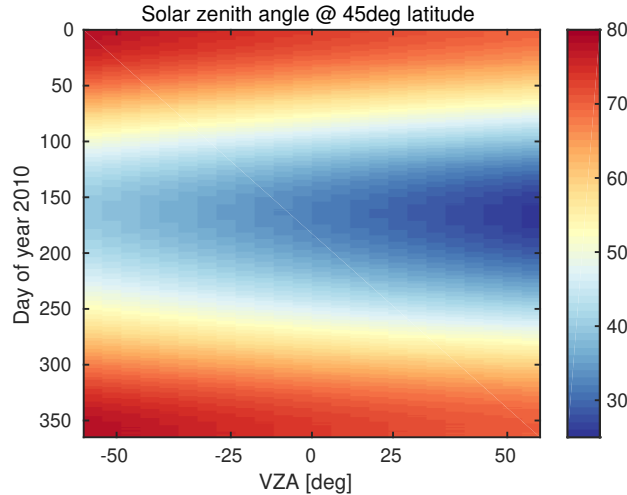
Figure 5. SZA depending on time and VZA at 45°N latitude. Data bins correspond to 24 discrete forward scan pixels and individual days in x- and y-direction, respectively. GOME-2A performs a sun-syncronous orbit at a fixed inclination to the sun. Hence, the SZA unambiguously depends on time, VZA, and latitude.

2.3 T_{min} retrieval

The T_{min} MICRU algorithm requires a certain number of measurements in order to constrain its model parameters using observations not contaminated by clouds. For the description of the algorithm, we define a base set of measurements Ω_0, which are spatially and temporally correlated. It is noted that Ω_0 is a subset of all available measurements depending on grid resolution, measurement resolution, time period, surface structure, and cloud statistics. Section 2.5.1 describes the implementation of the subsetting process.

MICRU defines T_{min} depending on the measurement geometry (θ_0, θ, ϕ), geolocation, and time t. T_{min} is not a true LER because it contains geo-physical and instrumental information. This information is not separated within MICRU and will be treated simultaneously as the ultimate goal is to determine a parametrisation of T_{min} as accurately as possible. In general, it is not possible to parametrise T_{min} in full (θ_0, θ, ϕ)-space due to the sun-synchronous orbit of GOME-2 (Sect. 2.1.1). At every latitude, the dependencies of SZA and RAA on both VZA and time repeat annually. The dependence of SZA and RAA on VZA and time are exemplarily depicted for 45°N latitude in Figs. 5 and 6, respectively. It is therefore sufficient to parametrise the observation geometry (in each bin) by θ and t.

Ω_0 typically contains a significant number of observations contaminated by clouds. Cloudy observations need to be filtered in order to retrieve a T_{min} parametrisation based on cloud-free observations. Therefore, an iterative filter algorithm to find the lower accumulation point by Grzegorski et al. (2006) is presented in Appendix A. Compared to HICRU, however, the MICRU algorithm generalizes from zero to four dimensions.
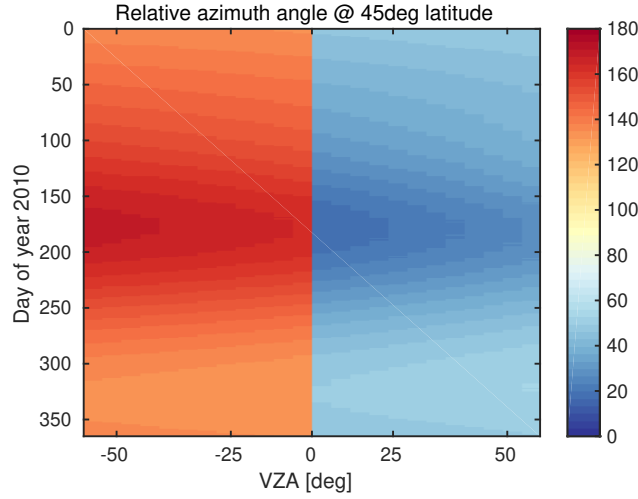
13

Figure 6. Same as Fig. 5, but showing the RAA at 45°N latitude.

2.3.1 $T_{\min}$ model

The MICRU $T_{\min}$ model is

$$y(\hat{t}, \hat{\theta}, \theta_s, r_g) = a_0 + a_t \hat{t} + y_a(\hat{t}, \hat{\theta}) + a_s \cos \theta_s + a_g r_g \tag{4}$$

applying 4 independent variables $\hat{t}$, $\hat{\theta}$, θ_s, and r_g and 7 dependent variables a_0, a_t, a_p, a_{a0}, a_{a1}, a_s, and a_g, which are intro-
5 duced in the following. Equation (4) is an empirical parametrisation accounting for actual and systematic effects of the lower threshold, which are not linearly independent in general.

Equation (4) applies normalized time $\hat{t}$ and normalized VZA $\hat{\theta}$ instead of t, and θ as independent model parameters to improve fit stability. Assuming t measures in unit days, we then define the normalized time

$$\hat{t} = \frac{t - t_0}{365.25 \,\text{days}} \tag{5}$$

10 measuring in unit years centred on t_0. In case of GOME-2A, t_0 is chosen so that $\hat{t} = 0$ for 1 January 2010. θ measured in unit degrees and the normalised VZA

$$\hat{\theta} = \theta / 55° \tag{6}$$

ranges between -1 and 1.

The two further model parameters are the scattering angle θ_s defined by

15 $$\cos \theta_s = \sin \theta_0 \sin \theta \cos \phi - \cos \theta \cos \theta_0 \tag{7}$$

and the reflected sun angle θ_r defined by

$$\cos \theta_r = \sin \theta_0 \sin \theta \cos \phi + \cos \theta \cos \theta_0 \,. \tag{8}$$

14
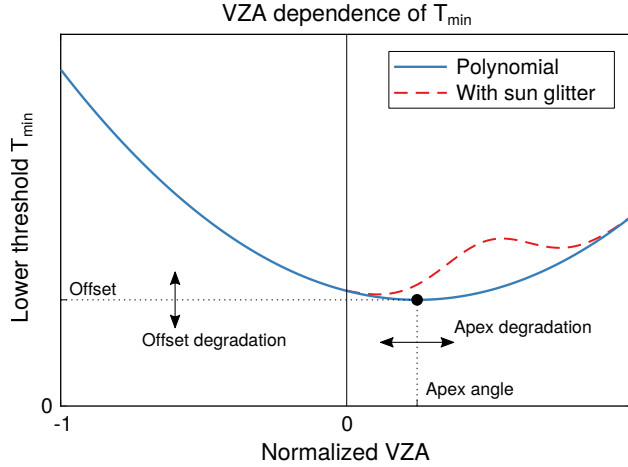
Figure 7. A second order polynomial parametrised by apex angle and curvature models systematic VZA dependencies of the lower threshold T_{min}. Degradation may affect both apex angle and offset. The position, amplitude, and width of the sun glitter contribution depends on geometry and wind speed.

Both angles are also illustrated in Fig. 1.

The right-hand side of Eq. (4) is the sum of the following terms.

1. The constant offset a_0 accounts for the mean surface LER.

2. Residual line-of-sight dependencies are modelled by a second order polynomial (Fig. 7), which is parametrised by the normalised apex angle $\hat{\theta}_a$ and curvature a_p:

$$y_a(\hat{\theta}) = a_p\left((\hat{\theta} - 2\hat{\theta}_a)\hat{\theta} + \hat{\theta}_a^2\right). \tag{9}$$

3. Temporal degradation is assumed by a linear offset degradation factor a_t and the time dependent normalised apex angle

$$\hat{\theta}_a(\hat{t}) = a_{a0} + a_{a1}\hat{t} \tag{10}$$

as indicated by the arrows in Fig. 7. Tests applying a second order polynomial or an exponential to model degradation of GOME-2 MSC data were not successful. The former does not improve results significantly and the latter deteriorates the stability of the fit.

4. BRDF effects are modelled by an empiric $\cos\theta_s$ term. Its inverse shows a similar behaviour like the Li-dense kernel for closed canopy (Li and Strahler, 1992; Wanner et al., 1995) but does not require any further parameters. This term models the annual oscillations particularly visible at the western swath edge in Figs. 8(d,e) and 9(d,e).

The cosine normalises the parameter improving the fit stability. As tests, we replaced the empirical term either with the precise Li-dense kernels, a reduced $\cos\theta_r$ term for surface effects, $\csc\theta_s$, or $\cos^2\theta_s$ but all of these test resulted in less accurate surface fits and, hence, increased T_{min} noise compared to our final choice.
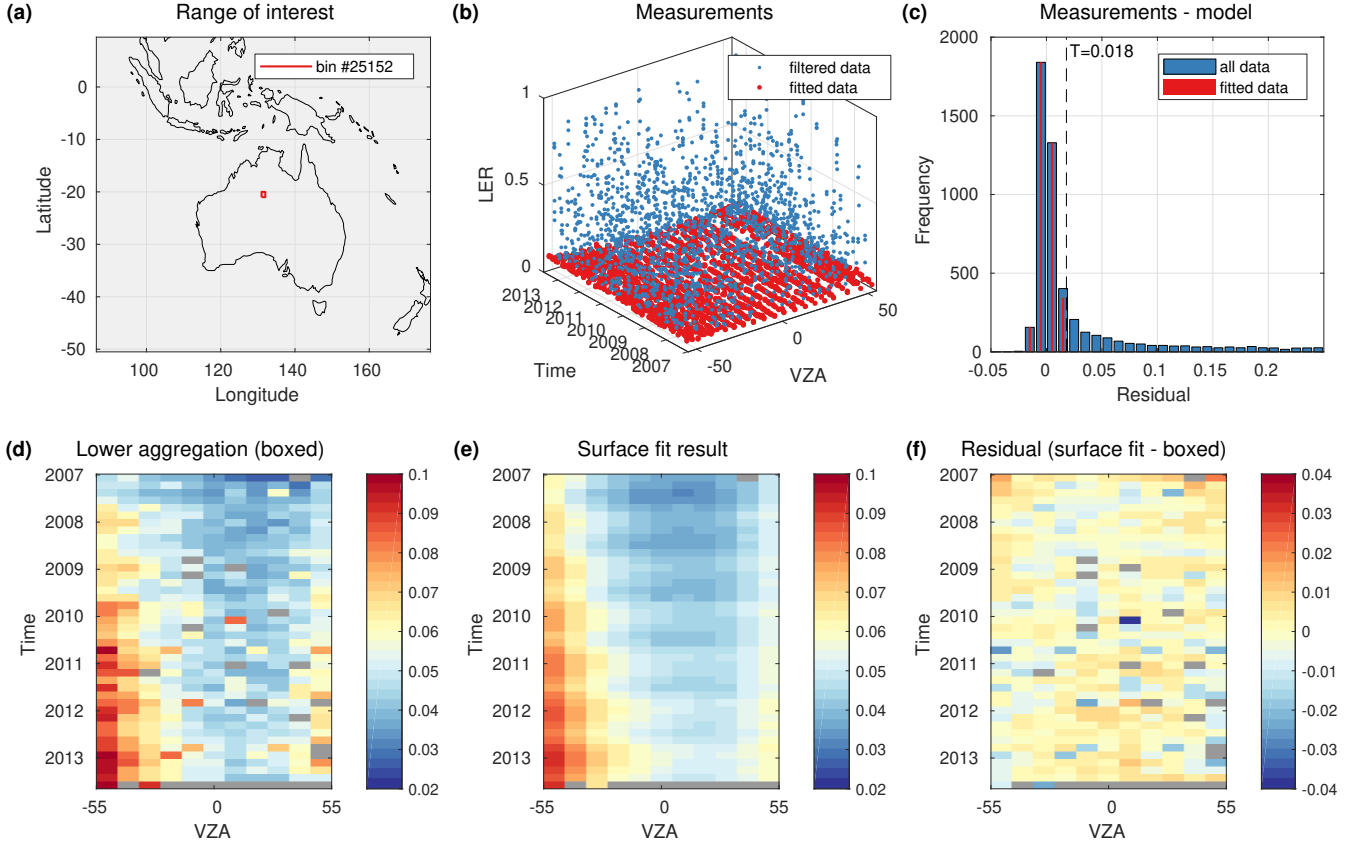
15

Figure 8. Example surface fit for MSC channel 2 at 382 nm and applying binning 2 over Australia: (a) The bin of interest ranges from 131°E to 132°E longitude and from 20°S to 21°S, (b) 3D representation of measurement set Ω_0 (blue) and finally fitted set Ω_I (red), (c) frequency distribution of the fit residual, (d) lower accumulation point within each individual 0D-box, (e) surface fit result using model Eq. 4; and (f) difference of (d) and (e). The discretisation chosen for (d)–(f) displays a trade-off between accuracy and noise for the sake of clarity. Negative VZA denote the western half of the swath.

5. The contribution of sun glitter on water surfaces is parametrised based on the isotropic sun-glitter model suggested by Cox and Munk (1954a, b). This model was found to be sufficiently accurate for MICRU and, according to Zhang and Wang (2010), performs reasonably well compared to competing models in their study. We apply the glitter reflectance r_g as provided by Eqs. (1–4), (9), and (15) in (Zhang and Wang, 2010). According to Cox and Munk (1954a), the mean square slope of the clean surface is

$$\sigma^2 = 0.003 + 5.12 \times 10^{-3}W \tag{11}$$

where W is the wind speed at 41 ft (≈ 12.5 m) above sea level, which is computed from 10 m-wind speeds as described in Sect. 2.1.2. The index of refraction is set to n=1.34 (Blum et al., 2012). Hence, r_g as illustrated in Fig. 7 is a function of θ_0, θ, ϕ, and W.
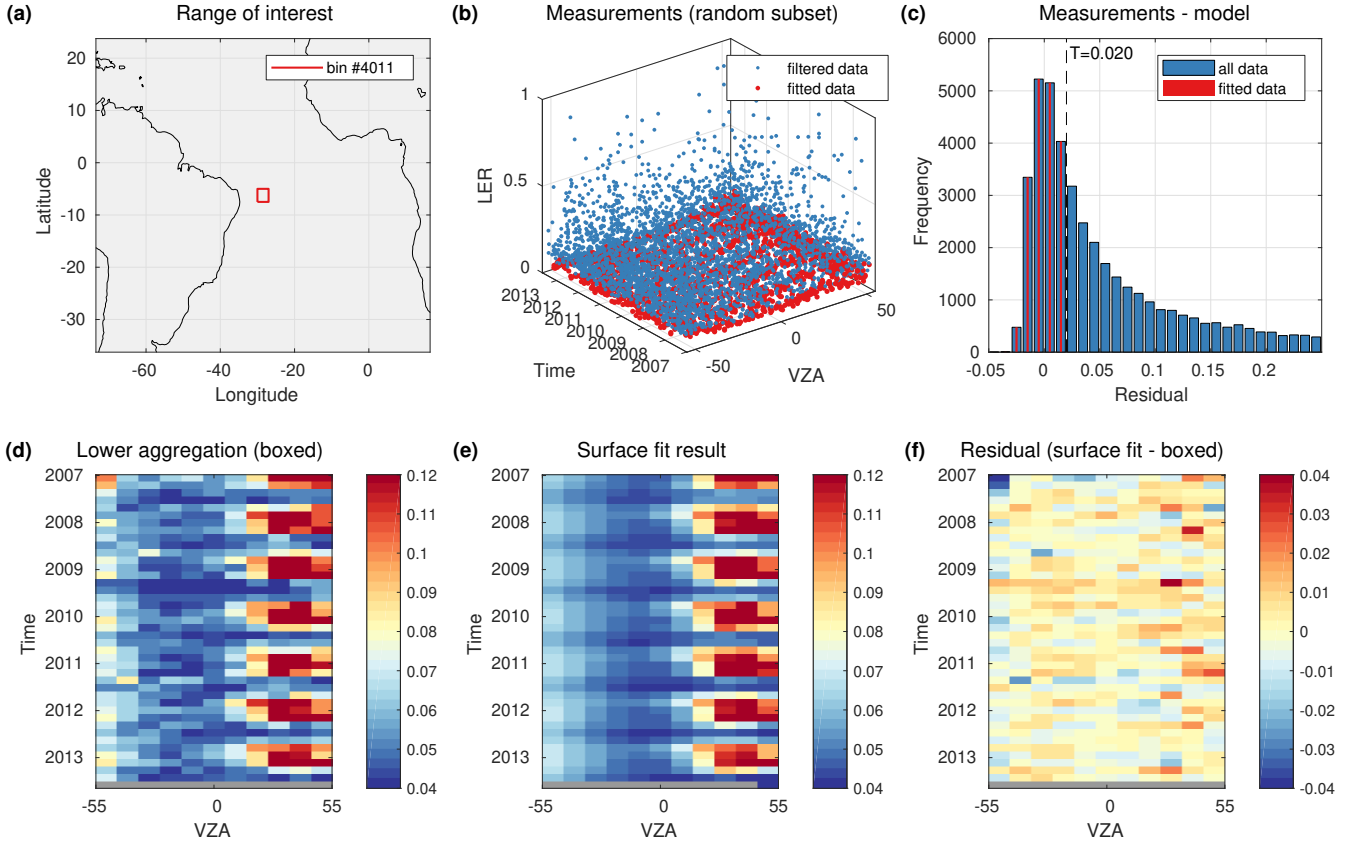
Figure 9. Same as Fig. 8, but for MSC channel 10 at 516.7 nm and applying binning 5 over the equatorial Atlantic. The set of measurements ranges from 30°W to 27°E longitude and from 7.55°S to 5°S.

Table 5 summarizes the $T_{\min}$ model parameters and the bounds of the constrained fit. The parameters a_t and a_{a1} are constrained to 0 for MSC channels 12, 13, and 14 as preliminary evaluations showed that degradation can be neglected for these channels, which furthermore improved signal-to-noise. Clearly, the above model is a trade-off between accuracy and stability. Choosing a model based on more parameters would increase the accuracy of modelling the physical effects but degrade the stability of the fit limited by the number of cloud-free observations.

2.4 Determination of $R_{\max}$

The upper threshold $R_{\max}$ is defined as the reflectance of a Lambertian surface with an albedo of 0.8 located at 7 km altitude. This simple cloud model, which was adopted from McPeters et al. (1996) and Koelemeijer et al. (2001) improves applicability to retrievals building on MICRU cloud products because cloud correction algorithms in many trace gas retrievals apply the same model (Vasilkov et al., 2017). Furthermore, the assumptions on cloud RT need to be consistent between cloud and trace

Table 5. List of $T_{\min}$ model parameters with initial values (β_0) and parameter bounds of the constrained non-linear fit.

Symbol	Comment	β_0	Range
a_0	offset	variable	$-\infty \ldots \infty$
a_t	offset degradation	0	$-0.02 \ldots 0.02^*$
a_p	polynomial amplitude	0.02	$0 \ldots 0.2$
a_{a0}	normalised apex angle	0	$-5 \ldots 10$
a_{a1}	apex degradation	0.02	$-0.5 \ldots 0.5^*$
a_s	scattering amplitude	0	$-0.5 \ldots 0.2$
a_g	glitter amplitude	0.2	$0 \ldots 0.4$

*: Degradation constrained to 0 for MSC channels 12, 13, and 14.

gas retrievals for AMF calculation. Volumetric clouds, on the other hand, are more complex to simulate and would require more parameters, which are unknown a priori.

$R_{\max}$ is assumed independent of geolocation and time and calculated applying the look-up-tables described in Sect. 2.2 and Table 4. A quantitative discussion of choosing $T_{\max} = 0.8$ as a cloud albedo for an Lambertian cloud model as upper threshold
5 is provided by Koelemeijer et al. (2001), Ahmad et al. (2004), and Stammes et al. (2008). As a consequence, however, very bright clouds exceeding $T_{\max} = 0.8$ will result in a MICRU CF > 1. Some CF algorithms normalize CF > 1 to 1, but MICRU rather provides these exceptionally high values as additional output.

It needs to be noted that instrumental degradation may introduce a systematic bias of the CF, which will be strongest for large CF. Most importantly for MICRU, the influence of the applied cloud model on the CF accuracy decreases with CF.

10 **2.5 Implementation**

The MICRU algorithm consists of several consecutive steps: Import of data, RT simulation, merging of external data, determination of $R_{\min}$, determination of $R_{\max}$, and finally the computation of CF. The following subsections detail the implementation of the methods described above in the MICRU framework.

2.5.1 Geospartial subsetting

15 The $T_{\min}$ algorithm (Sect. 2.3) requires a spatio-temporal subset of satellite measurements with a sufficient number of measurements. Section 2.1.2 describes how GOME-2 pixels are reduced to their centres. Hence, geospatial locations can be readily indexed and assigned to geospatial subsets. All MICRU computation refers to pixel centres rather than their actual area. This simplification takes advantage of the fact that the surface is scanned by almost identically shaped ground pixels over the evaluated measurement period, and, therefore, measurements with identical pixel center are congruent.
20 Temporally, larger subsets should be favoured over smaller ones unless there are significant changes of surface properties or the instrument response degrades much differently than considered in the model (Sect. 2.3.1). For example, for MSC binning

1 there are 400 equatorial bins over land with 15 or less measurements considered cloud-free by the T_{min}-retrieval despite applying a study period of 77 months. Longer time-series increase the probability of including measurements not contaminated by clouds (Krijger et al., 2007).

Spatially, a very small geospatial interval would be beneficial in order to increase the correlation between measurement and
5 collocated T_{min} where the true surface is inhomogeneous. However, there is a trade-off because the probability of including enough cloud-free measurements decreases if the geospatial interval becomes too small. If there are not enough cloud-free measurements, the accuracy of the fit degrades. Furthermore, spatial subsampling can be avoided using spatial sampling intervals larger than the native resolution of the measurements defined by its PSF.

Within MICRU, the geospatial subsetting is called *binning*, which is performed on a longitude-latitude grid. Each binning
10 corresponds to a global map at a different resolution. The T_{min} retrieval is independently applied on each binning, whose definition distinguishes between measurements over ocean and land. The results are then merged to form complete parametrisations of T_{min} for ocean and land surfaces independently. There are several advantages of this approach.

   1. If, for some reason, the fit fails using the highest resolution, the parametrisation results from evaluation using larger bins may be used instead.

15 2. The bin dimensions can be adapted to the surface type: smaller and approximately quadratic over land, larger and less depending on longitude over ocean.

   3. It enables independent parametrisations for the two different surface types. Hence, T_{min} gradients at the coast can be mitigated.

Table 6 details and Fig. 4 illustrates the MICRU binnings for GOME-2 MSC and PMD evaluations, respectively. Figure 8(a)
20 illustrates the dimension and location of bin 25152 of MSC binning 2.

The entire data set needs to be resorted with respect to geolocation instead of acquisition time for computational purposes. Therefore, input data is organised in geospatial *tiles* as defined in Table 6, which reduces the memory requirement for a process performing the iterative surface fitting per bin (Appendix A). Tiling furthermore enables parallel processing of MICRU on a cluster because each sub-process only requires a small portion of the observational data. Hence, scaling MICRU to sensors
25 different from GOME-2 is straight-forward by adjusting the tile resolution.

2.5.2 T_{min} maps

The following filters are applied on the input data prior to the T_{min}-retrieval:

   – Filter measurement in ascending node to avoid ambiguities of the time and latitude dependent θ-selection.

   – Filter viewing modes other than the nominal 1920 km swath (EUMETSAT, 2015). For example, this filter excludes *nadir*
30   *static* and *narrow swath* orbits as well as data recorded after June 2013.

   – Filter SZA larger 85°.

19

Table 6. Spacing of meridians ($\Delta\lambda$) and parallels ($\Delta\varphi$) for the definitions of tiling and binnings for MSC and PMD evaluations, respectively. Binning resolutions depend on surface type: land (s = 1) and ocean (s = 2).

	#	s	MSC $\Delta\lambda$	MSC $\Delta\varphi$	PMD $\Delta\lambda$	PMD $\Delta\varphi$
tiling			45°	15°	15°	5°
binning	1	1	1°	0.5°	0.125°	0.5°
	2	1	1°	1°	0.5°	1°
	3	1	3°	2.5°	2.5°	2.5°
	4	2	1°	0.5°	0.125°	0.5°
	5	2	3°	2.5°	2.5°	2.5°
	6	2	15°	2.5°	15°	2.5°
	7	2	45°	2.5°	15°	5°

- Filter data possibly affected by solar eclipses as defined in Appendix B of (Tilstra et al., 2017a).

- Filter times of instrumental malfunction as listed in (EUMETSAT, 2014).

- Filter measurements with AAI > 2.

- Filter measurements, which include neither > 90% land nor > 90% ocean.

- Over ocean, filter measurements with $\theta_r < 8°$ (sun glitter).

Then, the $T_{\min}$-algorithm (Sect. 2.3) is applied on the measurement tuples within each bin. Figures 8 illustrate the $T_{\min}$-algorithm applied on MSC channel 2 for a $1° \times 1°$ bin over Australia. Similarly, Fig. 9 illustrates the same on MSC channel 10 data at 516.7 nm over the Atlantic Ocean. This step is repeated for all binnings listed in Table 6 and all channels listed in Tables 1 and 2 for MSC and PMD, respectively. For diagnostic purposes, the number of iterations i, the number of included measurements N, the number of fitted measurements N^*, threshold τ, and residual statistics are intermediately stored alongside the fit result β for diagnostic purposes.

Tiled $T_{\min}$ results are stitched together to form global maps for all binnings and channels. For each channel, the maps of different resolutions need to be merged in order to obtain two complete and unambiguous β maps, respectively one for ocean and one for land. The steps of the merging process are detailed in Appendix B. Appendix C presents exemplary results for MICRU channel 02.

Table 7. Flags applied by the MICRU algorithm allowing for individual filtering.

Flag	Description
Coast warning	if $>10\%$ land and $>10\%$ ocean
AAI warning	if $AAI > 2$
Snow warning	if MODIS 8-day snow concentration $>5\%$
Sea ice warning	if micro-wave sea-ice concentration $>5\%$
Sunglint warning	if $\theta_r < 36°$ over ocean or $\theta_r < 8°$ over land
Sunglint risk	if $\theta_r < 8°$ over ocean
Statistics warning	if $N < 80$ or if the mode of $R > 0.1$
Coarse mode	if the applied binning is neither 1 or 4
Extrapolated parameters	if the applied parametrisation is extrapolated

2.5.3 CF calculation and flagging

Once $R_{\min}$ and $R_{\max}$ are determined, c can be computed using Eq. (1) for all MICRU channels separately. The MICRU data set furthermore provides several quality flags listed in Table 7. MICRU MSC and PMD data are merged with three aliasing offsets $m = 0, 1, 2$ (Sect. 2.1.1) for the investigation of the spatial aliasing in Sect. 3.3.3.

2.6 Comparison data

For GOME-2 MSCs, FRESCO+ cloud fractions evaluated at the O_2-A band are widely-used (Wang et al., 2008; TEMIS, 2019). In this study, three different versions of the FRESCO cloud fractions are applied in order to study the particular differences with respect to background map generation and residual VZA dependence:

FRESCO L1b denotes the CF data shipped with the L1b files from EUMETSAT, also denoted FRESCO version 6. This FRESCO version applies a background map compiled from MERIS measurements over land and GOME-1 surface LER over ocean (Popp et al., 2011; Tilstra et al., 2017b).

FRESCO v7 is the first FRESCO version applying a background LER map derived from GOME-2 measurements themselves (Tilstra et al., 2017b).

FRESCO v8 is the most recent version applying a directional LER database compiled from GOME-2 measurements. The resolution at the coast and over specific regions is increased to reduce interference from different surface types within one GOME-2 pixel (Wang et al., 2018).

FRESCO L1b data of the entire evaluation period is included in this study. For FRESCO v7 and v8, however, comparisons to MICRU are limited to selected months. For FRESCO v7, it is January, April, July, and October 2010. For FRESCO v8, it is

January to December 2010 plus April 2007 and 2013 (cf. Figs. 24(b) and (c)). The applied FRESCO products do not correct for interferences with sun glitter. It is furthermore noted that MICRU data are ignored in the comparisons in Sect. 3.4 if respective OCRA/FRESCO data are invalid.

The second batch of comparison data are OCRA cloud fractions inferred from GOME-2 PMD measurements described by Lutz et al. (2016). In its actual version 3.0, OCRA is mainly developed as the operational CF product for the S5P/TROPOMI mission (Loyola et al., 2018). In contrast to FRESCO, OCRA applies an empirical correction scheme for the sun glint effect (Lutz et al., 2016). OCRA CF are officially provided at PMD resolution and are therefore suited to be compared directly to MICRU PMD results. OCRA results mapped to MSC resolution are denoted OCRA MSC. OCRA, however, does not assume a constant cloud albedo of 0.8 as upper threshold resulting in systematic differences between both products. We therefore introduce scaled OCRA results as a third OCRA data set. The scaling is performed requires the cloud albedo CA_{ROCINN} retrieved by the retrieval of cloud information using neural networks (ROCINN) algorithm (Loyola et al., 2007, 2011, 2018), which is therefore only available at MSC resolution. We define the scaled OCRA CF $CF_{OCRA\_fixed\_albedo}$ by

$$CF_{OCRA\_fixed\_albedo} = CF_{OCRA} \frac{CA_{ROCINN}}{0.8} \tag{12}$$

denoted by OCRA_fixed_albedo below.

The selected cloud products define the upper threshold differently. FRESCO applies a Lambertian (or reflecting) cloud model – like MICRU – and OCRA applies a color space approach for the upper threshold (Wang et al., 2008; Lutz et al., 2016). Furthermore, the treatment of extreme CF significantly differs between MICRU, FRESCO, and OCRA. Both FRESCO and OCRA provide normalised CF, which means that CF do not linearly scale with reflectance. OCRA, for example, normalises $CF < 0$ to 0 and $CF > 1$ to 1. For FRESCO, normalisation schemes defer between versions: FRESCO L1b sets $CF < 0$ to 0. For $CF > 1$, all FRESCO version vary the cloud albedo to improve convergence. In contrary, MICRU does not apply any normalisation by default leading to an unlimited CF distribution. We define *cropped* subsets of data: $CF < 0$ are set to 0 and $CF > 1$ are omitted from statistical comparisons (Sect.3.4) in order to avoid systematic bias from different normalisation strategies. It shall be noted that both normalisation and cropping lead to biased mean results. These biases propagate into trace gas retrievals if normalised CF data are applied.

Finally, measurements by the AVHRR/3 (Advanced Very High Resolution Radiometer version 3) instrument are applied as independent measurements for the detection of clouds from the MetOp satellite (Cracknell, 1997; NOAA, 2017; EUMETSAT, 2011). AVHRR is an imager with six spectral channels centred between 630 nm and 12 μm. The spatial sampling of GOME-2 and AVHRR is detailed by Sihler et al. (2017). In this study, AVHRR data of bands 1, 2, and 3a is applied to produce RGB false colour images. Furthermore, an artificial AVHRR cloudmask is constructed, where an AVHRR pixel is assumed cloudy if either the Albedo test, or the T4-T3 test, or the T4-T5 test indicates a cloudy scene (cf. EUMETSAT, 2011).

3   Results

This section starts off with results from the $T_{\min}$ retrieval (Sect. 3.1) and a comparison between MICRU, FRESCO, OCRA based on single, cloud-free swaths (Sect. 3.2). Subsequently, statistical ensembles are applied to intercompare MICRU CF results (Sect. 3.3), and to evaluate differences between the three CF algorithms (Sect. 3.4).

5   Studies on monthly statistics exclude data where

- SZA $\geq 84°$,

- latitudes $\geq 55°$,

- MODIS snow concentration $> 2\%$,

- AAI > 2,

10 - the sunglint risk flag is raised, or

- the coast warning is raised (exception: average maps)

in order to reduce interferences.

3.1 $T_{\min}$ retrieval

Figure 8 illustrates the input measurements and output results of the $T_{\min}$-retrieval (Sect. 2.3) applying MSC channel 2 at
15   382 nm and binning 2 over continental Australia. The blue dots in Fig. 8(b) denote the input data omitting scattering angle θ_s and glitter reflectance r_g dimensions for the sake of clarity. Figure 8(d) shows a matrix of lower aggregation points of LER retrieved independently in discrete boxes defined in the t/θ-plane. The lower aggregation points are retrieved with the same τ as resulting from the surface fit but without parametrisation. The matrix reveals an increasing trend with time and a significant VZA-dependence. The iterative surface fitting result using the same data (Fig. 8(e)) shows a similar but much smoother result
20   due to improved statistics by combining the information from all measurements and applying a parametrised surface model. Figure 8(f) shows the difference between boxed and fitted results indicating average deviations much smaller than 0.04. There are, however, small systematic deviations towards the edges indicating a slight overestimation of $T_{\min}$ at the beginning of the sensing period (2007) and at large VZA and slight underestimation at the end of the period (colder colors for 2013). The histogram of the residual R of LER measurements and modelled $T_{\min}$ is plotted in Fig. 8(c) using the respective colors as in
25   Fig. 8(b). Measurements applied for the final iteration of the surface fit peak between -0.01 and 0, for which a final threshold of $\tau = 0.018$ is applied.

Figure 9, in contrary to Fig. 8, illustrates the application to another MSC channel at 516.7 nm and surface type ocean. Compared to Australia, the fraction of fitted measurements is significantly lower due to a higher probability for clouds. The smaller fraction of fitted measurements is also indicated by a less pronounced peak in the histogram (Fig. 9(c)). There is a
30   significant contribution of sun glitter, which is visible by the annually appearing red areas at positive VZA in Figs. 9(d) and
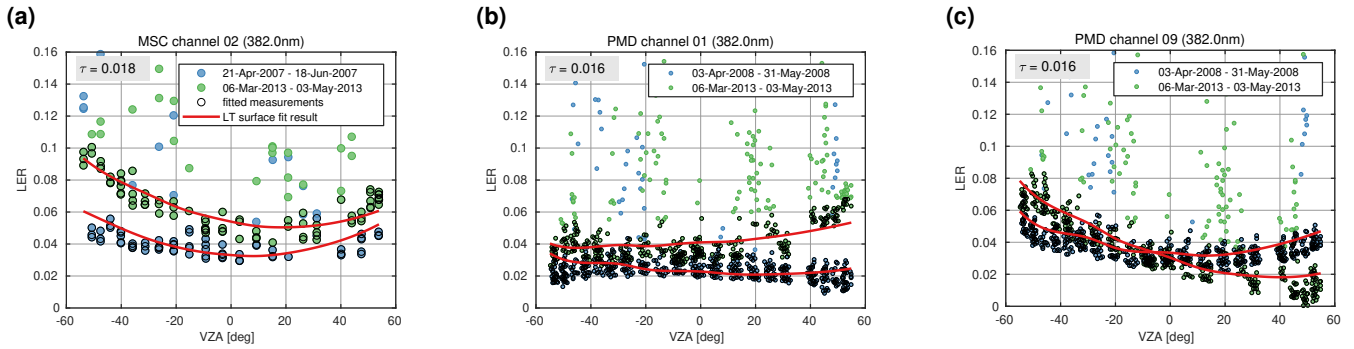
23

Figure 10. Detailed fit results from surface of three GOME-2 bands measured over Australia (cf. Fig. 8(a)), comparing the fit results with measurements selected from the beginning (blue dots) and the end (green dots): (a) MSC channel 02, the fit results (red lines) correspond to 8(f), (b) for PMD-PP, and (c) for PMD-SP. Note the significant differences between the residual VZA-dependences and their trends of three GOME-2 bands measuring at the same wavelength of 382 nm. Note that reflectance measurements below the red line will later result in negative CF.

(e). The scatter in Fig. 9(f) collocated with the regions affected by sun glitter is probably due to poor statistics when calculating the boxed comparison results. The LER in the first, western-most column of boxes seem to be biased low of the order of 0.01 compared to other viewing angles.

Figure 10 investigates trends of the VZA-dependence for the three GOME-2 channels MSC, PMD-PP, and PMD-SP but
5 same spectral region, respectively. Figure 10(a) corresponds to the first and last row in Fig. 8(d/e), indicated by blue and green dots, respectively. Circled dots correspond to the red dots in Fig. 8(b). The red lines correspond to the fit results shown in 8(e). Figure 10(a) reveals a lower threshold increasing with time (≈ 0.02 in total) and a time-dependent VZA-dependence affecting apex VZA and curvature. Figures 10(b) and (c) illustrate the temporal behaviour of the corresponding PMD-PP and PMD-SP measurements. For PMD-PP, the VZA-dependence and its degradation is smallest compared to the other channels. PMD-PP,
10 however, features a significantly larger overall trend compared to PMD-SP in Fig. 10(c). For PMD-SP, the overall trend is small, but the VZA-dependence degrades significantly more than MSC channel 2.

Another estimate of the residual VZA-dependence may be assessed by analysing the cross-track dependence of the lower CF accumulation point displayed in Figs. 11(a) and 12(a) for land and ocean surfaces, respectively. Over land, the small CF accumulate between -0.02 and 0.03 almost evenly over the entire swath. Over ocean, small CF are slightly more scattered. The
15 distribution dilutes significantly and reveals a slight positive bias towards west (negative VZA in Fig. 12).

3.2 Cloud-free observations

Figure 13 compares cloud-free measurements of MICRU, OCRA, and FRESCO over three exemplary sites featuring different surface cover (left to right): rainforest, continental mid-latitudes, and ocean. Independent AVHRR measurements are included to identify essentially cloud-free scans (top row). MICRU MSC and PMD results are specifically obtained at 440 and 460 nm,
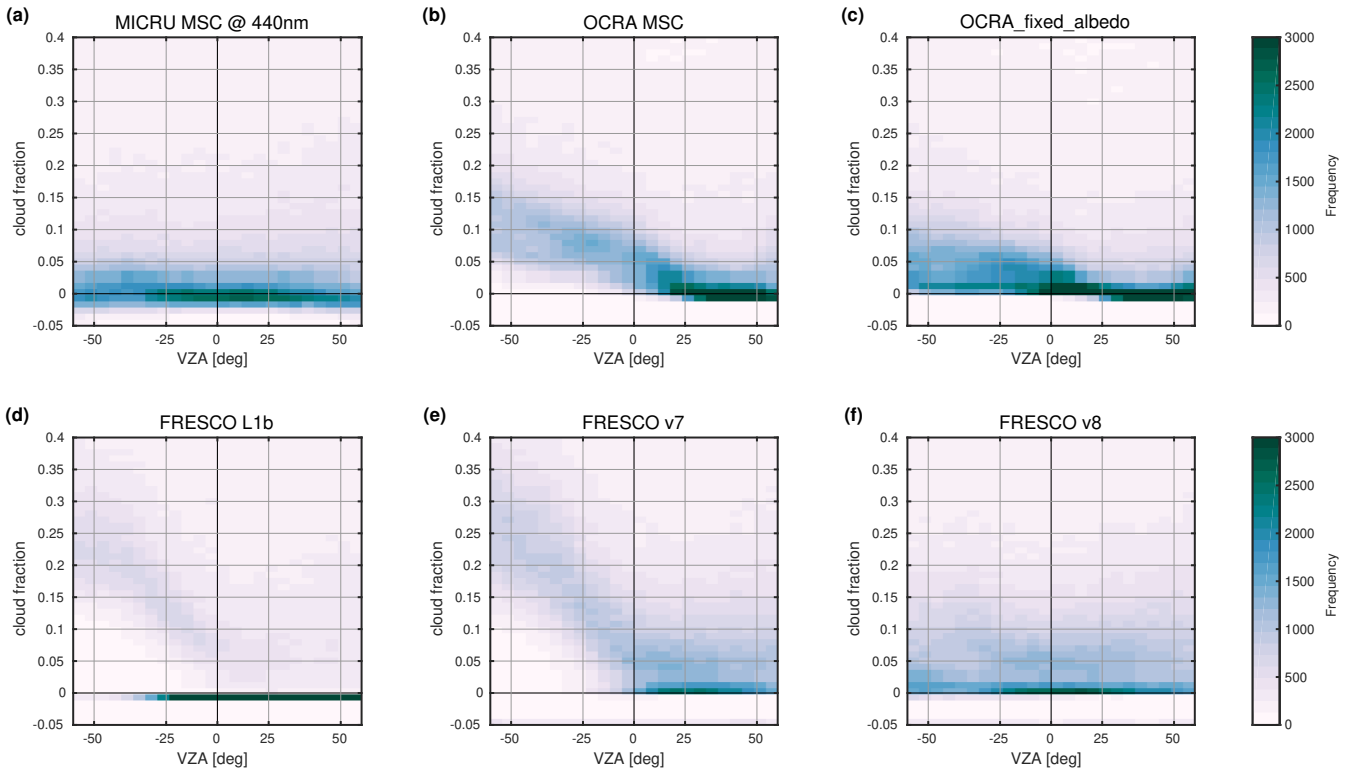
Figure 11. Comparison of viewing angle dependence of small CFs over land between the 55° parallels: (a) MICRU MSC at 440 nm, (b) OCRA MSC, (c) OCRA_fixed_albedo, (d) FRESCO L1b, (e) FRESCO v7, and (f) FRESCO v8. Statistics based on April 2010 data.

respectively. OCRA results are based on PMD measurements between 321 and 804 nm. FRESCO applies the O_2-A band at 757.5 nm.

MICRU MSC and PMD results show no significant cloud-cover where also AVHRR does not detect clouds. Purple colours at the swath edges, however, indicate biased low CF results (Figs. 13(d)–(i) in cloud-free observations over both land and ocean.

5 Over land, the MICRU results are consistent with the AVHRR cloud mask, e. g. CF contributions of singular clouds smaller than the GOME-2 pixel sizes are reproduced in Figs. 13(e) and (h) over North America. The bias of cloud-free observations is small and the colorbar range almost does not resolve the scatter around zero CF.

In case of sunglint, the situation is more complex. In Figs. 13(f) and (i), MICRU measurements scatter significantly as indicated within the area flagged with a sunglint warning (green edges). The scatter is only significant in the eastern swath

10 (orbit 17907) whereas the western swath (orbit 17908) shows almost no scatter. The analysis of the wind fields (not plotted) reveals that wind speeds vary between 0 and 5 m/s for the cloud-free region of the eastern swath and between 3 and 4 m/s in the western swath, respectively. The interpolation of the wind fields is apparently not accurate enough for the eastern swath. The interpolation is limited by a spatial resolution of 1° and a temporal resolution of 6 h. Hence, MICRU CF may be over- and underestimated in case of heterogeneous wind situations and especial for very low winds. We conclude, however, that MICRU
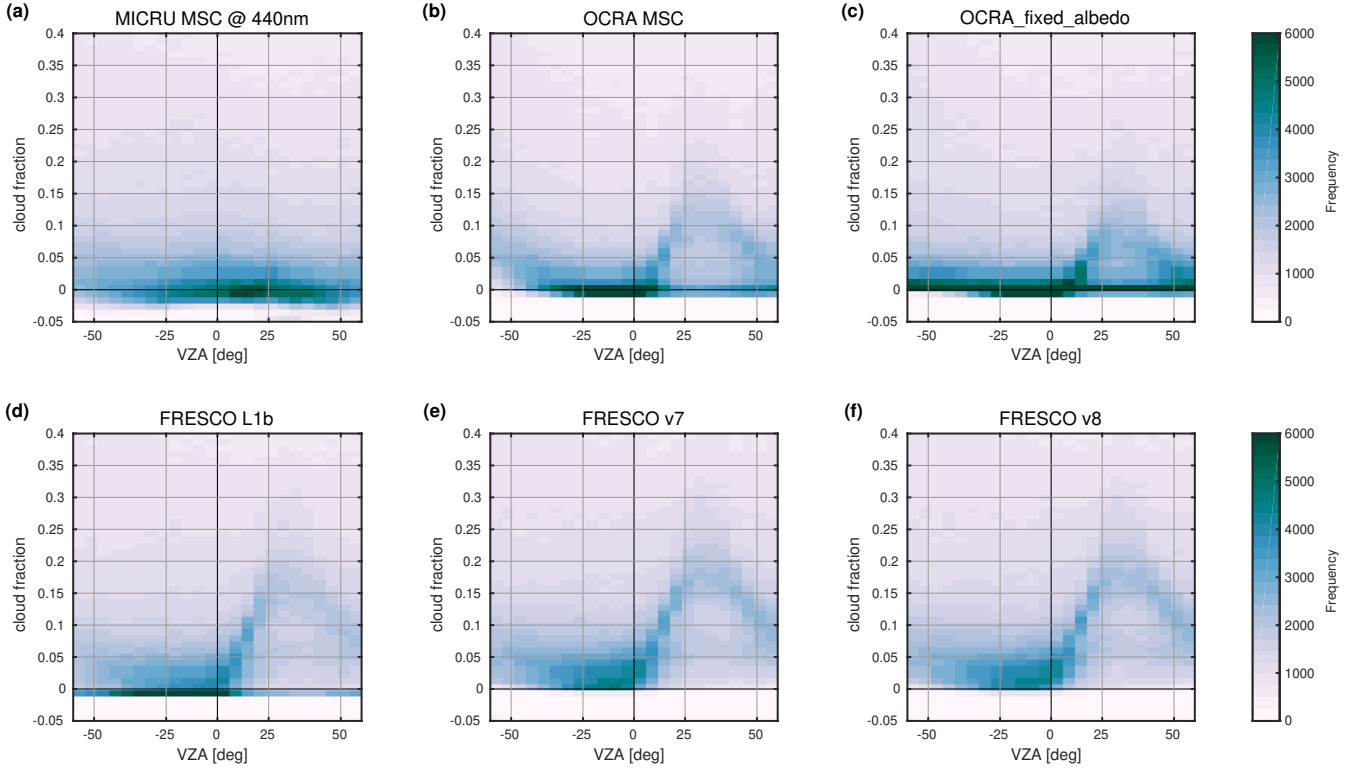
Figure 12. Same as Fig. 11 but over ocean. The influence of sun glitter is evident for positive VZA for most products, even though measurements flagged *sunglint risk* (Table 7) are filtered.

is capable to model moderate R_{min} contributions by sun glitter. When sun glitter is large (in case of low winds), as indicated by yellow colours in the false colour background image of Fig. 13(c), this corrections is less reliable. Therefore, measurements flagged with a sunglint warning are screened from the statistical comparison studies below.

Figure 13 furthermore compares MICRU results to FRESCO and OCRA. Over land, the CF maps of FRESCO L1b and v7 measurements (Figs. 13(j), (k), (m), and (n)) reveal significant positive biases in the western part of the swath. Cloud fractions larger than 20% are detected even though AVHRR and MICRU both detect no clouds. FRESCO v8 displays a significant improvement over Brazil (Fig. 13(p)), whereas CF over North America in Fig. 13(q) are still significantly biased in the west of the swath. Over East India (orbit # 17907), however, all FRESCO versions are significantly biased high (Figs. 13(l), (o), and (r)). Switching to OCRA, Fig. 13(s) reveals significantly smaller positive biases of OCRA over Brazil compared to FRESCO L1b and v7. Over North America (Fig. 13(t)), however, a positive bias and scatter are significant. The biases of OCRA_fixed_albedo at MSC resolution are significantly smaller, especially over Brazil (Fig. 13(v)). Similarly, Fig. 13(x) shows significantly smaller biases over East India compared to the native OCRA results at PMD resolution in Fig. 13(u).

Over ocean (right column in Fig. 13), biases in regions possibly affected by sun glitter are obvious in the FRESCO and OCRA data. FRESCO products are not correcting for this interference leading to systematic positive biases because the increased

intensity is apparently interpreted as reflecting clouds (Figs. 13(l), (o), and (r)). In contrary to FRESCO, OCRA corrects for the sun glint effect in the centre of the affected region (Fig. 13(u)), but interferences still persist for $\theta_r < 36°$, which is flagged by MICRU as sunglint warning.
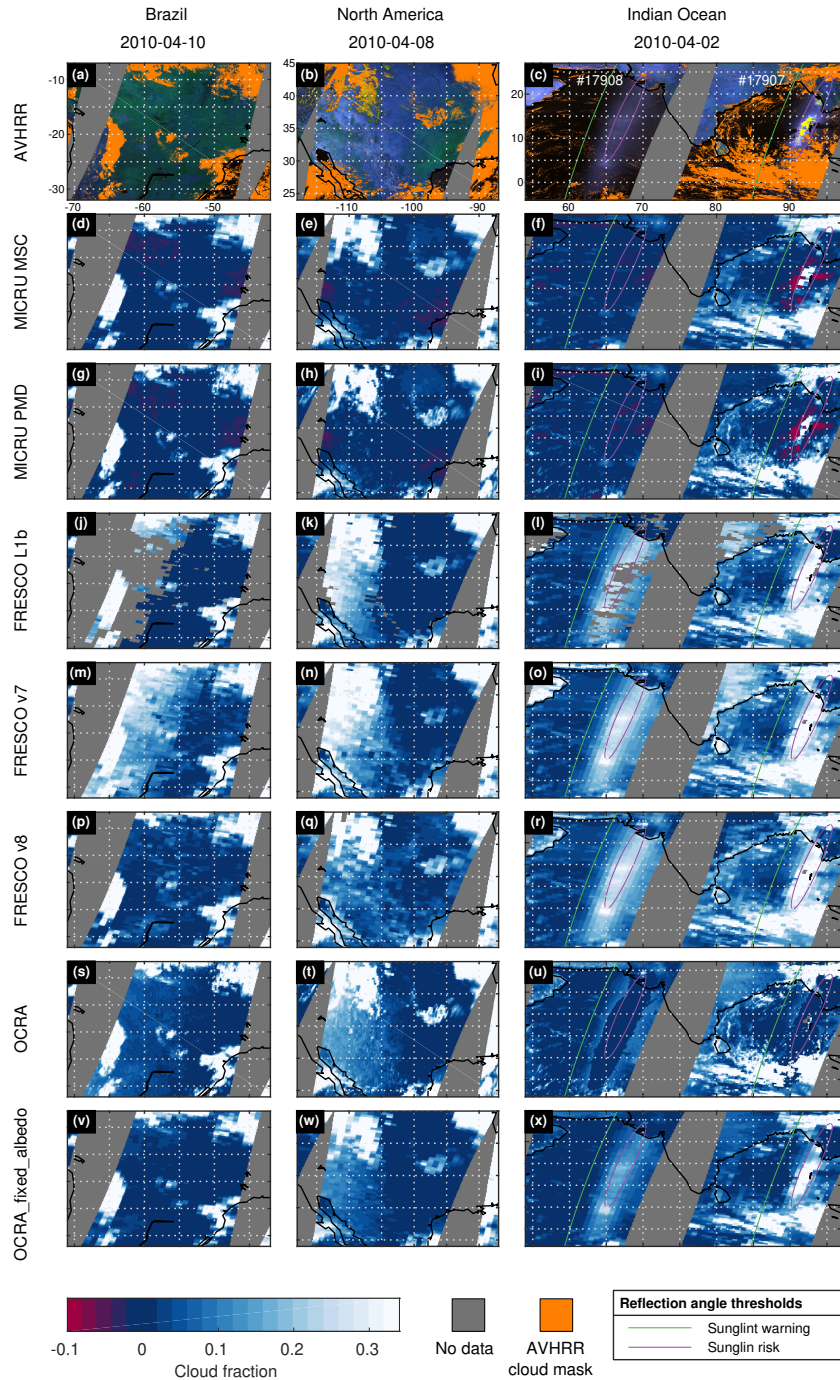
Figure 13. Detailed comparison between different cloud fraction products over cloud-free scenes over land and ocean: Brazil on 10 April 2010 (left column), North America on 8 April 2010 (second column), and the Indian Ocean on 2 April 2010. The rows display cloud information from different sensors/products (from top to bottom): AVHRR false colour RGB image indicating areas, where at least one AVHRR cloud test is positive (orange), MICRU MSC at 440 nm, MICRU PMD-PP at 460 nm, three FRESCO versions, OCRA, and OCRA_fixed_albedo. The colour bar is defined to resolve cloud fractions particularly below 0.3 and negative values. Areas without data are indicated in grey. Images in the right column contain swath data of two orbits featuring different sun glitter scenarios due to different wind conditions (see text).
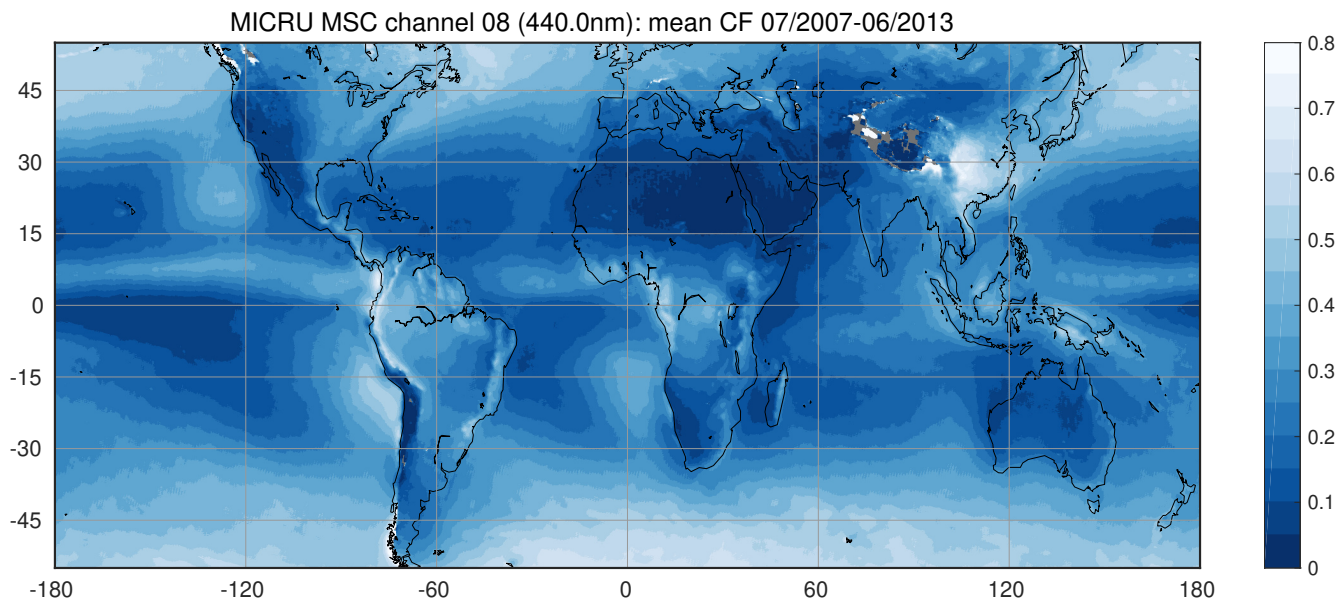
Figure 14. Six year average of MICRU MSC channel 8 cloud fraction measurements recorded between 1 July 2007 and 30 June 2013. Areas without data are plotted in gray. See Figs. F4 through F9 for comparison.

3.3 MICRU

3.3.1 Global average cloud fraction

Figure 14 shows a global map of the average MICRU cloud fraction of six consecutive years using GOME-2A measurements. Therefore, it is a snapshot of the average CF at 9:30 in morning. The averaging period starts in July 2007 and ends in June 2013. The map clearly reveals a statistically increased CF at the Intertropical Convergence Zone (ITCZ), off the west coasts of continents in the sub-tropics, and the sub-polar oceans. The comparatively high average CF over China indicates a significant bias due to aerosol scattering. Similar plots for MICRU PMD, FRESCO and OCRA are described in Appendix F.

3.3.2 MSC intercomparison

Figure 15 shows correlation density plots and bivariate fits (Cantrell, 2008) of MICRU CF for channel 2, 12, and 14 with respect to MICRU channel 8 (cf. Table 1).

The comparison between MICRU evaluations at 382 and 440 nm shows an almost perfect correlation of r^2 =0.997 in Fig. 15(a). The slope reveals a minute positive bias. Figures 15(b) and (c) reveal significantly increased scatter for comparisons with longer wavelengths, which is dominated by increased heterogeneities of the land surface reflectance because the scatter is almost independent from wavelength over ocean (not shown). It is important to note that in Figs. 15(b) and (c) the scatter

29
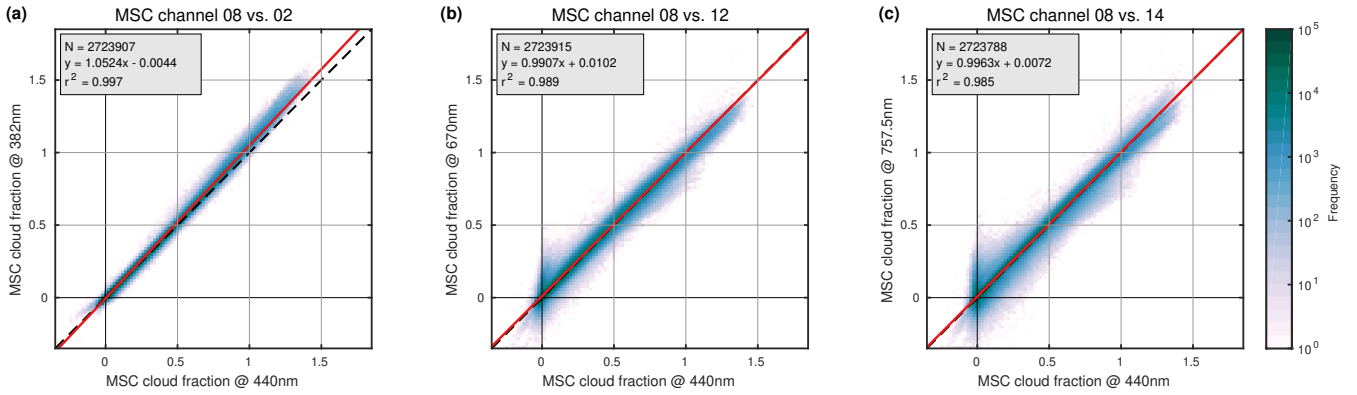
Figure 15. Comparison between MICRU MSC channel 8 at 440 nm and MSC channels (a) 2 at 382 nm, (b) 12 at 670 nm, and (c) 14 at 757.5 nm for April 2010. The plots correspond to the combinations indicated by circles in Fig. E1(a).

in y-direction for small $|c_x|$ is larger than the scatter in x-direction for small $|c_y|$. This indicates that the accuracy of CF is decreasing towards larger wavelengths.

Figure 15 furthermore indicates that the CF slope differs between MICRU channels, which is discussed in Sect. 4.1. Appendix E comprehensively compares results from MICRU channels and other cloud products.

3.3.3 MSC vs. PMD

Figure 16 shows CF comparison plots of two corresponding MSC/PMD evaluations. A spatial aliasing of $m = 0$ is chosen for the comparison at 382 nm in Fig. 16(a) and $m = 1$ at 519 nm in Fig. 16(b), respectively. According to Fig. 3, these are the optimal choices of m, which is confirmed by the circled values in Fig. E2(a) indicating a significantly higher correlation between MSC and PMD channels compared to the results neighbouring to the left and right.

Furthermore, the matrix results in Figs. E1(b) and E2(a) can be used to compare the influence of spatial versus spectral aliasing. Due to the different readout scheme (Fig. 3) both cannot be perfectly fulfilled simultaneously, either spectral or the spatial alignment between MSC and PMD can be achieved. In Fig. E1(b), the standard deviation of MSC measurements at 382 nm is slightly smaller (0.008) than for those at 424.5 nm (0.009). At 519 nm, however, the MSC values at 516.7 nm feature a smaller standard deviation (0.008) compared to those at 521.8 nm (0.009). Hence, spectral alignment seems favourable for PMD channel 1 at 382 nm whereas spatial alignment seems favourable for PMD channel 4 at 519 nm. The linear coefficients of correlation in Fig. E2(a), however, indicate, that PMD channel 1 correlates slightly better to MSC channel 5 (0.998) compared to MSC channel 2 (0.997). Hence, spatial alignment is favourable if r^2 should be optimal. For PMD channel 4, the deviation of the respective r^2 values is < 0.001 (both 0.998). It shall be noted here that Fig. E2(a) also illustrates the importance for the correct choice of m. The correlation of PMD-PP at 519 nm with itself is significantly reduced from 1 to 0.994 if the value of m deviates by ±1.
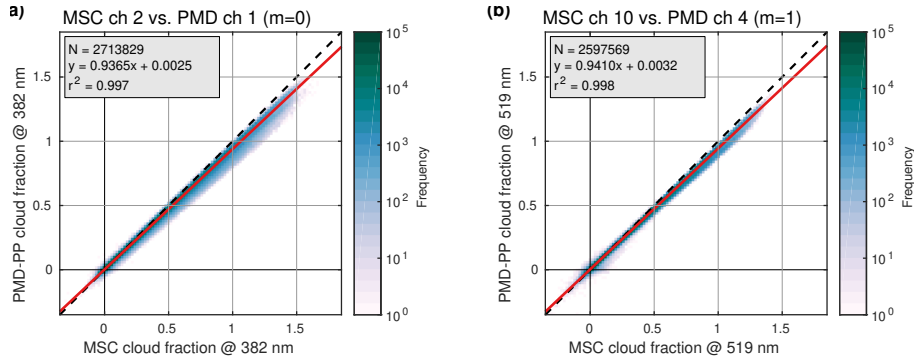
30

Figure 16. Comparison between MICRU MSC and MICRU PMD cloud fractions for April 2010: (a) at 382 nm and (b) at 519 nm. The plots correspond to the combinations indicated by circles in Fig. E2(a).
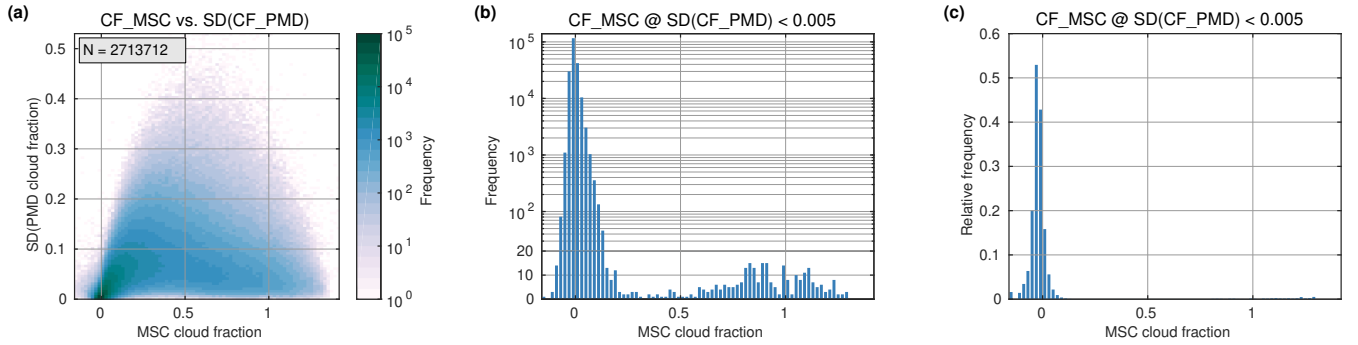

Figure 17. Standard deviation (SD) of PMD cloud fractions within one collocated MSC Pixel recorded in April 2010. PMD cloud fractions are obtained from PMD-PP channel 10 (m=1) with minimal spatial aliasing to MSC channel 10, which are both centred at 516.7 nm. (a) Density of PMD standard deviation and MSC cloud fraction; (b) histogram of MSC cloud fraction for a standard deviation of the collocated PMD measurements < 0.005, that is the lowermost row in (a); (c) relative frequency corresponding to (b). Note that the lower part of (b) is in linear, the upper part in logarithmic scale.

The coefficient of correlation between MSC channel 10 and PMD channel 4 ($m = 1$) of $r^2 = 0.998$ is optimal allowing a direct comparison and the investigation of the accuracy of small cloud fractions in the MSC product assuming that zero CF is physically only possible if all including PMD CFs are also zero. Therefore, standard deviations of PMD CFs within each MSC pixel are computed. Figure 17 shows the density of CF standard deviations versus MSC cloud fractions. The maximum
5   standard deviation is minimal for small and large CF and maximal for CF of approximately 0.5. The absolute and relative distributions of MSC measurements corresponding to a standard deviation of PMD CF <0.005 are plotted in Figs. 17(b) and (c), respectively. The width of the histogram bins is 0.02 CF. Figure 17(b) peaks at -0.01 CF and Fig. 17(c) at -0.03 CF, which can be interpreted as an estimate for the accuracy of small MICRU CF.
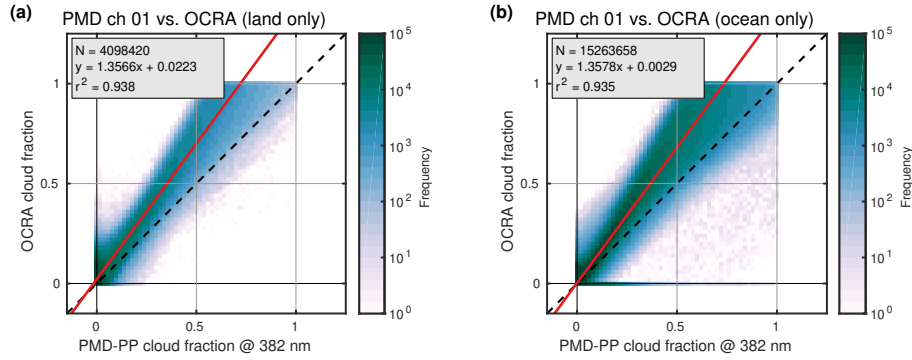
Figure 18. Comparison between MICRU PMD at 382 nm and OCRA based on CF data from April 2010: measurements over (a) land and (b) ocean. This comparison applies cropped data.

3.4 Comparison to other CF algorithms

3.4.1 MICRU vs. OCRA

Figures 13(s) and (t) in Sect. 3.2 suggest that OCRA measurements may be biased high in the western part of single cloud-free swaths over land. This observation is now investigated further based on monthly statistics. Figures 18(a) and (b) compare
5   MICRU and OCRA measurements recorded over land and ocean, respectively. Most apparently, the slope of 1.35 indicates different definitions of the upper threshold. Figure E2(c) consistently confirms that OCRA overestimates large CF compared to FRESCO and MICRU CF. This is probably due to OCRA applying a scattering cloud model to define the upper threshold whereas FRESCO and MICRU apply a reflecting cloud model. It needs to be noted that this comparison between OCRA and MICRU applies cropped data as described in Sect. 2.6, which may furthermore affect the overall slope. And indeed, the
10   comparisons between MICRU MSC and OCRA_fixed_albedo in Fig. 19 result in more moderate slopes of 0.9 and 0.86 for land and ocean, respectively. Also the linear coefficient of correlation is slightly higher compared to the uncorrected OCRA values in Fig. 18.

Secondly, it is focussed on the scatter of very small cloud fractions. Figure 18 clearly shows that OCRA CF for very small MICRU CF scatter more than MICRU CF for very small OCRA CF (cf. Fig. E1(b)). Figures 18(a) and (b) investigate this
15   feature depending on surface type land and ocean, respectively. Small OCRA CF over land scatter significantly more for small MICRU CF when compared to measurements over ocean. The same but less pronounced behaviour may be observed for OCRA_fixed_albedo in Fig. 19.

Figure 20 shows a detailed comparison between OCRA and MICRU over land where the data is sorted according to the viewing direction west, nadir, and east, respectively. Focussing again on small CF, a significant bias of 0.066 may be detected
20   when averaging over the 8 westernmost GOME-2 pixels of the swath (Fig. 20(a)), whereas the bias towards nadir and east is negligible (0.02). Furthermore, the scatter of small OCRA CF is larger towards western compared to eastern viewing directions.
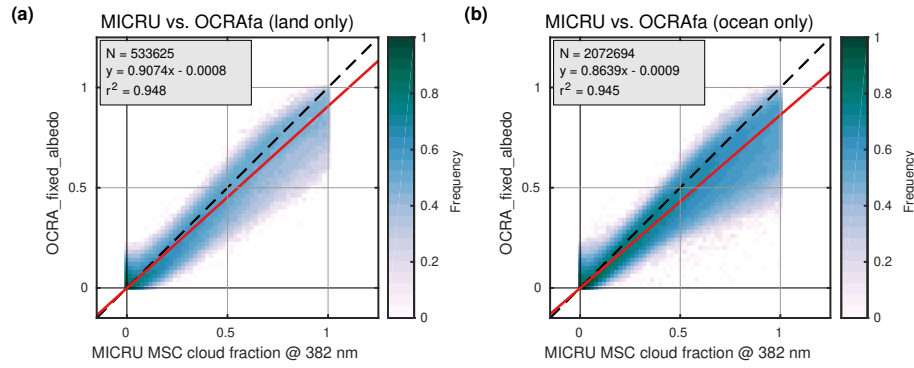
Figure 19. Comparison between MICRU MSC at 382 nm and OCRA_fixed_albedo based on CF data from April 2010: measurements over (a) land and (b) ocean. This comparison applies cropped data.
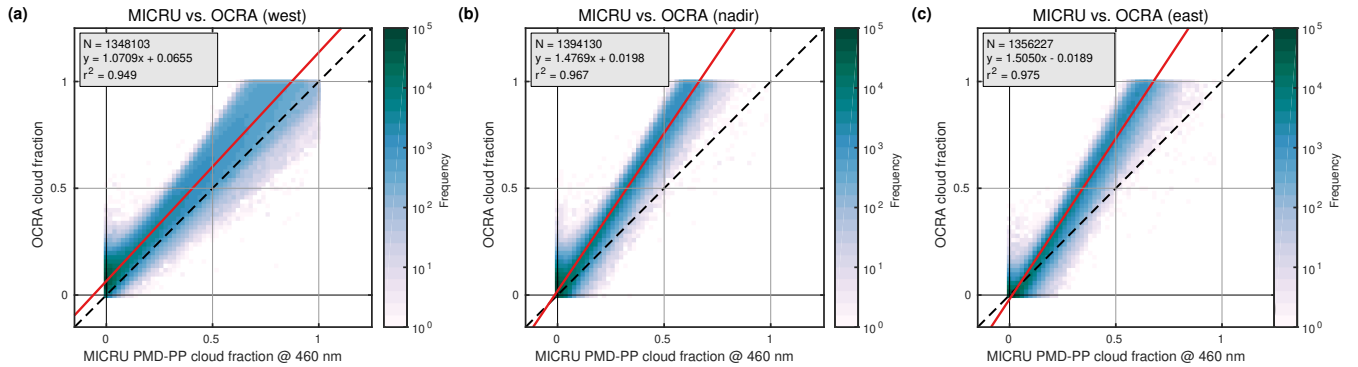

Figure 20. Same data as Fig. 18(a) but for different viewing angles: (a) west, (b) nadir, and (c) east. This comparison applies cropped data.

An additional view on the VZA-dependence of MICRU and OCRA CF is provided by Figs. 11(a)–(c) and 12(a)–(c) for land and ocean surfaces, respectively. Over land, the accumulation points of small OCRA MSC are significantly biased high for all negative VZA. The albedo correction for OCRA_fixed_albedo (Fig. 11(c)) improves the situation significantly confining the accumulation point to CF < 0.1, which is still significantly larger than the MICRU CF in Fig. 11(a). Over ocean, both
5   OCRA investigated versions reveal a significant bias from sun glitter for positive VZA in Figs. 11(b) and (c). Towards the west (negative VZA), the lower accumulation point of OCRA_fixed_albedo is more populated than MICRU.

3.4.2   MICRU vs. FRESCO

Figure 21 compiles the comparison between MICRU CF at 440 nm and three FRESCO versions depending on surface type land or ocean, respectively. Overall, all FRESCO versions reveal a significantly higher scatter of small CF compared to MICRU,
10   which is similar to the comparison to OCRA. Furthermore, the scatter over land is consistently larger compared to over ocean

due to the increased albedo effect at 757 nm applied by FRESCO. The slope of the comparisons is close to unity due to a similar definition of the upper threshold. But there are specific differences between the FRESCO versions.

The comparisons to FRESCO L1b in Fig. 21(a) and (b) feature smaller biases for small CF than FRESCO v7 and v8, which is in agreement with Fig. E1(b). The respective comparisons applying FRESCO v7 data in Fig. 21(c) and (d) reveal significantly larger scatter over both land an ocean. The bias over land is larger than 0.08, which seems to be a specific feature for FRESCO v7 as all other investigated products are less biased against each other (cf. Fig. E2(b)). The comparison over land in Fig. 21(c) includes FRESCO CF up to 0.5 for MICRU CF=0, which may be attributed to albedo effects along coasts as investigated below (Fig. 23). Figure 21(d) than shows a small quantity of unrealistic CF smaller 0.2 over ocean for MICRU CF up to 0.8. Next, the comparison between FRESCO v8 and MICRU features a bias smaller compared to v7 but still larger than L1b. The scatter is significantly improved compared to v7, but the scatter of small FRESCO CF for small MICRU CF is still much larger than vice-versa. In Fig. 21 may be furthermore observed that both FRESCO versions v7 and v8 feature CF <0. This is an improvement considering that physical measurements are affected by noise.

Similar to the comparison to OCRA, the comparisons between FRESCO and MICRU over land are now investigated depending on viewing geometry. Figure 22 consistently demonstrates that the western part of the swath are biased due to BRDF effects. Largest biases are observed towards west for FRESCO L1b and v7 (Figs. 22(a) and (d)), whereas the comparisons between FRESCO v8 and MICRU are almost independent from the viewing direction (Figs. 22(g)–(i)). It is furthermore noted that the comparisons between MICRU and FRESCO L1b for nadir and eastern viewing geometries in Figs. 22(b) and (c) reveal an almost identical scatter of small MICRU CF for small FRESCO CF and vice-versa. This feature, however, is not visible in the comparison with the two more recent FRESCO versions, for which a significant amount of small CF are systematically biased (Figs. 22(e),(f), (h), and (i)).

Figures 11(d)–(f) and 12(d)–(f) detail the VZA-dependence of the three FRESCO versions over land and ocean, respectively. Over land, the accumulation points of small CF are significantly biased high for negative VZA, especially for FRESCO L1b and v7. The distribution of FRESCO v8 CF (Fig. 11(f)), however, is almost independent of VZA. Over ocean, the differences between the FRESCO versions are small and the bias from sun glitter is again significant, which is consistent with other results.

A final comparison between MICRU and FRESCO focusses on spatial features in average CF maps. Figure 23 compares average MICRU CF maps derived at 440 nm with three corresponding average maps from FRESCO data. The maps zoom on Mexico and its Pacific coast where interferences due to the land-sea contrast can be expected. All maps are computed using the same selection of data: January, April, July, and October 2010. In order to reduce potential interferences from BRDF effects (cf. Fig. 22), only the central third (nadir) of the swath is considered where $|\theta| < 23.5°$. Significant differences between the 4 CF products are visible in the mean CF maps in the left column of Fig. 23 even though major features are similar. The difference plots in the right column quantify the differences. Comparing MICRU to FRESCO L1b in Fig. 23(c) reveals relatively high spatial gradients, especially at the coast of the peninsula. Furthermore, MICRU seems to be biased low in comparison to FRESCO L1b over the Pacific and mainland Mexico, especially in the north-east of the zoom image. The comparison to FRESCO v7 in Fig. 23(e) differs significantly. Here, FRESCO v7 is biased high throughout the image. Furthermore, FRESCO v7 CF are biased low by more than 15% along the coasts, which may be attributed to the low resolution sampling applied
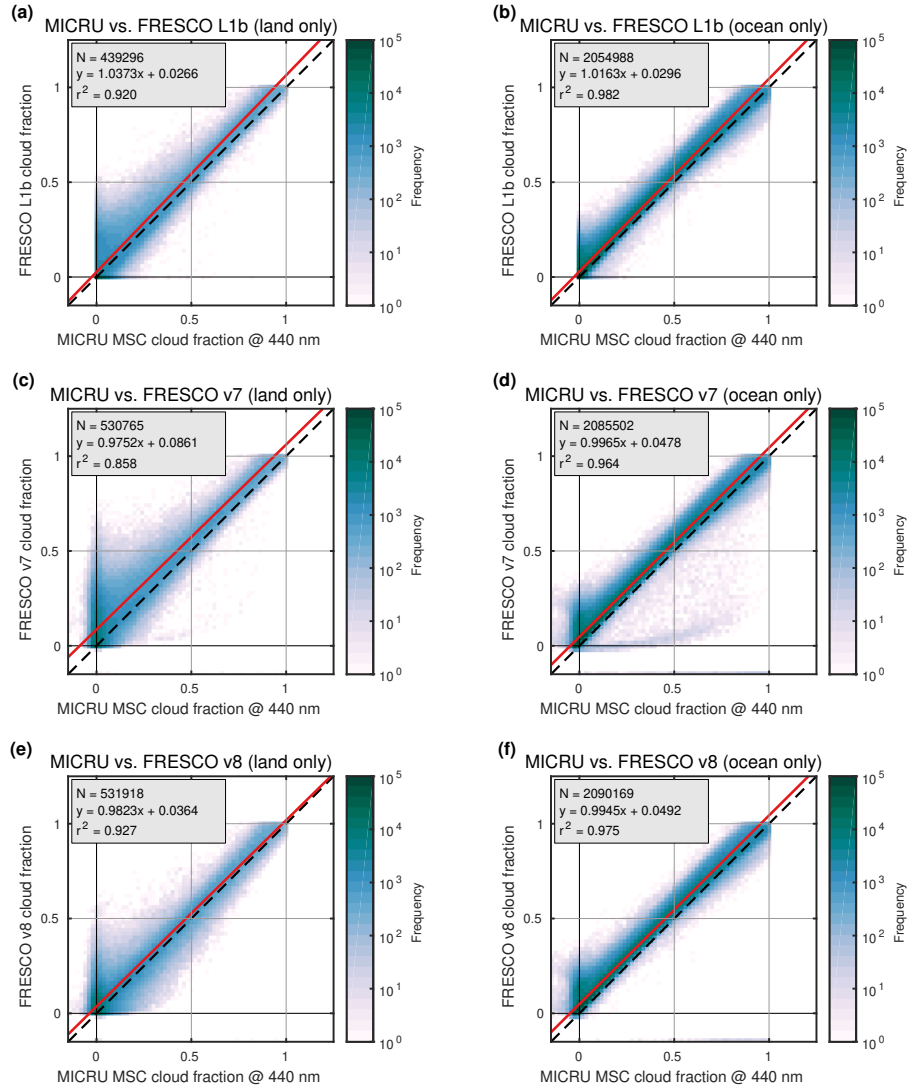
Figure 21. Comparison between MICRU MSC at 440 nm and three different FRESCO versions based on CF data from April 2010: measurements over land (left column) and ocean (right column); FRESCO L1b (top row), FRESCO v7 (middle row), and FRESCO v8 (bottom row). The comparison to FRESCO L1b applies cropped data. The comparisions in (c)–(f) only exclude CF > 1.

in the LER computation for this FRESCO version in combination with the larger albedo contrast between land and ocean in the wavelength rage applied by FRESCO. For FRESCO v8 (Fig. 23(g)), this issue is partially reduced by applying LER maps with an increased resolution along coasts. Another feature in the comparison to FRESCO v7 and v8 in Figs. 23(e) and (g) is pointed out. Both average FRESCO data are biased high with respect to MICRU in central Mexico east of Torreón
5 Municipality, where the surface albedo is significantly higher compared to the surrounding. Hence, this feature may again be due to the comparatively low spatial sampling of the background LER maps and the red wavelength range, where the influence
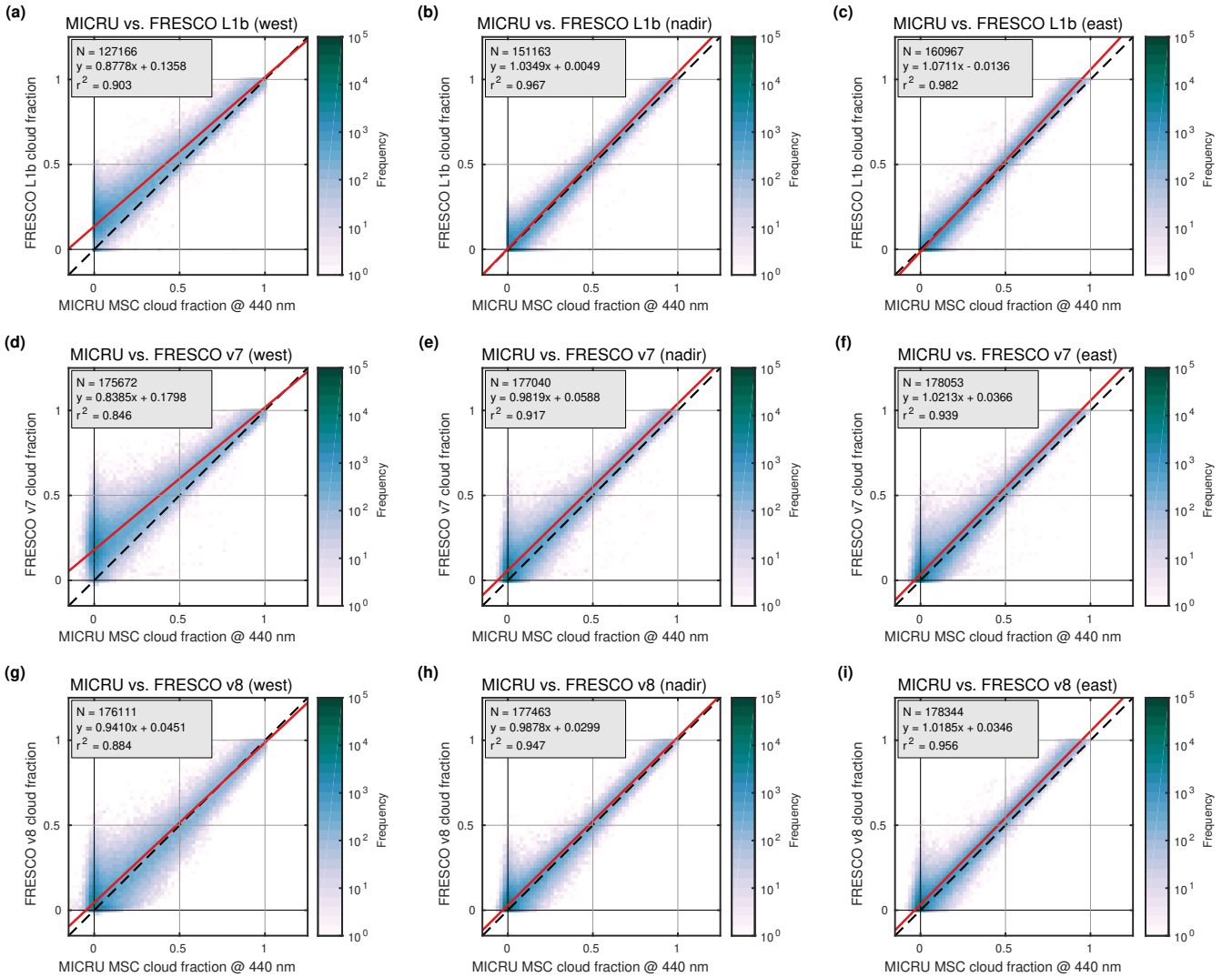
Figure 22. Viewing angle dependence of the comparison between MICRU at 440 nm and three different FRESCO versions over land. Same data as Fig.21(a), (c), and (e), respectively.

of the albedo on CF is larger compared to shorter wavelengths. In contrary, this interference is not visible in Fig. 23(c) where a MERIS background map sampled at higher spatial resolution is applied.

3.4.3 Temporal evolution and degradation

So far, the statistical evaluations are carried out on monthly data aggregates. Now, the temporal evolution of the different CF products is investigated with respect to small CF. Here, the temporal evolution is studied based on the 15th percentile of monthly CF measurements framed by the 55° parallels. Preceding test showed that 10 to 15% of GOME-2 MSC measurements
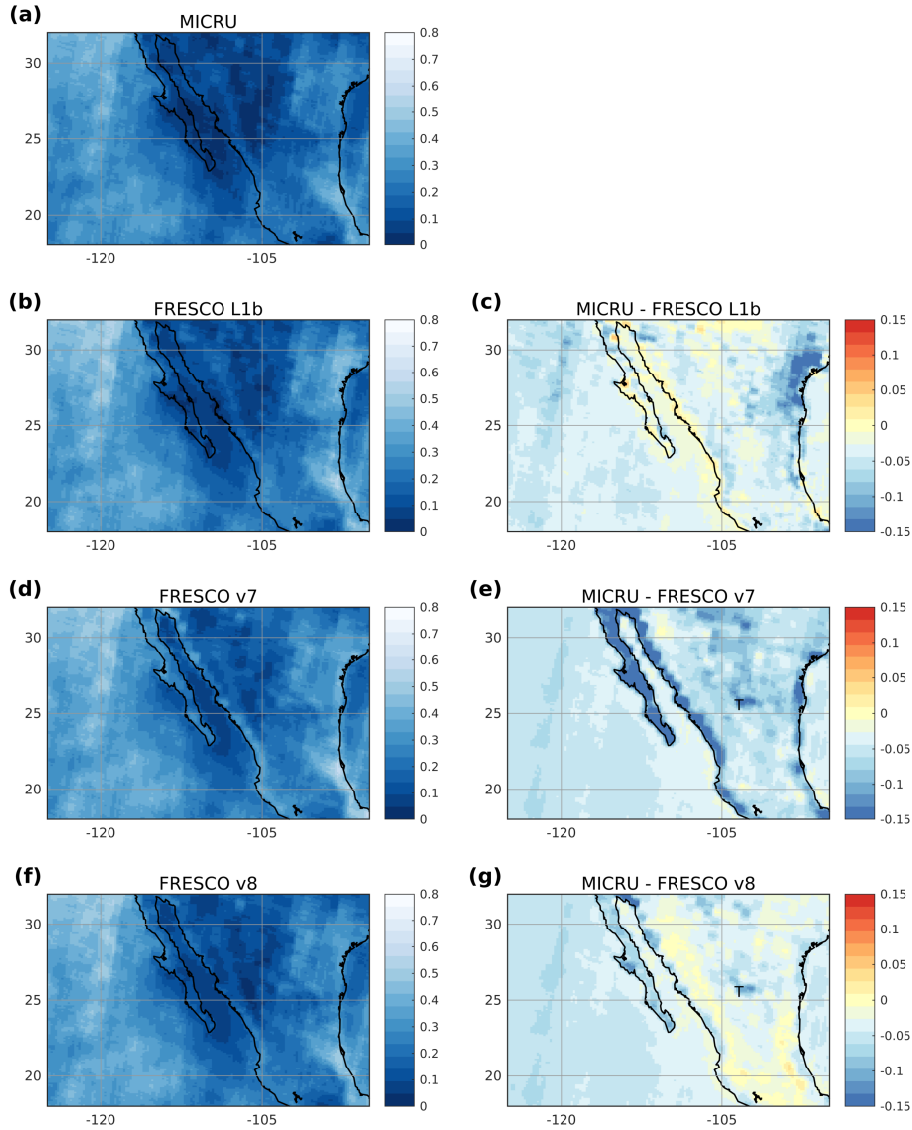
Figure 23. Comparison between average cloud fractions from different algorithms: (a) MICRU PMD channel 8 at 440 nm; (b), (d), and (f) FRESCO L1b, v7, and v8, respectively; (c), (e), and (g) respective differences between MICRU and FRESCO. Averages include all nadir measurements ($|\theta| < 23.5°$, same as in Figs. 22(b), (e), and (h), respectively) recorded in January, April, July and October 2010. The T in (e) and (g) marks the location of Torreón Municipality in Comarca Lagunera, Mexico (see text).

are effectively cloud-free. The selection of the 15th percentile showed optimal contrast for this study and avoids saturation or normalisation effects. Figure 24 compiles the temporal evolution of selected CF products and groups them in order to highlight different comparative aspects.

There are, however, no significant trends visible in the investigated time period.

Figure 24(a) compares the time series of different cloud products: MICRU MSC channel 8, the same MSC channel but applying only one year of data (dashed blue), the two MICRU PMD channels at a similar wavelength of 460, nm (cf. Table 2), OCRA MSC, OCRA_fixed_albedo, and the three FRESCO versions. First off, the two MICRU MSC versions align almost perfectly. Apparently, reducing the time interval used to derive the LT parametrisation has an almost negligible effect in this comparison. Furthermore, the statistics of MICRU MSC, MICRU PMD, and OCRA_fixed_albedo data are almost identical, with the MICRU PMD and OCRA_fixed_albedo results being positively biased of ≈ 0.005. The amplitude of bi-annual variations is of the same order for the MICRU versions and less pronounced for OCRA_fixed_albedo. In contrary to the MICRU results, OCRA and FRESCO results feature a larger amplitude of at least 0.01 and an increased annual instead of bi-annual oscillation. For all products, the overall trends are negligible compared to the annual variations.

Figure 24(b) details the CF statistics depending on VZA over land (cf. Figs. 22 and 20). The plot confirms the aforementioned results: MICRU shows negligible VZA-dependence of the 15th percentile. For FRESCO v8, the 15th percentile of nadir measurements (solid gray line) is approximately 0.01 smaller compared to measurements in the eastern and western third of the swath. The VZA-dependence in the OCRA_fixed_albedo percentiles is significantly larger compared to MICRU and FRESCO. OCRA data reveals a clear east to west trend, while FRESCO v8 features minimal CF values in the centre third of the swath. The CF in the western third of the swath of OCRA_fixed_albedo (dotted orange line) average to 0.02 while the average is close to zero in the eastern third of the swath.
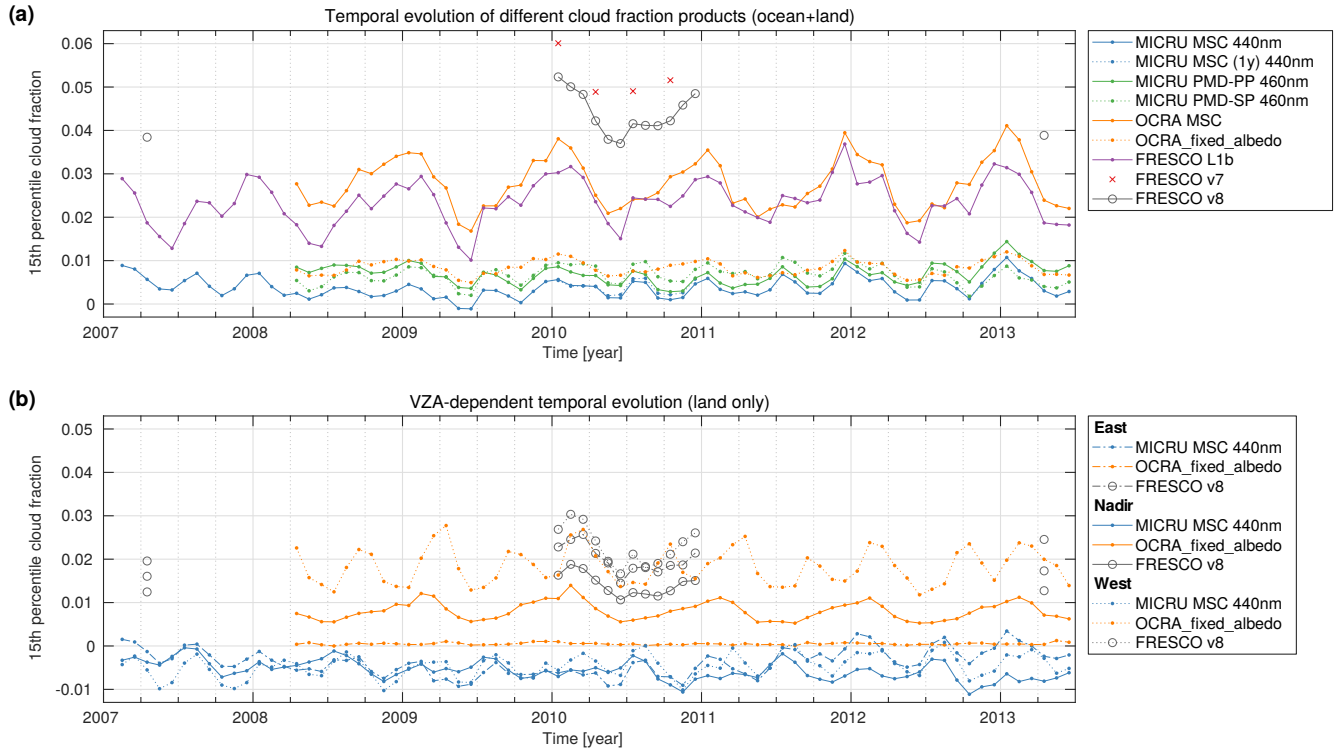
Figure 24. Temporal evolution of the 15th percentile of monthly cloud fraction distributions: (a) comparison between selected MICRU channels, 2 OCRA versions, and 3 FRESCO versions and (b) viewing angle dependency of MICRU, OCRA_fixed_albedo and FRESCO v8. Note that the offset between the blue line in (a) and the average of the blue lines in (b) is due to a different data subset, that is all vs. land only, respectively. FRESCO L1b and v7 results are omitted in (b) for the sake of clarity.

4 Discussion

4.1 MICRU

Figures 8 and 9 illustrate the $T_{\min}$ retrieval at two different sites and wavelengths. The residuals in both examples (Figs. 8(f) and 9(f)) are on average significantly smaller than the targeted 0.04 accuracy. Systematic contributions from degradation, seasonal
5   variability, VZA-dependence, and sun glitter are small. This indicates that Eq. (4) is sufficient to parametrise $T_{\min}$ for GOME-2A. Figures. 13 and 24(b) also support this conclusion. The periodic structures in the west of Fig. 8(e), which are also visible but less pronounced in Fig. 9(e), may be mostly attributed to the anisotropic reflectivity over land. Figure 11 suggests that this anisotropy may be underestimated by the operational CF products. In Fig. 8(e), there seems to be an upward trend and a shift of the apex towards east over time. Both may be attributed to the degradation of this particular MICRU channel (cf. Figs. D1(a)
10   and (d)). Furthermore, also local changes of land use, vegetation type, or precipitation climatology may lead to shifts in the lower threshold, which would be linearised by the applied $T_{\min}$-model. These additional local trends may be reproduced by the MICRU algorithm as Figs. C1(d) and (g) illustrate.

Equation (4) models the residual VZA dependence. Figure 10 shows that the VZA dependence and its temporal dependence vary between GOME-2 channels even though they are measuring in the same wavelength region. This indicates that the in-
15   strumental contribution to the residual VZA dependence is at least of the same order than possible inaccuracies of RT used to invert the surface LER. Hence, this issue can not be solved by a more accurate RT but needs to be corrected for empirically. Furthermore, degradation needs to be accounted for and it needs to be noted that the design of MICRU would allow degradation models different to Eqs. (4) and (10). For example, discrete functions and prescribed degradation are both possible to be included.

20   Considering the influence of surface BRDF effects on MICRU CF, our results support the discussion by Lorente et al. (2018) that the LER model systematically underestimates the surface reflectance in forward direction corresponding to the eastern part of the GOME-2 swath. Figures C1(f) and D1(c) show that the average apex offset is biased high. The minimum gradient of the polynomial is more frequently in the eastern part of the swath. This suggests stronger contributions from the surface BRDF in the western part of the swath in accordance with Lorente et al. (2018). Therefore, MICRU CF in Figs. 11, 12, 13, 20, and 22
25   are consistently smaller in the western part of the swath when compared to OCRA and the three FRESCO versions because OCRA and FRESCO both apply a constant surface reflectance model whereas MICRU applies an empiric VZA dependence model. This effect is almost independent from wavelength and consistent for all MICRU channels (cf. Fig. 15 and Appendix E). It needs to be noted, however, that also OCRA applies an empirical VZA correction based on global monthly means (Lutz et al., 2016).

30   Lorente et al. (2018) furthermore claim that surface effects are stronger for longer wavelengths where atmospheric scattering is weaker. Figure D1(b) may support this claim: the average curvature of the residual VZA dependency decreases with wavelength but its variance increases. This observation is consistent for all three channels and suggests that, at shorter wavelengths, the residual VZA dependency is due to a combination of instrumental and RT effects, which are similar for the ensemble of measurements. At larger wavelengths, however, the surface introduces a larger variance due to stronger spatial and season

heterogeneities. However, the wavelength dependency of the apex offset in Fig. D1(c) is ambiguous. The average apex offset peaks between 450 and 700 nm for two out of three GOME-2 channels. The variance, on the other hand, is minimal for shorter wavelengths. Therefore, retrieving CF in the UV/blue spectral range is in any case beneficial in order to reduce interferences with surface albedo and type.

5   In addition to interferences with BRDF effects, there is another drawback of retrieving CF at larger wavelengths (cf. Sect.3.3.2), which is caused by the spectral surface albedo and its heterogeneity increasing with wavelength. CF retrieved at 382 and 440 nm correlate better compared to those retrieved at the O_2-B and O_2-A band at 670 and 757.5 nm, respectively. This effect is studied more systematically in Fig. E1(b) revealing a significant increase of the standard deviation of small CF between 521.8 and 670 nm. The average CF maps Figs. F1, 14, F2, and F3 of MICRU CF at 382, 440, 670 and 757.5 nm, respectively, reveal significant systematic biases of the bright tropic deserts at 670 and 757.5 nm, notably aver Africa and Australia. At 382 and 440 nm, the MICRU results over bright desert areas are significantly smaller than all other results and may, therefore, be assumed more reliable. This assumption is confirmed by Fig. 13, where MICRU CF results over North America and East India, which are significantly brighter compared to Brazil, are not significantly biased. These maps furthermore indicate systematic CF biases from anthropogenic aerosols over East Asia and residual clouds in the tropics of South America and

15   Africa.

Another aspect of the MICRU MSC channel intercomparison are differencies at different wavelengths for high values of CF and, hence, slopes deviating from unity as, for example, shown in Fig. 15(a). CF at 382 nm are biased high with respect to those retrieved at 440 nm while the intercept at zero CF is negligible. Hence, the definition of $T_{\max}$ apparently deviates between MICRU channels, which should be independent from surface effects. Figure E2(c) comprehensively compares the slopes of all

20   MICRU channels. There is a significantly biased slope for MSC channels 1–4 retrieved at 389.7 and below. This step between MSC channels 4 and 5 may be attributed to the application of different GOME-2 bands, specifically bands 2B and 3, from which the MICRU channels are extracted (cf. Table 1). Hence, we conclude that differences between MICRU channels at high CF values are dominated by instrumental effects and calibration deficiencies of the input data. We would like to note that we observed also the CF accuracy degrading near GOME-2 band edges when fine-tuning the MSC channel definitions (Table 1).

25   The degradation depends only weakly on kernel width leading to the conclusion that this is a broadband effect. Furthermore, interferences with molecular absorption and atmospheric scattering above the clouds resulting in a wavelength dependent R may also cause a systematic slope bias. It needs to be noted, however, that the influence of the slope on the accuracy on small cloud fractions is minor.

From the systematic studies compiled in Figs. E1 and E2(c) we may conclude that MSC channels between 424.5 and

30   521.8 nm are most consistent. The varying slope in Band 2B may be influenced by instrumental effects. For cloud height retrievals using the O_2-A band, MICRU channels 4 and 7 centred at 389.68 ad 433.4 nm, respectively, may be a good option for GOME-2 as they offer reasonable spatial aliasing (Fig. 3). There is a slight priority for channel 7 when considering the mean and standard deviation of small CF in Figs. E1(a) and (b).

The comparison between MSC and PMD channel results with minimal spatial alignment in Fig. 16 shows an almost perfect

35   correlation and biases ≤ 0.4. The correlation in the UV is slightly lower compared to the visible, which may be caused by the

inferior spatial aliasing in the UV. The comparisons between MSC and PMD furthermore reveal a slope significantly smaller than 1. Figure E2(b) reveals that this is a minor feature and may be explained by calibration differences between the different GOME-2 channels. However, the slope is dominated by differences of the definition of the UT, which are not accounted for by MICRU. This behaviour has a minor effect on the accuracy of the LT.

5   The comparison between MSC and PMD measurements allows to estimate the influence of spatial (i. e. temporal) and the spectral alignment. Figure E2(a) confirms a maximum correlation for optimal m as expected. The influence of the spatial alignment parameter m is found significant and deviations by ±1 degrade the correlation from 0.998 to 0.992 for MSC at 516.7 nm. Results comparing spatial versus spectral alignment are not very clear. At least for PMD channel 4 (PMD-PP centred at 519 nm) spatial alignment seems slightly favourable over spectral alignment, which would be perfect for MSC channel 11

10   (Fig. E1(b)).

      Hence, MSC channel 10 is selected over channel 11 to be compared to PMD-PP channel 4 with $m = 1$ in order to investigate the absolute accuracy of small CF. The comparison between the standard deviation of PMD CF within one MSC pixel in Fig. 17 indicates that the systematic bias of MICRU CF is of the order of -0.03.

      Figure 24 finally shows that small MICRU CF have negligible trend over the investigated period of more than 6 years.

15   The variations of the 15th percentile are smaller than 0.01. Clearly, CF at different viewing directions are significantly more consistent for MICRU compared to OCRA and FRESCO.

4.2   OCRA

OCRA CF are compared to MICRU results based on singular orbits and exemplary monthly statistics. Both approaches consistently reveal that OCRA CF are biased high for observations towards west (Figs. 13(s), 13(t), and 20(a)). This indicates that

20   BRDF effects have a stronger influence on OCRA results for observation geometries opposing the sun and that the empirical VZA correction performed by OCRA is not sufficient. OCRA_fixed_albedo results, however, indicate that considering the cloud albedo by ROCINN significantly lowers the biases between MICRU and OCRA/ROCINN CF (Figs. 13(v-x), Fig. 19). OCRA_fixed_albedo CF values in the eastern third of the GOME-2 swath have similar statistics like MICRU (Fig. 24(b)). It needs to be noted, however, that comparisons to OCRA_fixed_albedo may only be performed at MSC resolution because the

25   required ROCINN cloud albedo values are not available in PMD resolution. Therefore, all comparisons to OCRA at PMD resolution are affected by a different cloud albedo.

      Considering the bias of small MICRU CF of -0.03, the bias of OCRA measurement in the western third of the swath can be estimated to 0.095 on average over land. These biases may be even larger depending on observation geometry and surface type (Fig. 13(t)).

30   The overall statistics in Fig. 18 indicate that small OCRA CF are on average less biased when taking into account the negative systematic bias of MICRU (Sect. 3.3.3). The accuracy of singular OCRA measurements, however, is significantly and consistently lower compared to MICRU as revealed by the larger scatter of OCRA CF for very small MICRU CF than vice versa (Figs. 18, 20, and E1(b)). Again, the application of OCRA_fixed_albedo improves the comparison in Fig. 19 significantly compared to OCRA at PMD resolution Fig. 18. The remaining excess scatter of small OCRA_fixed_albedo compared to small

MICRU CF may be explained by the spatial aliasing effect intrinsically affecting all OCRA evaluations, which combine PMD measurements from 3 PMD bands with slightly different acquisition times.

From the investigation of OCRA CF over ocean in Fig. 13(u) it can be concluded that OCRA's empirical correction algorithm is a bit too optimistic. While large contributions by sun glitter seem to be removed, the area at larger θ_r are still positively biased. At regions of very strong sun glitter (yellow areas in Fig. 13(c), OCRA seems to properly account for this effect on PMD resolution. OCRA_fixed_albedo, however is again affected by sun glitter as indicated in Fig. 13(x). It is noted that the conservative MICRU sunglint warning flag contains the affected regions and that also OCRA contains a sunglint flag.

4.3 FRESCO

Three different versions of FRESCO CF are compared to MICRU MSC results based on singular orbits, exemplary monthly statistics, and average nadir maps. The different approaches for the background maps of the FRESCO versions are clearly visible in Figs. 22 and 23. Small FRESCO CF over land are significantly biased high for western observation geometries by 0.17 and 0.21 on average for FRESCO L1b and v7, respectively. In contrary, the comparison between FRESCO v8 and MICRU is almost independent of the VZA. Therefore, we conclude that the consideration of BRDF effects in FRESCO v8 displays a significant improvement compared to preceding versions of the product.

On the other hand, however, Fig. 23 shows that interferences with the coast are minimal for FRESCO L1b whereas both newer FRESCO versions are significantly biased high at coasts and inland. This issue is slightly improved in FRESCO v8, where GOME-2 background LER data is sampled at a four times higher resolution at coasts. This specific positive bias along coasts may interfere with the processing and evaluation of tropospheric trace gas products from GOME-2 applying FRESCO because it leads to filtering a significant amount of measurements there when a CF-threshold filter is applied. Assuming a significant fraction of the worlds population resides along coasts this interference is considered significant. Less coastal measurements would be applied using FRESCO L1b, but this would come with the cost of filtering many measurements in the western part of the swath as investigated by Fig. 22.

Compared to MICRU, FRESCO results are biased high as indicated in the top right section of Fig. E1(a). The mean biases of FRESCO v7 and v8 are between 0.05 and 0.07, which is unrealistic even when considering the systematic bias of MICRU CF. In this light, FRESCO L1b CF, however, are probably less biased on average compared to MICRU.

The scatter of FRESCO CF for very small MICRU CF, however, is consistently larger for all FRESCO versions than vice versa. This may be attributed to the application of radiances close to the O_2-A band as discussed above. From the comparison of MICRU CF at different wavelengths we may furthermore conclude that the attempt by Desmons et al. (2019) to apply FRESCO at the O_2-B band may not fully mitigate significant interferences with heterogeneities of the absolute surface albedo.

In general, it appears that features in the comparison between one FRESCO version and MICRU do not appear in the comparison with the other FRESCO versions. We therefore conclude, that MICRU reveals actually less systematic features than all three considered FRESCO versions.

5 Conclusions

MICRU is a cloud fraction retrieval algorithm based on satellite radiance measurements of backscattered solar radiation. The MICRU algorithm achieves an accuracy of 0.04 in calculating small effective cloud fractions (CF) from spectroscopic satellite measurements. This is a prerequisite for accurate trace gas retrievals because clouds in most cases determine the radiative transport within each satellite measurement. The unique feature of MICRU is the application of an empirical BRDF surface model accounting for viewing angle dependencies in the cloud retrieval. The paper demonstrates that MICRU CF depend significantly less on VZA compared to other available CF products for GOME-2 and, hence, are significantly more accurate. MICRU determines the lower threshold from the measurements themselves furthermore reducing biases due to calibration and degradation issues.

As a proof-of-concept, we applied MICRU to GOME-2A data, but the algorithm is also applicable to similar spectroscopic satellite missions like SCIAMACHY, OMI, TROPOMI/S5P, and UVNS/Sentinel-5. Furthermore, MICRU can also process UV/vis imager data like AVHRR, MERIS, MODIS, or MSI/Sentinel-2 due to its scalable design.

Our results confirm that MICRU is able to accurately retrieve small CF over a wide spectral range, which renders it an optimal choice for tropospheric trace gas retrievals. These should use a cloud product based on radiance measurements of similar wavelength and spatial sampling so that the correlation between cloud and trace gas retrievals are optimised. For example, satellite instruments like Sentinel-5 have an inter-band offset of up to 30%, which deteriorates the applicability of particularly small cloud fractions retrieved in the red spectra range (e.g. FRESCO) to DOAS products like NO_2 and HCHO retrieved in the UV/blue spectral region.

In conclusion, applying radiances recorded in the UV/blue spectral range is advantageous over the red spectral range in order to reduce surface effects. Furthermore, spatial alignment effects between MSC and PMD channels may be minimised by choosing appropriate spectral convolution kernels. In order to test the applicability of MICRU to data from recent satellite missions spanning less than 6 years, it was applied on a data set reduced to one year. Results of this alternative retrieval are found to provide sufficient accuracy. Hence, MICRU may be applied on satellite missions offering less data than the GOME-2A mission with confidence.

Appendix A: Iterative surface fitting

MICRU applies an iterative threshold technique to retrieve the lower accumulation point $T_{\min}$. The method is similar to the threshold method applied by HICRU (Grzegorski et al., 2006), where $R_{\min}$ is assumed to only depend on time and viewing direction. For HICRU, this dependency could be resolved manually because the number of discrete VZAs was small, and, therefore, the lower accumulation point could be efficiently retrieved in an image processing manner. MICRU, however, assumes a more complex behaviour of $T_{\min}$ and therefore incorporates a nonlinear least-squares fit in every iteration of the lower accumulation point determination algorithm.

The basic idea behind iterative surface fitting is that the lower envelope of measurement set Ω (blue dots in exemplary Figs. 8(b) and 9(b)) is approximated by iteratively filtering measurement tuples $(\hat{t}, \hat{\theta}, \theta_s, r_g, \mathrm{LER}) \in \Omega$ fulfilling

$$\mathrm{LER} > y(\beta) + \tau \tag{A1}$$

where $y(\beta)$ is the fit result and τ is a positive threshold. β denotes the result vector of Eq. (4)

$$\beta = [a_0, a_t, a_p, a_{a0}, a_{a1}, a_s, a_g]. \tag{A2}$$

The accuracy and the convergence of the method depend on the choice of τ (Grzegorski et al., 2006), the applicability of the $T_{\min}$ model, the stability of the surface fit, and the initial values β_0. Compared to HICRU, MICRU introduces two improvements: (1) an adaptive scaling of τ reducing the number of a priori assumptions, and (2) the application of a surface fit. The surface fit incorporates parameter constraints (Table 5) and therefore the trust-region-reflective algorithm (Coleman and Li, 1994, 1996) is applied.

The initialisation of the fit defines β_0 and an initial selection vector V_0. The selection vector V_i defines the subset of measurements $\Omega_{i+1} = \Omega(V_i)$, on which the $(i+1)$-th iteration of the surface fit is applied. Table 5 provides initial values β_0 except for a_0, which is set to the median of $\mathrm{LER}(\Omega)$. V_0 is set true for all LER measurements fulfilling $\mathrm{LER} < a_0 + \sigma_0$, where σ_0 is the standard deviation of residual vector $\boldsymbol{R} = \mathrm{LER} - y(\beta_0)$. The initial threshold τ_0 is set to 0.012.

The i-th iteration consists of the following steps: Fit Eq. (4) to Ω_i with initial guess β_{i-1} yielding β_i. The residual vector is then $\boldsymbol{R} = \mathrm{LER} - y(\beta_i)$ defining the measurement set used in the next iteration through

$$\Omega_{i+1} = \{\Omega | \boldsymbol{R} < \tau \wedge \boldsymbol{R} > -3\sigma_{\boldsymbol{R}}\} \tag{A3}$$

where $\sigma_{\boldsymbol{R}}$ is again the standard deviation of $\boldsymbol{R}$. The second condition in Eq. (A3) filters outliers of the measurements distribution towards $-\infty$.

After that, the threshold for the next iteration is determined. τ_{i+1} depends on the retrieved mean LER, that is the threshold becomes larger for brighter surfaces. The adjustment is retarded to steps of $\delta\tau = 0.002$. The upper limit $\tau_{\max}$ is defined. $\tau_{\max}$ increases linearly with $\overline{y(\beta_i)}$: $\tau_{\max} = \tau_0$ for $\overline{y(\beta_i)} = 0$ and $\tau_{\max} = 0.1$ for $\overline{y(\beta_i)} = 1$. Then, τ is increased if

$$\tau_i < \tau_{\max} \Rightarrow \tau_{i+1} = \tau_i + \delta\tau$$

or decreased if

$$\tau_i > \tau_0 \wedge \tau_i > \tau_{\max} + \delta\tau \Rightarrow \tau_{i+1} = \tau_i - \delta\tau.$$

Iterations terminate if at least one of the following four conditions is true: number of iteration steps exceeds $i_{\max} = 40$, invariance of selection vector ($V_{i+1} = V_i$), invariance of result vector ($\beta_i = \beta_{i-1}$), or Ω_{i+1} includes less than 8 data points.

The result is $\beta = \beta_i$ corresponding to a remaining set Ω_i (red dots in Fig. 8(b)) defining $T_{\min}$ as a function of $\hat{t}$, $\hat{\theta}$, θ_s, and r_g in a specific geo-spatial bin. Diagnostic metrics for filtering (Sect. 2.5.3) are the number of elements in Ω_i, its ratio to the number of elements in Ω_0, and the number of iterations i.

Appendix B: $T_{\min}$ merging steps

The merging process consists of the following steps:

- Extrapolate all results to highest resolution.

- Discard result bins fulfilling

    - $i < 4$, or

    - $a_0 \leq$ -0.5 for $\varphi > 80°$S.

- Additionally, filter oceans bins where

    - $N^* \leq 120$, or

    - $N^* \leq 1000$ for $\frac{N^*}{N} < 0.02$ and $|\varphi| \leq 65°$

  is fulfilled, except in the coarsest resolution realised in binning 7.

- Additionally, filter bins over land with $N^* \leq 80$.

- Filtered maps are merged from coarse to fine resolution in order to maintain the highest resolution possible.

- Empty bins – or gaps – are extrapolated as follows:

    - For $\varphi \leq 80°$S, zonal means are copied into the gaps, if there are no data at the same latitude at all, β from one row towards North are applied

    - Remote gaps, like islands or lakes, which are more than 6° longitude and 3° latitude away from a valid bin, are filled with zonal mean values

    - Remaining gaps, e. g. at coasts, are filled by successive applying a Gaussian convolution kernel with a 1σ diameter of 3° longitude and 1° latitude.

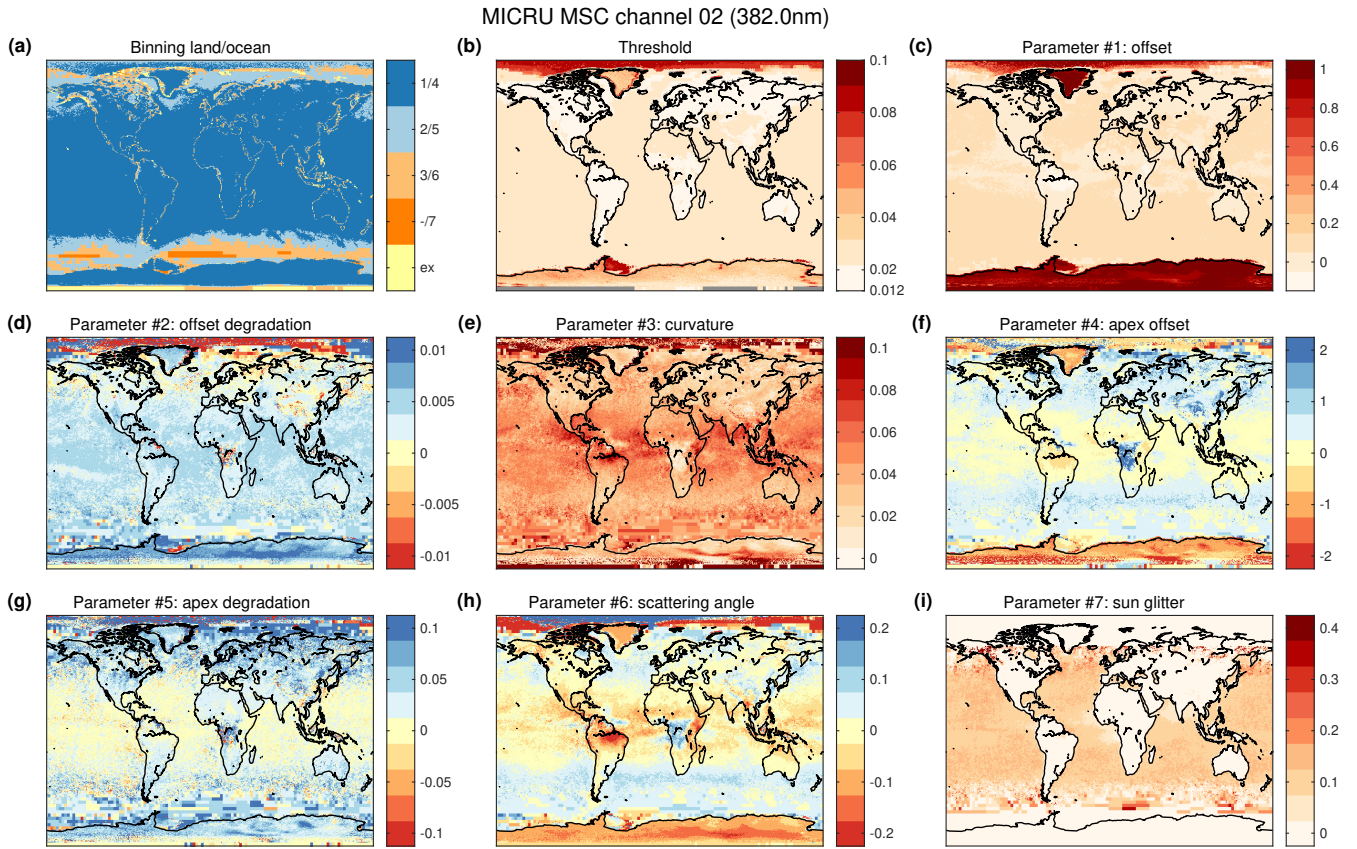- Set $a_g = 0$ for $|\varphi| > 65°$

Figure C1. Parametrisation of the lower threshold (LT) for MSC channel 02 after post-processing: (a) binning over land and ocean, (b) final threshold $T_{\min}$, (c) offset, (d) offset degradation, (e) curvature, (f) apex angle, (g) apex degradation, (h) scattering angle, (i) sun glitter. In (a), colors other than dark blue indicate regions, where the resolution is reduced or extrapolation (ex) is applied. Coast containing pixels display land results.

Appendix C: $T_{\min}$ parameter map

Figure C1 shows an exemplary stitching result for MSC channel 2. The spatial origin of the finally applied fit results is compiled in Fig. C1(a): Fit results from the highest resolution - binning 1 over land and binning 4 over ocean – are in dark blue colour. Extrapolated bins are in coloured yellow. Coastlines typically apply coarser resolutions because of the poorer statistics and the 5 90% cut-off criterion for the respective surface types. Polar oceans appear in light blue or orange colours because frequent clouds and bright sea ice significantly reduce N^*.

Figure C1 is a merged $T_{\min}$ map of all binned $T_{\min}$-results for MSC channel 2. It is the base LUT for calculating $R_{\min}$ globally. Figure C1(b) indicates, that τ increases over water and desert regions with larger LER. Figures C1(c) through (i) illustrate the geographical dependence of the fitted surface parameters. A significant latitudinal dependence and interferences 10 with the increased cloud probability at the ITCZ can be observed for all parameters. A significant land-sea contrast is visible for

47

the apex degradation in Fig. C1(g): the apex seems to shift systematically less over land. Furthermore, there is a significantly different behaviour of the apex angle and scattering angle dependence over the rain-forest regions between South America and Africa in Figs. C1(f) and (h), respectively. Both regions feature a comparatively large cloud probability, and, hence, less statistics available for the $T_{\min}$ retrieval.

5   It is noted that Figs. C1(d) and (g) reveal that both trend terms are latitudinally correlated with opposite sign. A discussion of independent terms is therefore difficult. This observation, however, confirms an overall degradation of the VZA dependence as shown in Fig. 7.

Sunglint is not constant throughout Fig (i) and, therefore, cannot be corrected for a priori. Specifically, (i) indicates lower values in the ocean west of equatorial Africa and India. Towards the poles scatter increases as sunglint contribution diminishes.

10   Over the Amazon, interestingly, there is a clear signal from sun glitter, which was not expected a-prior, illustrating the gain by fitting this parameter also over land.

Appendix D: Wavelength dependency of MICRU results

Figure D1 compiles the average wavelength dependency of the $T_{\min}$ parameters for MSC and PMD MICRU channels. Apparently, offset degradation is much more an issue for MSC and PMD-PP when compared to PMD-SP (Fig. D1(a)), which is in

15   accordance to the findings from Fig. 10. The VZA-dependence is consistently stronger in the UV compared to MICRU channels at longer wavelengths (Fig. D1(b)) but relatively smaller for PMD-PP as already discussed above. The wavelength dependence of the apex degradation in Fig. D1(d) seems to be much more complex, changing signs below 500 nm. The wavelength dependence of a_s is small compared to the overall variability in Fig. D1(e). a_g in Fig. D1(f) are increasing with wavelength suggesting Rayleigh scattering is damping the contribution from sun glitter in the UV.

20   Appendix E: Matrix comparison between MICRU, FRESCO, and OCRA

Figures E1 and E2 show a selection of comparisons between different MICRU MSC, MICRU PMD, FRESCO and OCRA cloud products for April 2010. Figures E1(a) and (b) show the mean CF and standard deviation of selected CF for the product in x-direction. The selection includes only those measurements fulfilling $|c| < 0.01$ of the product in y-direction. As a reference, results in Fig. 15, that are results where MICRU MSC channels 2, 12 and 14 are compared to MICRU MSC channel 8 evaluated

25   at 440 nm, correspond to the results in the second row as indicated by circles in Fig. E1 (a).

Focussing on the inter-MSC comparison, the upper left block in Figs. E1 and E2, one observes that the MICRU results are relatively consistent for all MICRU channels. The standard deviation in Fig. E1(b) reveals a significant jump between 521.8 and 670 nm, which was already observed in Fig. 15. Figures E2(a) and (b) show that the correlation degrades and the deviation of small CF increases with increasing spectral distance. The slope, which is dominated by $R_{\max}$, reveals a significant jump

30   between 389.7 and 425.5 nm in Fig. E2(c) coinciding with a step from MSC band 2B to band 3 (cf. Table 1).
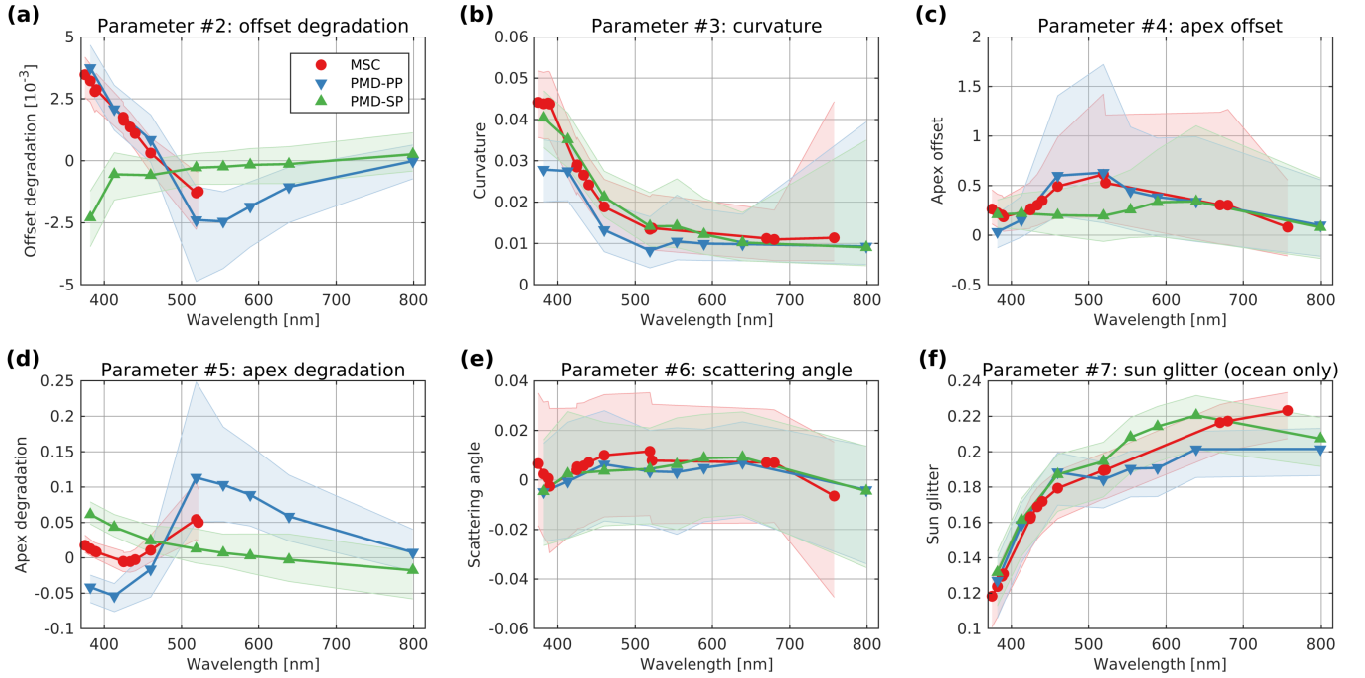
Figure D1. Wavelength dependency of T_{min} parameters: (a) offset degradation, (b) curvature, (c) apex offset, (d) apex degradation, (e) scattering angle, and (f) sun glitter. MSC channels in red, PMD channels 1–8 in blue and PMD channels 9–16 in green. Interconnected data points are median fit parameters. Transparent areas include 50% of all results with boundaries at the 25th and 75th percentiles.

MSC applying less data

In addition to the standard MSC evaluation integrating 6 years of measurements (Sect. 2.1.1), an evaluation using only one year of data is performed in order to simulate the performance of MICRU if applied to shorter data sets. We chose the year 2010 because it ranges approximately in the centre of the standard evaluation period where CF accuracy may be assumed optimal

5   (cf. Sect. 3.4.3). For this special evaluation, the parameters accounting for degradation (a_t and a_{a1} in Table 5) are constrained to 0 for all MSC channels. The results of this simulation are included in the result matrices in Figs. E1 and E2 and denoted by *1 year*.

The circles in Fig. E1(b) indicate the entries, where the new results are compared to the standard results, which are located one column to the left. All circled values are larger compared to the standard evaluation. This indicates that small cloud

10   fractions are less accurate if a shorter evaluation period is chosen. The corresponding matrix entries in Fig. E1(a) indicate that small cloud fractions retrieved at 382 nm are more deviated compared to the standard evaluation (-0.3) compared to those at longer wavelengths, where corresponding entries are negligible (denoted by ·).
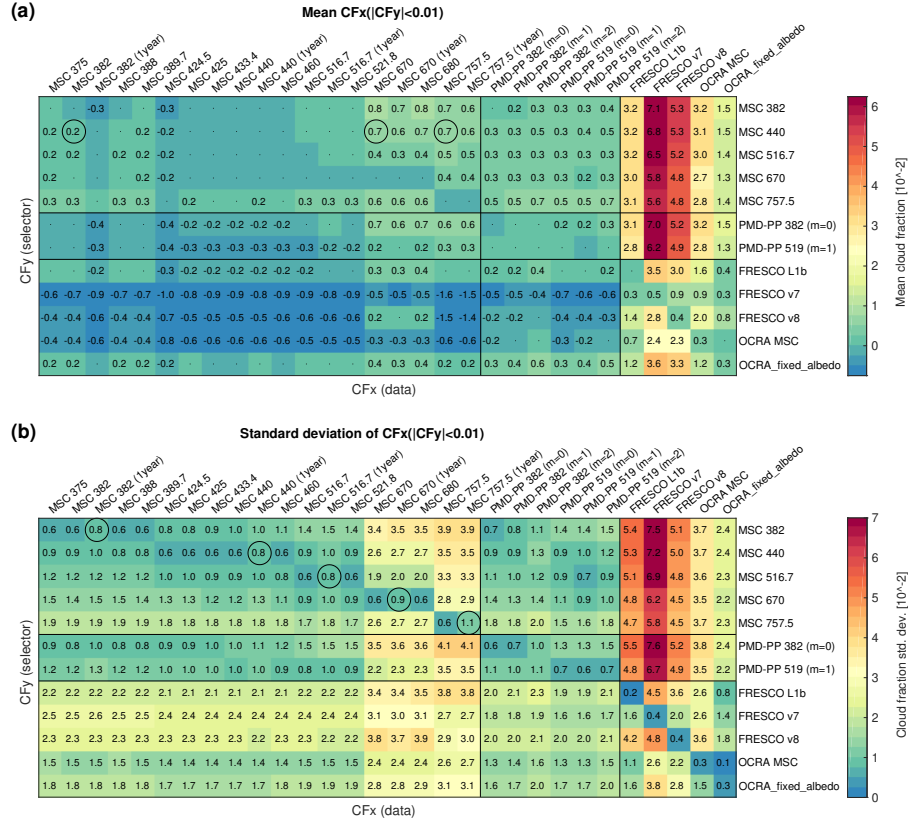
Figure E1. Tabular inter-comparison of MICRU and external cloud fraction results for April 2010: (a) Mean CF of product listed in x direction selected by corresponding product in y direction with an absolute CF<1%, (b) same as (a) but listing the standard deviation. The circled values in (a) correspond to Fig. 15. The circled values in (b) indicate values comparing data of the same MICRU channel but different evaluations periods: one year versus the standard data set applying 7+ years.
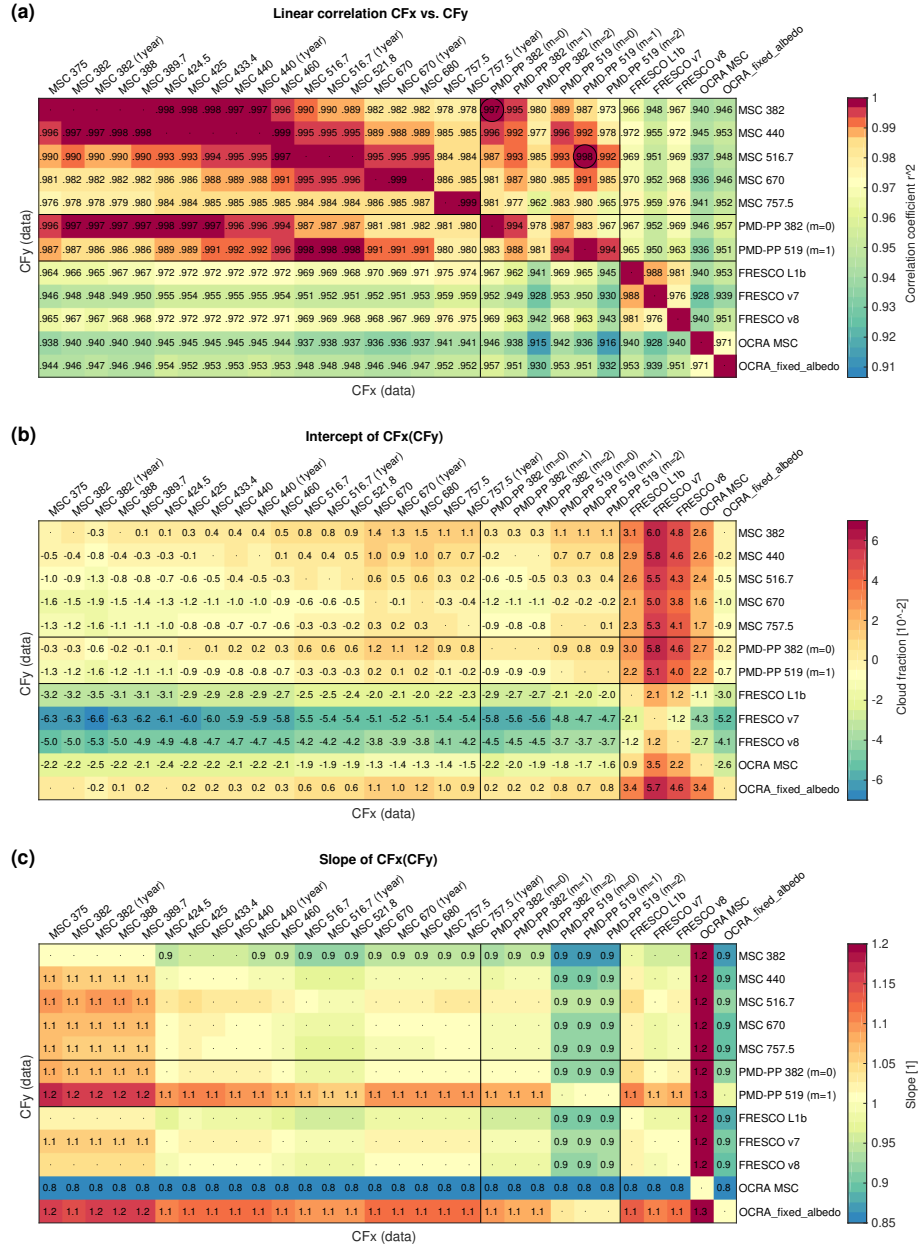
Figure E2. Continuation of Fig. E1: (a) linear coefficient of correlation r^2, (b) and (c) intercept and slope of bi-variate linear fit, respectively. Numbers of small deviations from 0 and 1, respectively, are omitted for the sake of clarity. The circled values in (a) correspond to Fig. 16.
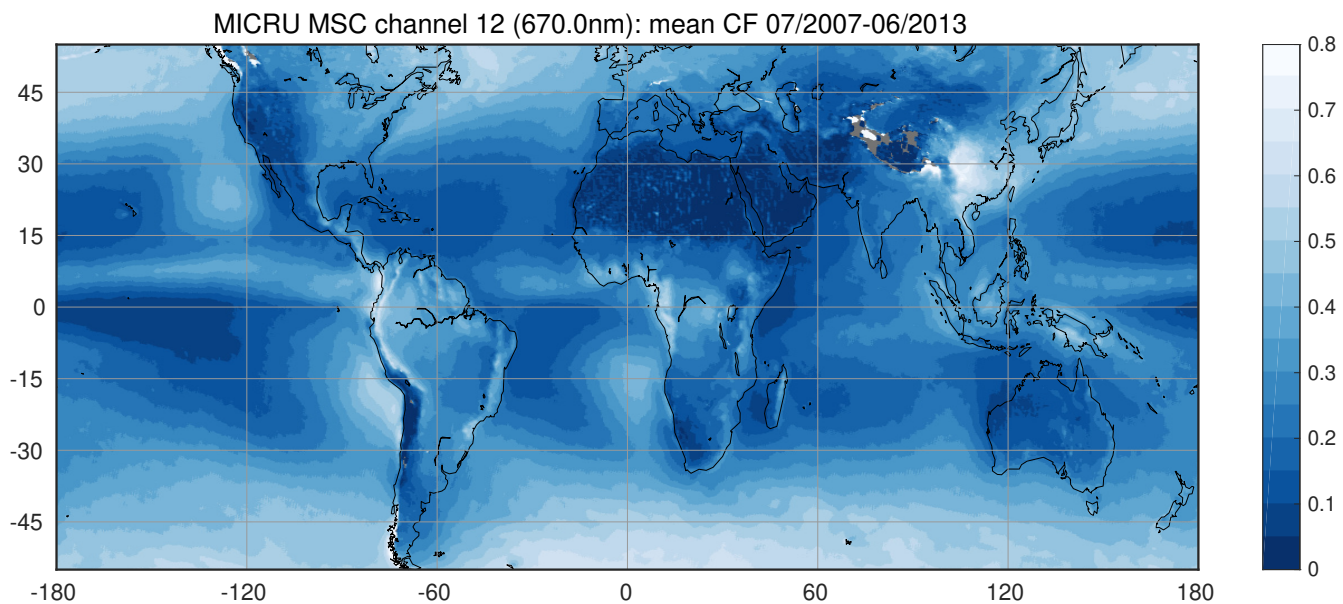
51
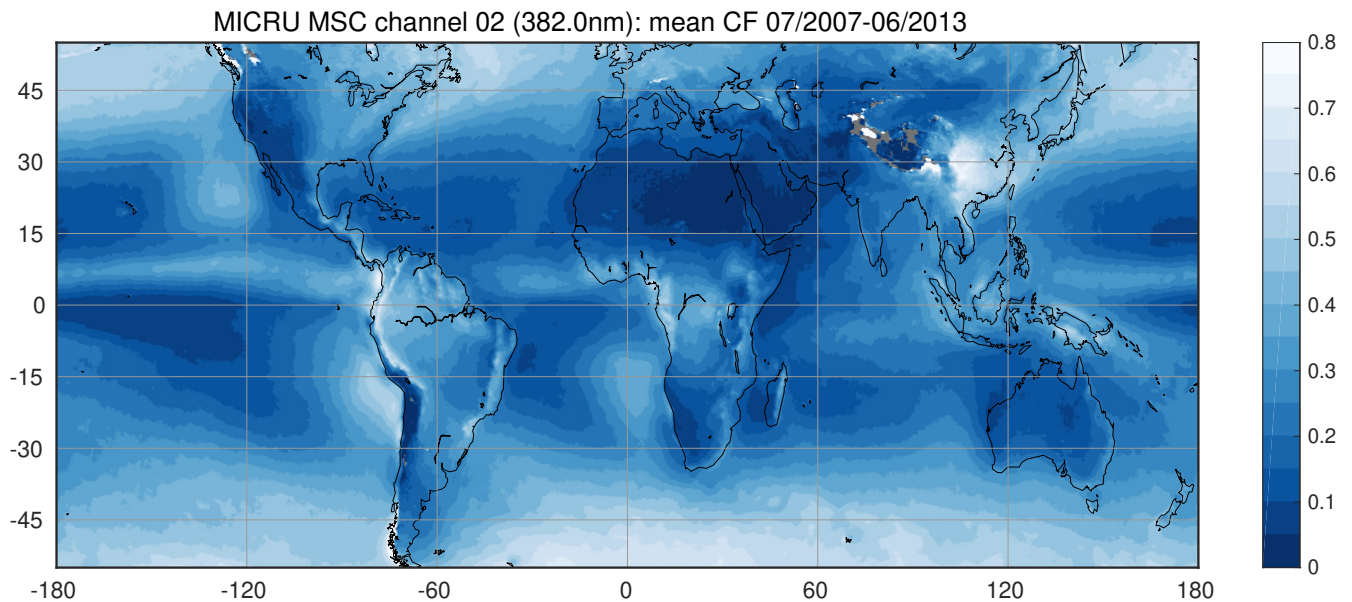
Figure F1. Six year average of MICRU MSC channel 2 cloud fraction measurements recorded between 1 July 2007 and 30 June 2013. Areas without data are plotted in gray.

Appendix F: Global average cloud fractions

This section compiles global average cloud fraction maps of MICRU MSC channels 2, 12, and 14 (Figs. F1, F2, F3), FRESCO L1b (Fig. F4), FRESCO v7 (Fig. F5), FRESCO v8 (Fig. F6), MICRU PMD channel 4 (Fig. F8), OCRA (Fig. F9), and OCRA_fixed_albedo (Fig. F7) similar to Fig. 14 in Sect. 3.3.1 applying MICRU MSC channel 8 in the main body of the paper. MICRU MSC and FRESCO L1b maps are compiled from 6 years of data collected between July 2007 and June 2013. Averages of MICRU PMD and OCRA data begin one year later. FRESCO v7 data (Fig. F5) comprises 4 months, FRESCO v8 data (Fig. F6) comprises solely year 2010.

Figure F2. Six year average of MICRU MSC channel 12 cloud fraction measurements recorded between 1 July 2007 and 30 June 2013. Areas without data are plotted in gray.
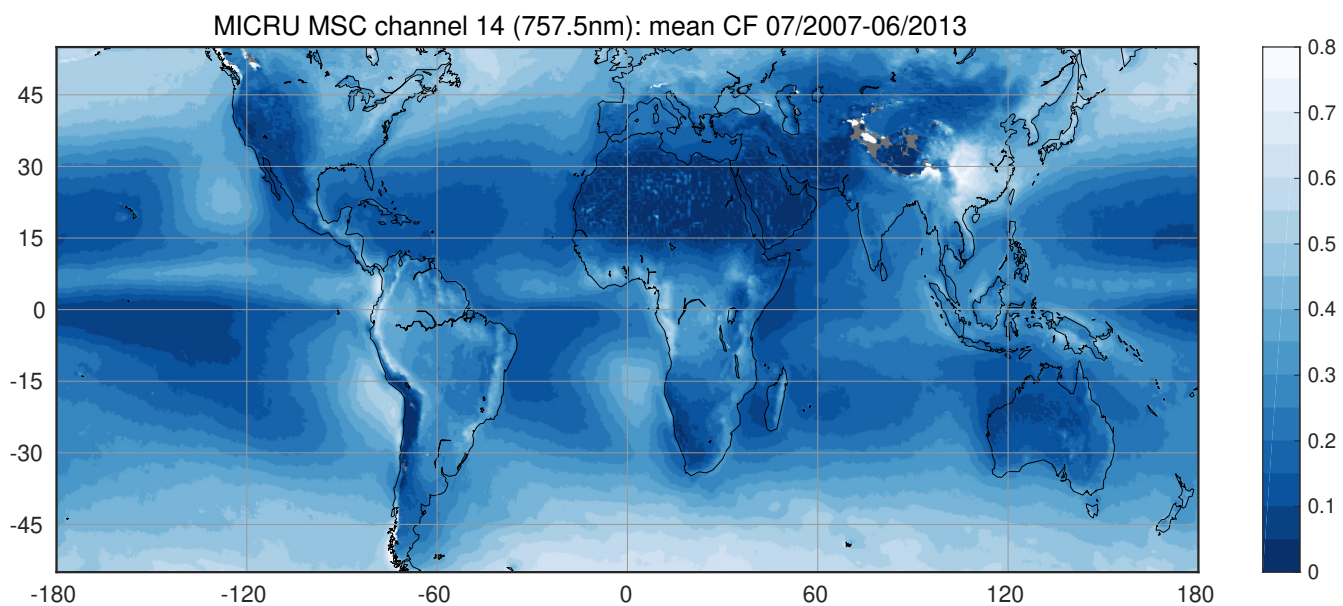
Figure F3. Six year average of MICRU MSC channel 14 cloud fraction measurements recorded between 1 July 2007 and 30 June 2013. Areas without data are plotted in gray.
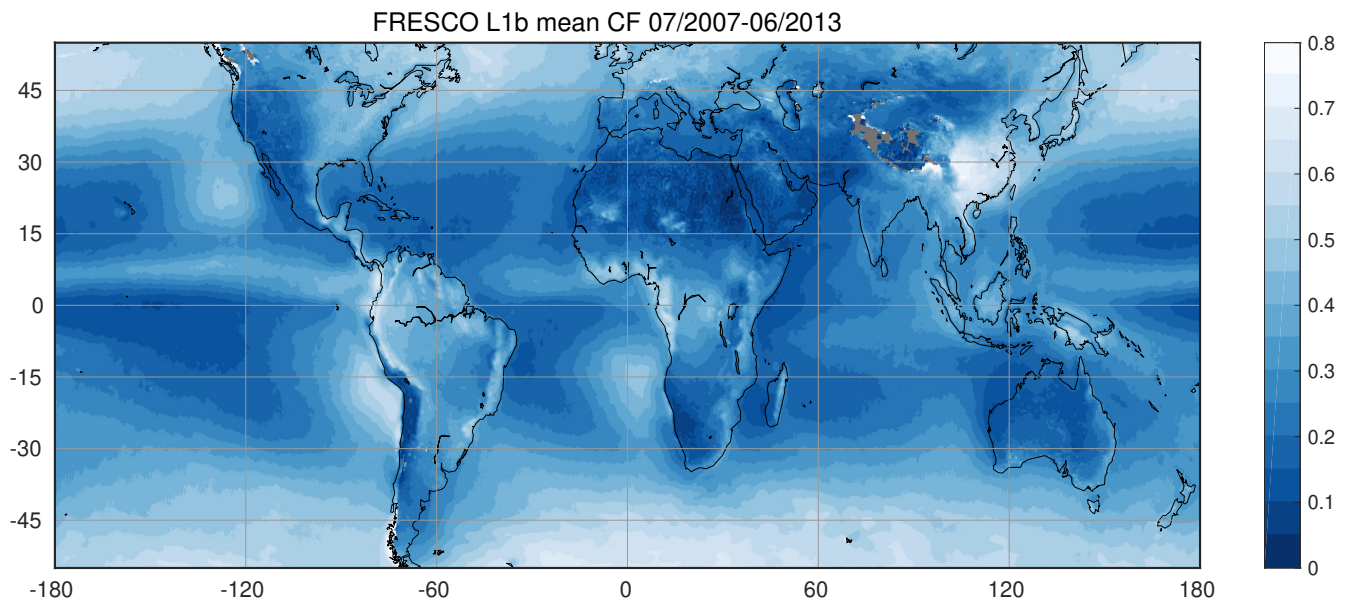
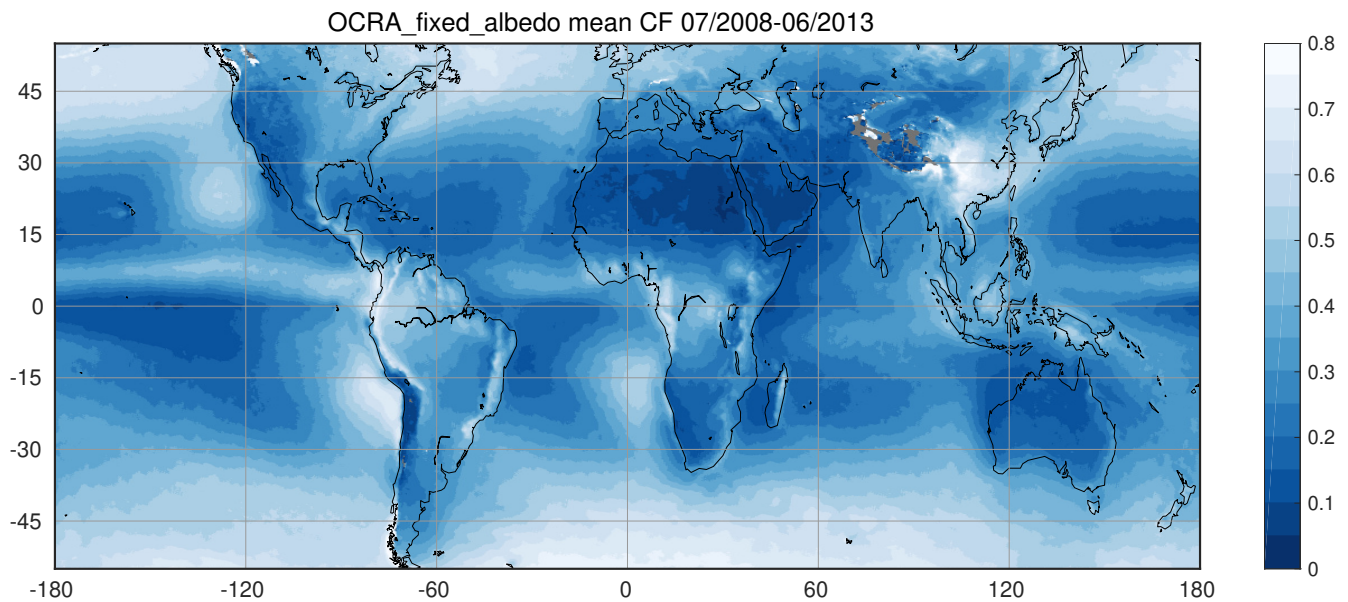**Figure F4.** Same as Fig. 14 but six year average of FRESCO L1b cloud fraction measurements recorded between 1 July 2007 and 30 June 2013. Areas without data are plotted in gray.
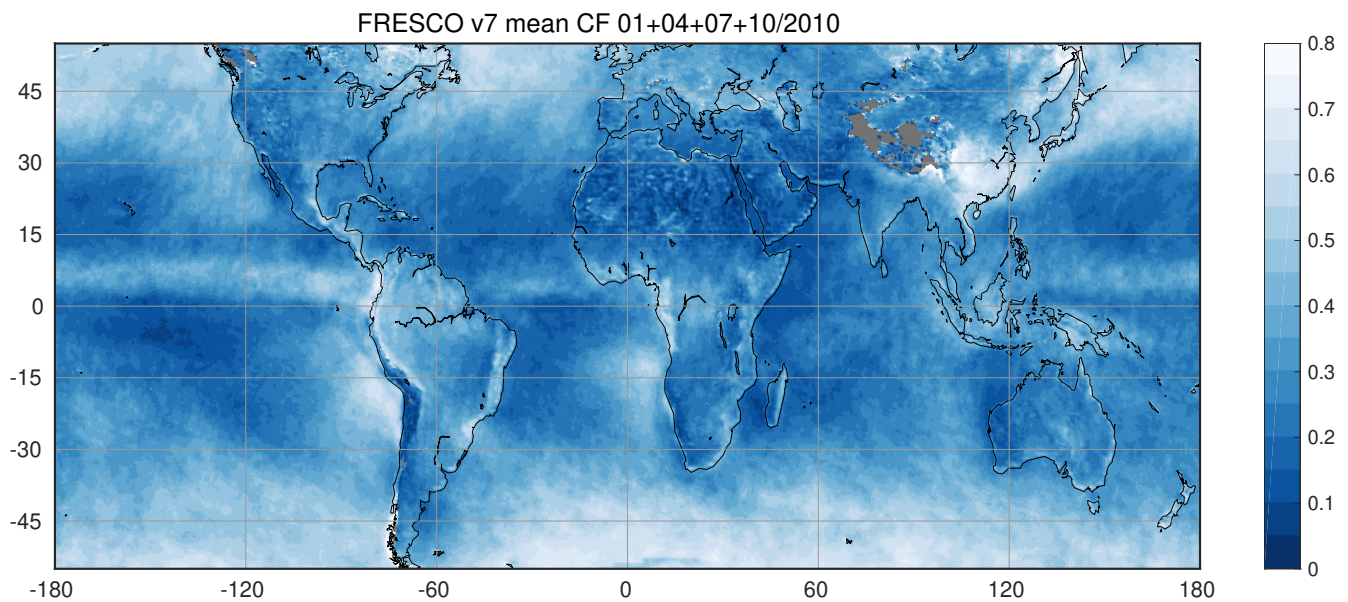
Figure F5. Same as Fig. 14 but four month average of FRESCO v7 cloud fraction measurements recorded in January, April, July, and October 2010. Areas without data are plotted in gray.
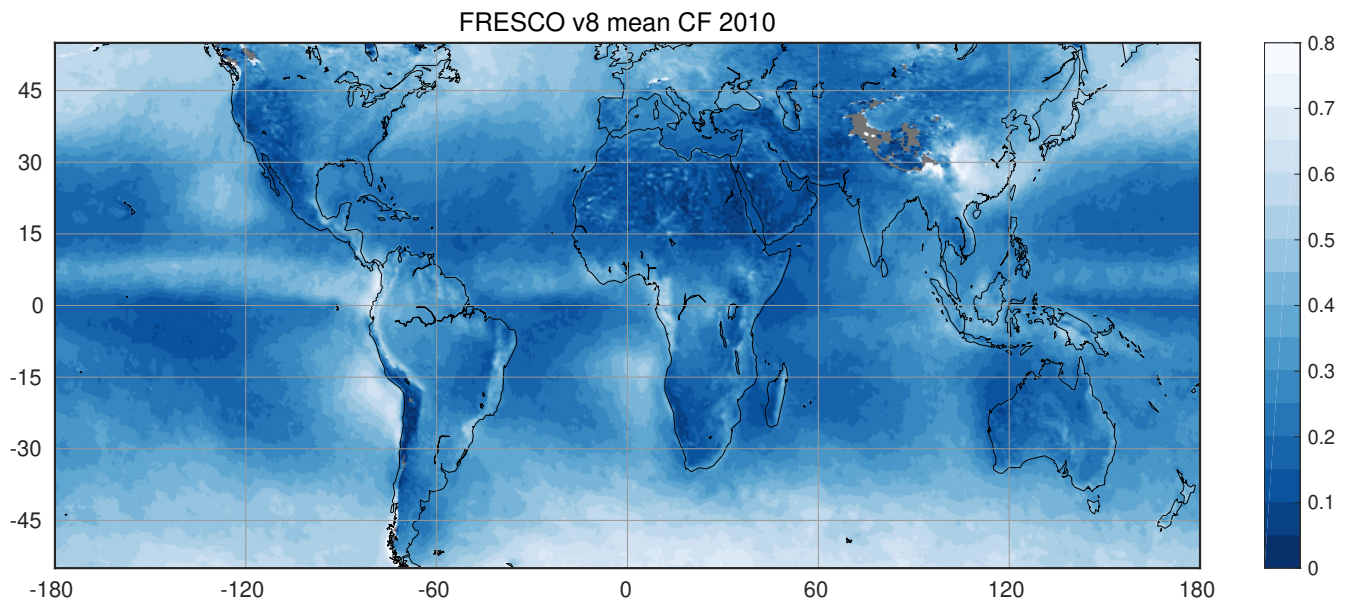
Figure F6. Same as Fig. 14 but one year average of FRESCO v8 cloud fraction measurements recorded in 2010. Areas without data are plotted in gray.

Figure F7. Same as Fig. 14 but five year average of OCRA_fixed_albedo cloud fraction measurements recorded between 1 July 2008 and 30 June 2013. Areas without data are plotted in gray.
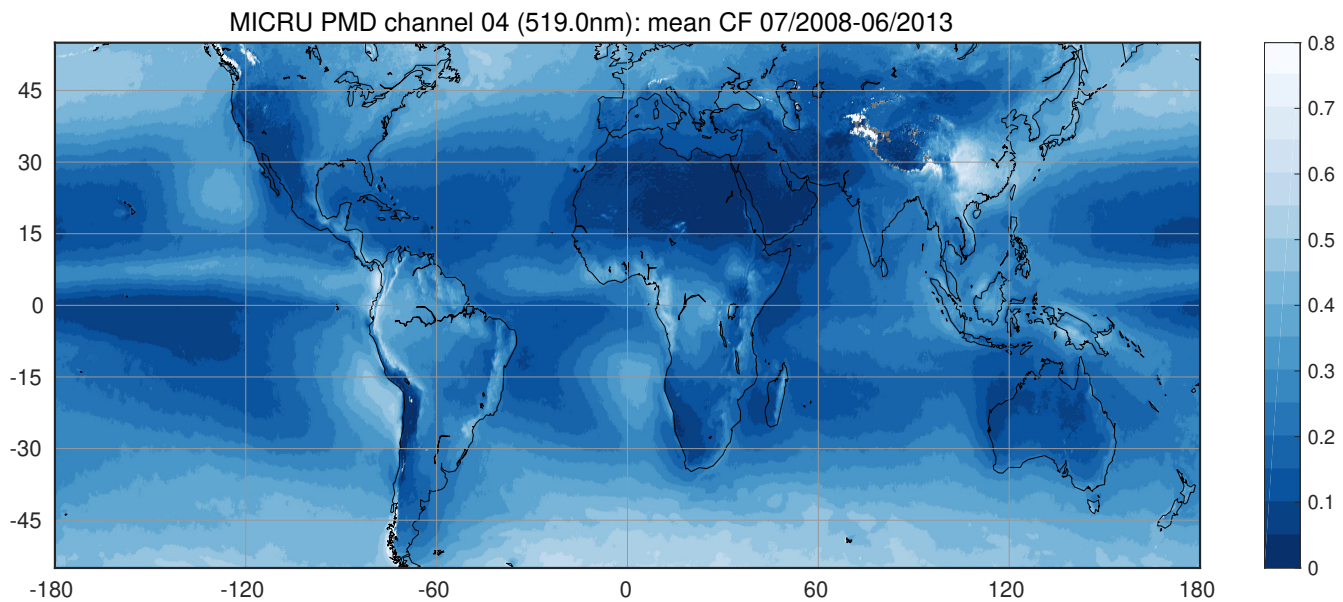
Figure F8. Same as Fig. 14 but five year average of MICRU PMD channel 04 cloud fraction measurements recorded between 1 July 2008 and 30 June 2013. Areas without data are plotted in gray.
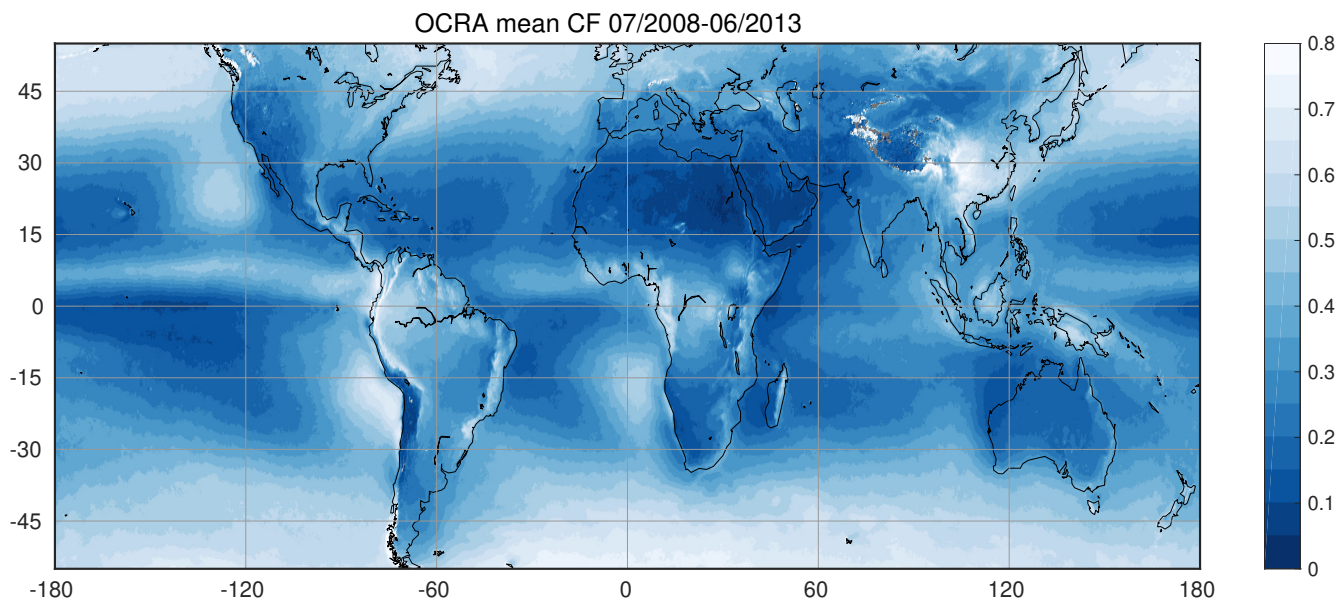

Figure F9. Same as Fig. 14 but five year average of OCRA cloud fraction measurements recorded between 1 July 2008 and 30 June 2013. Areas without data are plotted in gray.

References

Ahmad, Z., Bhartia, P. K., and Krotkov, N.: Spectral properties of backscattered UV radiation in cloudy atmospheres, J. Geophys. Res., 109, D01 201, https://doi.org/10.1029/2003JD003395, 2004.

Barkley, M. P., Kurosu, T. P., Chance, K., De Smedt, I., Van Roozendael, M., Arneth, A., Hagberg, D., and Guenther, A.: Assessing sources of uncertainty in formaldehyde air mass factors over tropical South America: Implications for top-down isoprene emission estimates, J. Geophys. Res., 117, 2156–2202, https://doi.org/10.1029/2011JD016827, 2012.

Blum, M., Rozanov, V. V., Burrows, J. P., and Bracher, A.: Coupled ocean-atmosphere radiative transfer model in the framework of software package SCIATRAN: Selected comparisons to model and satellite data, Adv. Space Res., 49, 1728–1742, https://doi.org/10.1016/j.asr.2012.02.012, 2012.

Boersma, K. F., Eskes, H. J., and Brinksma, E. J.: Error analysis for tropospheric NO 2 retrieval from space, J. Geophys. Res., 109, D04 311, https://doi.org/10.1029/2003JD003962, 2004.

Bovensmann, H., Burrows, J. P., Buchwitz, M., Frerick, J., Noël, S., Rozanov, V. V., Chance, K. V., and Goede, A. P. H.: SCIAMACHY: mission objectives and measurement modes, J. Atmos. Sci., 56, 127–150, https://doi.org/10.1175/1520-0469(1999)056<0127:SMOAMM>2.0.CO;2, 1999.

Burrows, J. P., Weber, M., Buchwitz, M., Rozanov, V., Ladstätter-Weißenmayer, A., Richter, A., DeBeek, R., Hoogen, R., Bramstedt, K., Eichmann, K.-U., Eisinger, M., and Perner, D.: The Global Ozone Monitoring Experiment (GOME): Mission concept and first scientific results, J. Atmos. Sci., 56, 151–175, https://doi.org/10.1175/1520-0469(1999)056<0151:TGOMEG>2.0.CO;2, 1999.

Callies, J., Corpaccioli, E., Eisinger, M., Hahne, A., and Lefebvre, A.: GOME-2 – MetOp's Second-Generation Sensor for Operational Ozone Monitoring, ESA Bulletin, 102, 28–36, 2000.

Cantrell, C. A.: Technical Note: Review of methods for linear least-squares fitting of data and application to atmospheric chemistry problems, Atmos. Chem. Phys., 8, 5477–5487, https://doi.org/10.5194/acp-8-5477-2008, 2008.

Cavalieri, D. J., Parkinson, C. L., Gloersen, P., and Zwally, H. J.: Sea Ice Concentrations from Nimbus-7 SMMR and DMSP SSM/I-SSMIS Passive Microwave Data, Version 1, NSIDC-0051, 2007–2013, NASA National Snow and Ice Data Center Distributed Active Archive Center, Boulder, Colorado USA, https://doi.org/10.5067/8GQ8LZQVL0VL, last access: 25 Mai 2018, 1996.

Coleman, T. F. and Li, Y.: On the Convergence of Reflective Newton Methods for Large-Scale Nonlinear Minimization Subject to Bounds, Math. Program., 67, 189–224, https://doi.org/10.1007/BF01582221, 1994.

Coleman, T. F. and Li, Y.: An Interior, Trust Region Approach for Nonlinear Minimization Subject to Bounds, SIAM J. Optimiz., 6, 418–445, https://doi.org/10.1137/0806023, 1996.

Cox, C. and Munk, W.: Measurement Of The Roughness Of The Sea Surface From Photographs Of The Sun's Glitter, J. Opt. Soc. Am., 44, 838–850, 1954a.

Cox, C. and Munk, W. H.: Statistics of the sea surface derived from sun glitter, J. Mar. Res., 13, 198–227, https://doi.org/10.5194/amt-9-3607-2016, 1954b.

Cracknell, A.: The Advanced Very High Resolution Radiometer, Taylor and Francis, London, ISBN 9780748402090, 1997.

de Graaf, M., Sihler, H., Tilstra, L. G., and Stammes, P.: How big is an OMI pixel?, Atmos. Meas. Tech., 9, 3607–3618, https://doi.org/10.5194/amt-9-3607-2016, 2016.

De Smedt, I., Müller, J., Stavrakou, T., van der A, R., Eskes, H., and Van Roozendael, M.: Twelve years of global observations of formaldehyde in the troposphere using GOME and SCIAMACHY sensors, Atmos. Chem. Phys., 8, 4947–4963, https://doi.org/10.5194/acp-8-4947-2008, 2008.

Dee, D. P., Uppala, S. M., Simmons, A. J., Berrisford, P., Poli, P., Kobayashi, S., Andrae, U., Balmaseda, M. A., Balsamo, G., Bauer, P., Bechtold, P., Beljaars, A. C. M., van de Berg, L., Bidlot, J., Bormann, N., Delsol, C., Dragani, R., Fuentes, M., Geer, A. J., Haimberger, L., Healy, S. B., Hersbach, H., Hólm, E. V., Isaksen, L., Kållberg, P., Köhler, M., Matricardi, M., McNally, A. P., Monge-Sanz, B. M., Morcrette, J.-J., Park, B.-K., Peubey, C., de Rosnay, P., Tavolato, C., Thépaut, J.-N., and Vitart, F.: The ERA-Interim reanalysis: configuration and performance of the data assimilation system, Q. J. Roy. Meteor. Soc., 137, 553–597, https://doi.org/10.1002/qj.828, 2011.

Desmons, M., Wang, P., Stammes, P., and Tilstra, L. G.: FRESCO-B: a fast cloud retrieval algorithm using oxygen B-band measurements from GOME-2, Atmos. Meas. Tech., 12, 2485–2498, https://doi.org/10.5194/amt-12-2485-2019, 2019.

Deutschmann, T., Beirle, S., Frieß, U., Grzegorski, M., Kern, C., Kritten, L., Platt, U., Prados-Román, C., Pukite, J., Wagner, T., Werner, B., and Pfeilsticker, K.: The Monte Carlo atmospheric radiative transfer model McArtim: Introduction and validation of Jacobians and 3D features, J. Quant. Spectrosc. Ra., 112, 1119–1137, https://doi.org/10.1016/j.jqsrt.2010.12.009, 2011.

Ebuchi, N. and Kizu, S.: Probability Distribution of Surface Wave Slope Derived Using Sun Glitter Images from Geostationary Meteorological Satellite and Surface Vector Winds from Scatterometers, J. Oceanogr., 58, 477–486, https://doi.org/10.1023/A:1021213331788, 2002.

EUMETSAT: AVHRR Level 1b Product Guide, Internet, https://www.eumetsat.int/website/wcm/idc/idcplg?IdcService=GET_FILE&dDocName=PDF_AVHRR_L1B_PRODUCT_GUIDE&RevisionSelectionMethod=LatestReleased&Rendition=Web, last access: 19 June 2019, 2011.

EUMETSAT: GOME-2/Metop-A instrument, PPF and auxiliary-data change history, Internet, http://oiswww.eumetsat.org/epsreports/html/history/MetopAGOME2PPFhist.pdf, last access: 22 May 2019, 2014.

EUMETSAT: GOME-2 Factsheet, Internet, http://www.eumetsat.int/, last access: January 2019, 2015.

Fasnacht, Z., Vasilkov, A., Haffner, D., Qin, W., Joiner, J., Krotkov, N., Sayer, S. M., and Spurr, R.: A geometry-dependent surface Lambertian-equivalent reflectivity product for UV–Vis retrievals – Part 2: Evaluation over open ocean, Atmos. Meas. Tech, 12, 6749–6769, https://doi.org/10.5194/amt-12-6749-201, 2019.

Fournier, N., Stammes, P., de Graaf, M., van der A, R., Piters, A., Grzegorski, M., and Kokhanovsky, A.: Improving cloud information over deserts from SCIAMACHY Oxygen A-band measurements, Atmos. Chem. Phys., 6, 163–172, https://doi.org/10.5194/acp-6-163-2006, 2006.

Grainger, J. F. and Ring, J.: Anomalous Fraunhofer Line Profiles, Nature, 193, 762, https://doi.org/10.1038/193762a0, 1962.

Grzegorski, M.: Cloud retrieval from UV/VIS satellite instruments (SCIAMACHY and GOME), Dissertation, University of Heidelberg, https://doi.org/10.11588/heidok.00010423, 2009.

Grzegorski, M., Wenig, M., Platt, U., Stammes, P., Fournier, N., and Wagner, T.: The Heidelberg iterative cloud retrieval utilities (HICRU) and its application to GOME data, Atmos. Chem. Phys., 6, 4461–4476, https://doi.org/10.5194/acp-6-4461-2006, 2006.

Hall, D. K. and Riggs, G. A.: MODIS/Terra Snow Cover 8-Day L3 Global 0.05Deg CMG, Version 6, 2007–2013, NASA National Snow and Ice Data Center Distributed Active Archive Center, Boulder, Colorado USA, https://doi.org/10.5067/MODIS/MOD10C2.006, last access: 1 June 2017, 2016.

Harmel, T. and Chami, M.: Estimation of the sunglint radiance field from optical satellite imagery over open ocean: multidirectional approach and polarization aspects, J. Geophys. Res.-Oceans, 118, 76–90, https://doi.org/10.1029/2012JC008221, 2013.

Herman, J. R. and Celarier, E. A.: Earth surface reflectivity climatology at 340–380 nm from TOMS data, J. Geophys. Res., 102, 28 003–28 012, https://doi.org/10.1029/97JD02074, 1997.

IFE-Bremen: User's Guide for the Software Package SCIATRAN (Radiative Transfer Model and Retrieval Algorithm) – Version 3.8, Internet, Institute of Remote Sensing (IFE), University of Bremen, Germany, http://www.iup.uni-bremen.de/sciatran/free_downloads/users_guide_sciatran.pdf, last access: 14 February 2019, 2018.

Justice, C., Vermote, E., Townshend, J., Defries, R., Roy, D., Hall, D., Salomonson, V., Privette, J., Riggs, G., Strahler, A., Lucht, W., Myneni, R., Knyazikhin, Y., Running, S., Nemani, R., Wan, Z., Huete, A., van Leeuwen, W., Wolfe, R., Giglio, L., Muller, J., Lewis, P., and Barnsley, M.: The Moderate Resolution Imaging Spectroradiometer (MODIS): land remote sensing for global change research, IEEE Trans. Geosci. Remote Sens., 36, 1228–1249, https://doi.org/10.1109/36.701075, 1998.

Kleipool, Q. L., Dobber, M. R., de Haan, J. F., and Levelt, P. F.: Earth surface reflectance climatology from 3 years of OMI data, J. Geophys. Res.-Atmos., 113, D18 308, https://doi.org/10.1029/2008JD010290, 2008.

KNMI: OMI Instrument Characteristics, Internet, https://projects.knmi.nl/omi/research/instrument/characteristics.php, last access: 4 February 2015, 2019.

Koelemeijer, R. B. A., Stammes, P., Hovenier, J. W., and de Haan, J. F.: A fast method for retrieval of cloud parameters using oxygen A-band measurements from Global Ozone Monitoring Experiment, J. Geophys. Res., 106, 3475–3490, https://doi.org/10.1029/2000JD900657, 2001.

Koelemeijer, R. B. A., de Haan, J. F., and Stammes, P.: A database of spectral surface reflectivity in the range 335–772 nm derived from 5.5 years of GOME observations, J. Geophys. Res., 108, 4070, https://doi.org/10.1029/2002JD002429, 2003.

Kokhanovsky, A. A., von Hoyningen-Huene, W., and Burrows, J. P.: Determination of the cloud fraction in the SCIAMACHY ground scene using MERIS spectral measurements,, Int. J. Remote Sens., 30, 6151–6167, https://doi.org/10.1080/01431160902842326, 2009.

Krijger, J. M., van Weele, M., Aben, I., and Frey, R.: Technical note: The effect of sensor resolution on the number of cloud-free observations from space, Atmos. Chem. Phys., 7, 2881–2891, https://doi.org/10.5194/acp-7-2881-2007, 2007.

Kuze, A. and Chance, K. V.: Analysis of cloud top height and cloud coverage from satellites using the O_2 A and B bands, J. Geophys. Res., 99, 14 481–14 491, https://doi.org/10.1029/94JD01152, 1994.

Lang, R.: GOME-2 PMD Band Definitions 3.0 and PMD Calibration, EUMETSAT, http://www.eumetsat.int, Doc.No. EUM/OPS-EPS/DOC/07/0601, Issue v8, 2010.

Levelt, P. F., van den Oord, G. H. J., Dobber, M. R., Malkki, A., Visser, H., de Vries, J., Stammes, P., Lundell, J. O. V., and Saari, H.: The Ozone Monitoring Instrument, IEEE Trans. Geosci. Remote Sens., 44, 1093–1101, https://doi.org/10.1109/TGRS.2006.872333, 2006.

Li, X. and Strahler, A. H.: Geometric-optical bidirectional reflectance modeling of the discrete crown vegetation canopy: effect of crown shape and mutual shadowing, IEEE T. Geosci. Remote., 30, 276–292, https://doi.org/10.1109/36.134078, 1992.

Liu, C., Beirle, S., Butler, T., Liu, J., Hoor, P., Jöckel, P., Pozzer, A., Frankenberg, C., Lawrence, M. G., Lelieveld, J., Platt, U., and Wagner, T.: Application of SCIAMACHY and MOPITT CO total column measurements to evaluate model results over biomass burning regions and Eastern China, Atmos. Chem. Phys., 11, 6083–6114, https://doi.org/10.5194/acp-11-6083-2011, 2011.

Lorente, A., Boersma, K. F., Yu, H., Dörner, S., Hilboll, A., Richter, A., Liu, M., Lamsal, L. N., Barkley, M., De Smedt, I., Van Roozendael, M., Wang, Y., Wagner, T., Beirle, S., Lin, J.-T., Krotkov, N., Stammes, P., Wang, P., Eskes, H. J., and Krol, M.: Structural uncertainty in air mass factor calculation for NO_2 and HCHO satellite retrievals, Atmos. Meas Tech., 10, 759–782, https://doi.org/10.5194/amt-10-759-2017, 2017.

Lorente, A., Boersma, K. F., Stammes, P., Tilstra, G., Richter, A., Yu, H., Kharbouche, S., and Muller, J.-P.: The importance of surface reflectance anisotropy for cloud and NO_2 retrievals from GOME-2 and OMI, Atmos. Meas Tech., 11, 4509–4529, https://doi.org/10.5194/amt-11-4509-2018, 2018.

Loyola, D.: A new cloud recognition algorithm for optical sensors, in: IGARSS '98. Sensing and Managing the Environment. 1998 IEEE International Geoscience and Remote Sensing. Symposium Proceedings. (Cat. No.98CH36174), pp. 572–574, IEEE, https://doi.org/10.1109/IGARSS.1998.699514, 1998.

Loyola, D., Thomas, W., Livschitz, Y., Ruppert, T., Albert, P., and Hollmann, R.: Cloud Properties Derived From GOME/ERS-2 Backscatter Data for Trace Gas Retrieval, IEEE T. Geosci. Remote Sens., 45, 2747–2758, https://doi.org/10.1109/TGRS.2007.901043, 2007.

Loyola, D., Koukouli, M., Valks, P., Balis, D., Hao, N., Van Roozendael, M., Spurr, R., Zimmer, W., Kiemle, S., Lerot, C., and J.-C.Lambert: The GOME-2 Total Column Ozone Product: Retrieval Algorithm and Ground-Based Validation, J. Geophys. Res, 116, D07 302, https://doi.org/10.1029/2010JD014675, 2011.

Loyola, D. G., García, S. G., Lutz, R., Argyrouli, A., Romahn, F., Spurr, R. J. D., Pedergnana, M., Doicu, A., García, V. M., and Schüssler, O.: The operational cloud retrieval algorithms from TROPOMI on board Sentinel-5 Precursor, Atmos. Meas. Tech, 11, 409–427, https://doi.org//10.5194/amt-11-409-2018, 2018.

Loyola, D. G., Xu, J., Heue, K.-P., and Zimmer, W.: Applying FP_ILM to the retrieval of geometry-dependent effective Lambertian equivalent reflectivity (GE_LER) daily maps from UVN satellite measurements, Atmos. Meas. Tech, 13, 985–999, https://doi.org/10.5194/amt-13-985-2020, 2020.

Lutz, R., Loyola, D., Gimeno García, S., and Romahn, F.: OCRA radiometric cloud fractions for GOME-2 on MetOp-A/B, Atmos. Meas Tech., 9, 2357–2379, https://doi.org/10.5194/amt-9-2357-2016, 2016.

Martin, J., Eugenio, F., Marcello, J., and Medina, A.: Automatic Sun Glint Removal of Multispectral High-Resolution Worldview-2 Imagery for Retrieving Coastal Shallow Water Parameters, Remote Sens., 8, https://doi.org/10.3390/rs8010037, 2016.

Martin, R. V., Chance, K., Jacob, D., Kurosu, T. P., Spurr, R. J. D., Bucsela, E., Gleason, J. F., Palmer, P. I., Bey, I., Fiore, A. M., Li, Q., Yantosca, R. M., and Koelemeijer, R. B. A.: An improved retrieval of tropospheric nitrogen dioxide from GOME, J. Geophys. Res., 107, 4437, https://doi.org/10.1029/2001JD001027, 2002.

McKenzie, R. L., Johnston, P. V., McElroy, C. T., Kerr, J. B., and Solomon, S.: Altitude distributions of stratospheric constituents from ground-based measurements at twilight, J. Geophys. Res.-Atmos., 96, 15 499–15 511, https://doi.org/10.1029/91JD01361, 1991.

McPeters, R., Bhartia, P. K., Krueger, A. J., Herman, J. R., Schlesinger, B. M., Wellemeyer, C. G., Seftor, C. J., Jaross, G., Taylor, S. L., Swissler, T., Torres, O., Labow, G., Byerly, W., and Cebula, R. P.: Nimbus-7 Total Ozone Mapping Spectrometer (TOMS) Data Products User's Guide, Nasa reference publication 138, NASA, https://ozoneaq.gsfc.nasa.gov/media/docs/epusrguide.pdf, last access: 17 November 2020, 1996.

Munro, R., Eisinger, M., Anderson, C., Callies, J., Corpaccioli, E., Lang, R., Lefebvre, A., Livschitz, Y., and Albiñana, A. P.: GOME-2 on MetOp, in: Proc. of The 2006 EUMETSAT Meteorological Satellite Conference, Helsinki, Finland, 12–16 June 2006, EUMETSAT, p. 48, 2006.

Munro, R., Lang, R., Klaes, D., Poli, G., Retscher, C., Lindstrot, R., Huckle, R., Lacan, A., Grzegorski, M., Holdak, A., Kokhanovsky, A., Livschitz, J., and Eisinger, M.: The GOME-2 instrument on the Metop series of satellites: instrument design, calibration, and level 1 data processing – an overview, Atmos. Meas. Tech., 9, 1279–1301, https://doi.org/10.5194/amt-9-1279-2016, 2016.

NOAA: Advanced Very High Resolution Radiometer – AVHRR, Website, https://noaasis.noaa.gov/NOAASIS/ml/avhrr.html, last access 19 June 2019, 2017.

NOAA: Global Self-consistent Hierarchical High-resolution Geography (GSHHG), Version 2.3.7 June 15, 2017, https://www.ngdc.noaa.gov/mgg/shorelines/, last access: 1 March 2018, 2018.

Noguchi, K., Rozanov, A. R. V., Rozanov, A., Burrows, J. P., Irie, H., and Kita, K.: Effect of surface BRDF of various land cover types on geostationary observations of tropospheric NO_2, Atmos. Meas. Tech., 7, 3497–3508, https://doi.org/10.5194/amt-7-3497-2014, 2015.

5   Noxon, J. F., Whipple, E. C., and Hyde, R. S.: Stratospheric NO_2 – 1. Observational method and behaviour at mid-latitude, J. Geophys. Res., 84, 5047–5076, https://doi.org/10.1029/JC084iC08p05047, 1979.

Perliski, L. and Solomon, S.: On the evaluation of air mass factors for atmospheric near-ultraviolet and visible absorption spectroscopy, J. Geophys. Res.,, 98, 10 363–10 374, https://doi.org/10.1029/93JD00465, 1993.

Popp, C., Wang, P., Brunner, D., Stammes, P., Zhou, Y., and Grzegorski, M.: MERIS albedo climatology for FRESCO+ O2A-band
10   cloudretrieval, Atmos. Meas. Tech., 4, 463–483, https://doi.org/10.5194/amt-4-463-2011, 2011.

Rozanov, V. V. and Rozanov, A. V.: Differential optical absorption spectroscopy (DOAS) and air massfactor concept for a multiply scattering vertically inhomogeneous medium: theoretical consideration, Atmos. Meas. Tech., 3, 751–780, https://doi.org/10.5194/amt-3-751-2010, 2010.

Rozanov, V. V., Rozanov, A. V., Kokhanovsky, A. A., and Burrows, J. P.: Radiative transferthrough terrestrial atmosphere and ocean: Software
15   package SCIATRAN, J. Quant. Spectr.Radiat. Transfer, 113, 13–71, https://doi.org/10.1016/j.jqsrt.2013.07.004, 2014.

Sarkissian, A., Roscoe, H. K., and Fish, D. J.: Ozone measurementsby zenith-sky spectrometers: an evaluation of errors in air-massfactors calculated by radiative transfer model, J. Quant. Spectrosc. Ra., 54, 471–480, https://doi.org/10.1016/0022-4073(95)00085-Y, 1995.

Schueler, C. F., Clement, J. E., Ardanuy, P. E., Welsch, C., DeLuccia, F., and Swenson, H.: NPOESS VIIRS sensor design overview, Proc. SPIE 4483, in: Earth Observing Systems VI, https://doi.org/10.1117/12.453451, 2002.

20   Sihler, H., Lübcke, P., Lang, R., Beirle, S., de Graaf, M., Hörmann, C., Lampel, J., Penning de Vries, M., Remmers, J., Trollope, E., Wang, Y., and Wagner, T.: In-operation field-of-view retrieval (IFR) for satellite and ground-based DOAS-type instruments applying coincident high-resolution imager data, Atmos. Meas. Tech., 10, 881–903, https://doi.org/10.5194/amt-10-881-2017, 2017.

Solomon, S., Schmeltekopf, A. L., and Sanders, R. W.: On the interpretation of zenith sky absorption measurements, J. Geophys. Res.-Atmos., 92, 8311–8319, https://doi.org/10.1029/JD092iD07p08311, 1987.

25   Stammes, P., Sneep, M., de Haan, J. F., Veefkind, J. P., Wang, P., and Levelt, P. F.: Effective cloud fractions from the Ozone Monitoring Instrument: Theoretical framework and validation, J. Geophys. Res.-Atmos., 113, D16S38, https://doi.org/10.1029/2007JD008820, 2008.

TEMIS: FRESCO product versions description, Internet, http://www.temis.nl/fresco/versions.html, last access: 4 February 2019, 2019.

Tilstra, L. G., De Graaf, M., Aben, I., and Stammes, P.: In-flight degradation correction of SCIAMACHY UV reflectances and Absorbing Aerosol Index, J. Geophys. Res.-Atmos., 117, D06 209, https://doi.org/10.1029/2011JD016957, 2012.

30   Tilstra, L. G., Tuinder, O. N. E., and Stammes, P.: Algorithm theoretical basis document – GOME-2 surface LER product, Internet, https://acsaf.org/docs/atbd/Algorithm_Theoretical_Basis_Document_LER_May_2017.pdf, last access: 17 May 2019, 2017a.

Tilstra, L. G., Tuinder, O. N. E., Wang, P., and Stammes, P.: Surface reflectivity climatologies from UV to NIR determined from Earth observations by GOME-2 and SCIAMACHY, J. Geophys. Res.-Atmos., 122, https://doi.org/10.1002/2016JD025940, 2017b.

Tuinder, O., de Graaf, M., Tilstra, G., Penning de Vries, M., and Kooreman, M.: Algorithm theoretical basis document – ATBD for the Ab-
35   sorbing Aerosol Index product, Internet, https://acsaf.org/docs/atbd/Algorithm_Theoretical_Basis_Document_NAR_NAP_ARS_ARP_Sep_2019.pdf, last access: 28 November 2020, 2020.

Tuinder, O. N. E., de Winter-Sorkina, R., and Builtjes, P. J. H.: Retrieval methods of effective cloud cover from the GOME instrument: an intercomparison, Atmos. Chem. Phys., 4, 255–273, https://doi.org/10.5194/acp-4-255-2004, 2004.

USGS: Global 30 Arc-Second Elevation (GTOPO30), Internet, USGS EROS Archive, https://doi.org/10.5066/F7DF6PQS, https://www.usgs.gov/media/files/gtopo30-readme, last access: 22 October 2020, 2018.

Várnai, T. and Marshak, A.: View angle dependence of cloud optical thicknesses retrieved by Moderate Resolution Imaging Spectroradiometer (MODIS), J. Geophys. Res., 112, D06 203, https://doi.org/10.1029/2005JD006912, 2007.

5   Vasilkov, A., Qin, W., Krotkov, N., Lamsal, L., Spurr, R., Haffner, D., Joiner, J., Yang, E.-S., and Marchenko, S.: Accounting for the effects of surface BRDF on satellite cloud and trace-gas retrievals: a new approach based on geometry-dependent Lambertian equivalent reflectivity applied to OMI algorithms, Atmos. Meas Tech., 10, 333–349, https://doi.org/10.5194/amt-10-333-2017, 2017.

Vasilkov, A., Yang, E.-S., Marchenko, S., Qin, W., Lamsal, L., Joiner, J., Krotkov, N., Haffner, D., Bhartia, P. K., and Spurr, R.: A cloud algorithm based on the O_2-O_2 477 nm absorption band featuring an advanced spectral fitting method and the use of surface geometry-

10 dependent Lambertian-equivalent reflectivity, Atmos. Meas Tech., 11, 4093–4107, https://doi.org/10.5194/amt-11-4093-2018, 2018.

Veefkind, J. P., Aben, I., McMullan, K., Förster, H., de Vries, J., Otter, G., Claas, J., Eskes, H. J., de Haan, J. F., Kleipool, Q., van Weele, M., Hasekamp, O., Hoogeveen, R., Landgraf, J., Snel, R., Tol, P., Ingmann, P., Voors, R., Kruizinga, B., Vink, R., Visser, H., and Levelt, P. F.: TROPOMI on the ESA Sentinel-5 Precursor: A GMES mission for global observations of the atmospheric composition for climate, air quality and ozone layer applications, Remote Sens. of Environ., 120, 70–83, https://doi.org/10.1016/j.rse.2011.09.027, 2012.

15 Veefkind, J. P., de Haan, J. F., Sneep, M., and Levelt, P. F.: Improvements to the OMI O2–O2 operational cloud algorithm and comparisons with ground-based radar–lidar observations, Atmos. Meas. Tech., 9, 6035–6049, https://doi.org/10.5194/amt-9-6035-2016, 2016.

Wagner, T., Heland, J., Zöger, M., and Platt, U.: A fast H_2O total column density product from GOME – Validation with in-situ aircraft measurements, Atmos. Chem. Phys., 3, 651–663, https://doi.org/10.5194/acp-3-651-2003, 2003.

Wang, P., Stammes, P., van der A, R., Pinardi, G., and van Roozendael, M.: FRESCO+: an improved O_2 A-band cloud retrieval algorithm

20 for tropospheric trace gas retrievals, Atmos. Chem. Phys., 8, 6565–6576, https://doi.org/10.5194/acp-8-6565-2008, 2008.

Wang, P., Tuinder, O., and (KNMI), P. S.: FRESCO+ version 2 for GOME-2 Metop-C processing, Internet, http://www.temis.nl/fresco/frescopv2_metopc_WP1_report_20181026.pdf, last access: 16 November 2020, 2018.

Wanner, W., Li, X., and Strahler, A. H.: On the derivation of kernels for kernel-driven models of bidirectional reflectance, J. Geophys. Res., 100, 21 077–21 089, https://doi.org/10.1029/95JD02371, 1995.

25 Wessel, P. and Smith, W. H. F.: A Global Self-consistent, Hierarchical, High-resolution Shoreline Database, J. Geophys. Res., 101, 8741–8743, 1996.

Zhang, H. and Wang, M.: Evaluation of sun glint models using MODIS measurements, J. Quant. Spectrosc. Ra., 111, 492–506, https://doi.org/10.1016/j.jqsrt.2009.10.001, 2010.